Institute of Thermoelectricity, Academy of Sciences and Ministry of Education and Science of Ukraine

Journal of THERMOELECTRICITY

International Research

Founded in December, 1993

published 6 times a year

No. 6 *2014*

Editorial Board

International Editorial Board

Founders - National Academy of Sciences, Ukraine
Institute of Thermoelectricity of National Academy of Sciences and Ministry of Education and Science of Ukraine

Certificate of state registration № КВ 15496-4068 ПР

Editorial office manager O. Pugantseva

Approved for printing by the Academic Council of Institute of Thermoelectricity of the National Academy of Sciences and Ministry of Education and Science, Ukraine

Address of editorial office:
Ukraine, 58002, Chernivtsi, General Post Office, P.O. Box 86.
Phone: +(380-372) 90 31 65.
Fax: +(380-3722) 4 19 17.
E-mail: jt@inst.cv.ua
http://www.jt.inst.cv.ua

Signed for publication 25.12.14. Format 70×108/16. Offset paper №1. Offset printing.
Printer's sheet 11.1. Publisher's signature 9.2. Circulation 400 copies. Order 6.

Printed from the layout original made by "Journal of Thermoelectricity" editorial board in the printing house of "Bukrek" publishers,
10, Radischev Str., Chernivtsi, 58000, Ukraine

Merry Christmas and Happy New Year!

L. Anatychuk

Dear readers of the "Journal of Thermoelectricity"!

Editorial Board is happy to congratulate you on the occasion of the New Year – 2015!

CONTENTS

Yu. A. Kruglyak

Department of Information Technologies, Odessa State Environmental University, 15, Lvivska Str., Odessa, 65016, Ukraine

Yu. A. Kruglyak

ELECTRIC CURRENT, THERMOCURRENT, AND HEAT FLUX IN NANO- AND MICROELECTRONICS: TRANSPORT MODEL

The Landauer – Datta – Lundstrom modern electron and heat transport model is briefly summarized. If a band structure is chosen analytically or numerically, the number of conduction modes can be evaluated and, if a model for a mean-free-path for backscattering can be established, then the near-equilibrium thermoelectric transport coefficients can be calculated for 1D, 2D, and 3D resistors of any size in ballistic, quasi-ballistic, and diffusive linear response regimes when there are differences in both voltage and/or temperature across the device.

Modes of conduction and transmission concepts are introduced. A new expression for resistivity is suggested providing a different view of resistivity in terms of the specific number of modes (per unit cross-sectional area) and the mean-free-path for backscattering. Fermi conduction window functions for electrons and phonons are formulated and compared. Whether a conductor is good or bad is determined only by the availability of the conductor energy states in an energy window ~ ± 2kT around the equilibrium electrochemical potential, which can vary widely from one material to another. Special attention is given to the near-equilibrium transport.

A general expression for thermocurrent is introduced which is suitable for analysis of conductivity of any materials from metals and semiconductors up to modern nanoresistors and nanocomposites. This general expression is simplified for the case of a linear response regime. Thermocurrent is expressed in terms of three transport coefficients -the conductivity, the Soret electro-thermal diffusion coefficient, and the electronic heat conductance under the short circuit conditions.

Heat transfer by phonons is treated in detail. The basic equation for the heat current is formulated. Electrical and thermal conductances are similar in structure, namely both are proportional to corresponding quantum of conductance, times an integral over the transmission, times the number of modes, times a window function. Moreover, the thermal broadening functions for electrons and phonons have similar shapes and each has a width of a few kT. Along with the number of modes determined by the dispersion relation, these two window functions play a key role in quantitative determination of the electrical and thermal conductivities.

Keywords: nanoelectronics, microelectronics, microelectronics, conductivity modes, transmission coefficient, Fermi windows, near-equilibrium transport, ballistic transport, quasi-ballistic transport, diffusive transport.

Introduction

The objective of this paper is to give a condensed summary of modern Landauer – Datta – Lundstrom (LDL) electron and heat transport model [1 – 5] which works well at the nanoscale, as well as at the macroscale for 1D, 2D, and 3D resistors in ballistic, quasi-ballistic, and diffusive linear response regimes, when there are differences in both voltage and temperature across the device.

We begin with two well known basic equations – for current and for the total number of electrons in the channel of a conductor under steady-state conditions and introduce a concept of conduction modes for resistors of different dimensions. Then introduce a concept of transmission coefficient as the relation of two transit times – ballistic to diffusive. It is shown that transmission coefficient is the relation of the mean-free-path for backscattering to the resistor length or in the most general case is the relation of the mean-free-path for backscattering to the sum of resistor length and the mean-free-path for backscattering. Now one can specify three transport regimes: diffusive, ballistic, and quasi-ballistic. Then new expression for a specific resistivity is suggested providing a different view of resistivity in terms of the specific number of modes (per unit cross-sectional area) and the mean-free-path for backscattering.

Further we treat only the near-equilibrium transport known also as the low field linear response regime which is most important practically and strongly influences and controls the performance of most electronic devices. Fermi conduction window function is introduced as a negative derivative of the equilibrium Fermi function over energy. Whether a conductor is good or bad is determined only by the availability of the conductor energy states in an energy window ~ $\pm 2kT$ around the equilibrium electrochemical potential, which can vary widely from one material to another. Current is driven by the difference of the Fermi functions in the "agenda" of the two contacts which for low bias is proportional to the Fermi conduction window function but not by so called "external electric field" as assumed in the Drude model still being useful and used in research and teaching. Thus famous Landauer expression for conductivity is introduced. Transport in a massive 3D conductor is treated.

It is shown that the conductance is always the product of the quantum of conductance, times the average transmission, times the number of modes in the Fermi windows which is one of the basic results of the LDL transport model.

Finally, the LDL model is generalized for thermocurrent. A general expression for thermocurrent is introduced which is suitable for analysis of conductivity of any materials from metals to semiconductors up to modern nanoresistors and nanocomposites. This general expression is simplified for the case of the linear response regime when there are differences in both voltage and temperature across the device. Thermocurrent is expressed through three transport coefficients – conductivity, the Soret electro-thermal diffusion coefficient, and the electronic heat conductance under the short circuit conditions as well as via these three specific transport coefficients. These equations are also valid for 1D and 2D resistors, but the units of the various terms differ. In summary, when a band structure is given, the number of modes can be

evaluated and, if a model for the mean-free-path for backscattering can be chosen, then the near-equilibrium transport coefficients can be evaluated using the expressions derived.

Heat transfer by phonons is treated in details. Basic equation for the heat current due to phonons is formulated. The rest is concerned with the linear response conditions. By analogy with the Fermi window function for electrons, the Fermi window function for phonons is introduced. As a result, an expression for the lattice thermal conductance is obtained which is proportional to the quantum of thermal conductance. It is valuable that the electrical and thermal conductivities are similar in structure, namely: both are proportional to corresponding quantum of conductance, times an integral over the transmission, times the number of modes, times a window function. Moreover, the thermal broadening functions for electrons and phonons have similar shapes and each has a width of a few kT. Along with the number of modes determined by the dispersion relation, these two window functions play a key role in determining the electrical and thermal conductivities.

1. LDL model for current

Two basic equations for electric current

$$N = \int \frac{D(E)}{2}\left(f_1 + f_2\right)dE\,, \tag{1}$$

$$I = \frac{2q}{h}\int \gamma(E)\pi\frac{D(E)}{2}\left(f_1 - f_2\right)dE \tag{2}$$

are easily derived [5 – 7], where N is the total, steady-state number of electrons in the channel, $D(E)$ is the density-of-states with the spin degeneracy factor $g_s = 2$ included, the Fermi function

$$f\left(E\right) = \frac{1}{e^{(E-E_F)/kT}+1} \tag{3}$$

is indexed with the resistor contact numbers 1 and 2, E_F is the Fermi energy which as well as temperature T may be different at both contacts, "broadening" $\gamma(E)$ relates to transit time for electrons to cross the resistor channel

$$\gamma(E) \equiv \frac{\hbar}{\tau(E)}\,. \tag{4}$$

Proportionality of current to $\left(f_1 - f_2\right)$ makes sence, and fundamental constant $2q/h$ is important and known as the Klitzing constant. According to (4), γ is measured in energy units, the density-of-states has units of (energy)$^{-1}$, thus the product $\gamma(E)\pi D(E)/2$ is dimensionless. We shall see now that $\gamma(E)\pi D(E)/2 \equiv M(E)$ has a physical meaning of the number of the resistor conduction modes (channels) at energy E.

1.1. Conduction modes

Let us consider 2D ballistic resistor of length L which is much shorter than a mean-free-pass for back-scattering λ, oriented along the x axis and having width W along the y axis. The total density-of-states is

$$D(E) = D_{2D}\,(\mathrm{E})\,L \cdot W, \tag{5}$$

$$D_{2D}(E) = g_v \frac{m^*}{\pi\hbar^2},\ [1/J{\cdot}m^2] \tag{6}$$

where $D_{2D}(E)$ is the specific density-of-states (per unit area $A = L \cdot W$) written for parabolic energy bands with an effective mass m^* and occupation of a single subband due to confinement in the z direction with a valley degeneracy g_v [8].

Let us determine the characteristic time τ. Equations (38) and (46) of [6] give

$$\frac{qN'(E)dE}{I'(E)dE} = \frac{\hbar}{\gamma}\frac{(f_1 + f_2)}{(f_1 - f_2)}, \tag{7}$$

where $N'(E)dE$ is the steady-state number of electrons in the channel in differential form

$$N'(E)dE = \frac{D(E)dE}{2} f_1(E) + \frac{D(E)dE}{2} f_2(E) \tag{8}$$

and current in differential form

$$I'(E)\,dE = \frac{q}{2\tau(E)}\left(N'_{01}\,dE - N'_{02}\,dE\right) = \frac{2q}{h}\frac{\gamma(E)}{2}\pi D(E)\,dE(f_1 - f_2) \tag{9}$$

with

$$N'_{01}(E)\,dE = D(E)\,dE\,f_1(E) \tag{10}$$

and

$$N'_{02}(E)\,dE = D(E)\,dE\,f_2(E) \tag{11}$$

as the number of electrons being in equilibrium between channel and contact 1, as well as channel and contact 2, between energy E and $E + dE$. We have assumed that current is defined to be positive when it flows from the outside into contact 2 with electrons moving from contact 1 to contact 2 (standard agreement).

Let us now apply a large enough voltage $V = (E_{F1} - E_{F2})/q$ to contact 2 which makes $E_{F2} << E_{F1}$, thus $f_2 << f_1$. Then Eq. (7) becomes

$$\frac{qN'(E)\,dE}{I'(E)\,dE} = \frac{\text{stored charge}}{\text{current}} = \frac{\hbar}{\gamma} = \tau(E). \tag{12}$$

The number of electrons in the resistor is

$$N'(E) = n_S'(E)\,L \cdot W\,, \tag{13}$$

where n_S' is the specific electron density (per unit area) and differential current

$$I'(E) = qWn_S'(E)\left\langle v_x^+(E)\right\rangle. \tag{14}$$

Thus Eq. (12) gives

$$\tau(E) = \frac{L}{\left\langle v_x^+(E)\right\rangle}, \tag{15}$$

which is simply the average transit time of electrons across the channel.

To evaluate τ, one needs to calculate the average velocity of an electron in the +*x* direction, from contact 1 to contact 2. This velocity in our case of ballistic transport, in which electrons move across the resistor without changing direction

$$\left\langle v_x^+(E)\right\rangle = v(E)\left\langle\cos\theta\right\rangle, \tag{16}$$

where angle θ is counted out of positive direction of the *x* axis. The average

$$\left\langle\cos\theta\right\rangle = \frac{1}{\pi}\int_{-\pi/2}^{\pi/2}\cos\theta d\theta = \frac{2}{\pi}, \tag{17}$$

thus for parabolic dispersion and under isotropic conditions assumed one obtains

$$\left\langle v_x^+(E)\right\rangle = \frac{2}{\pi}v = \frac{2}{\pi}\sqrt{\frac{2(E-E_C)}{m^*}}. \tag{16}$$

Defining conduction modes as

$$M(E) \equiv \gamma(E)\pi\frac{D(E)}{2} \tag{17}$$

and using (4) and (5), one finally obtains

$$M(E) = M_{1D}(E) = \frac{h}{4}\left\langle v_x^+(E)\right\rangle D_{1D}(E)\,,$$

$$M(E) = WM_{2D}(E) = W\frac{h}{4}\left\langle v_x^+(E)\right\rangle D_{2D}(E)\,, \tag{18}$$

$$M(E) = AM_{3D}(E) = A\frac{h}{4}\left\langle v_x^+(E)\right\rangle D_{3D}(E)\,,$$

where similar arguments were used to get the final results also for 1D and 3D conductors. One may note that the number of conduction modes at energy *E* is proportional to the width of 2D resistor and to the cross-sectional area *A* of 3D resistor.

Let us now call attention to the physical meaning of the results summarized in (18). Thus, for 2D conductor accounting for (6) and (16) we have

$$WM_{2D}(E) = g_v W \frac{\sqrt{2m^*(E - E_C)}}{\pi\hbar}. \tag{19}$$

In the case of a parabolic dispersion

$$E(k) = E_C + \frac{\hbar^2 k^2}{2m^*} \tag{20}$$

with the wave vector expressed through the de Broglie wavelength of electrons at energy E

$$\lambda_B = 2\pi/k, \tag{21}$$

from general expression (19) for the number of modes for 2D conductor one obtains important relation

$$WM_{2D}(E) = g_v \frac{Wk}{\pi} = g_v \frac{W}{\lambda_B(E)/2} = M(E), \tag{22}$$

which opens up a possibility of physical interpretation of the number of modes for 2D conductor, namely: $M(E)$ is just the number (accounting also for the valley degeneracy g_v) of the de Broglie electron half wavelengths that fit into the width of the resistor. Integrality of the conduction mode numbers is assured by the boundary conditions with the imperative vanishing of the wave function at the two edges of the 2D conductor. A thorough discussion of conduction modes concept for 1D, 2D, and 3D nano- and mesoresistors can be found in [9 – 12].

To summarize, now we have two basic equations for current

$$N = \int \frac{D(E)}{2}(f_1 + f_2)\,dE,$$

$$I = \frac{2q}{h}\int M(E)(f_1 - f_2)\,dE, \tag{23}$$

according to which to compute the number of electrons and the current, one needs two quantities – $D(E)$ and $M(E)$.

For parabolic energy bands (20) the 1D, 2D, and 3D densities of states are well known and given by

$$D(E) = D_{1D}(E)L = \frac{L}{\pi\hbar}\sqrt{\frac{2m^*}{(E - E_C)}}H(E - E_C),$$

$$D(E) = D_{2D}(E)A = A\frac{m^*}{\pi\hbar^2}H(E - E_C), \tag{24}$$

$$D(E) = D_{3D}(E)\Omega = \Omega\frac{m^*\sqrt{2m^*(E - E_C)}}{\pi^2\hbar^3}H(E - E_C),$$

where Ω is the volume of the 3D resistor, and $H(E - E_c)$ is the Heaviside step function. The number of modes in this particular case of parabolic dispersion

$$M(E) = M_{1D}(E) = H\left(E - E_C\right),$$

$$M(E) = WM_{2D}(E) = Wg_v \frac{\sqrt{2m^*(E - E_C)}}{\pi\hbar} H\left(E - E_C\right), \tag{25}$$

$$M(E) = AM_{3D}(E) = Ag_v \frac{m^*(E - E_C)}{2\pi\hbar^2} H\left(E - E_C\right).$$

Although we have assumed a parabolic dispersion above, the expressions for $M(E)$ (18) have general meaning and valid for linear dispersion like in graphene. For an arbitrary band structure a numerical procedure might be used [13].

1.2. Transmission coefficient

We have treated ballistic transport above. Let us turn to diffusive case when $L >> \lambda$. Electrons injected from contacts 1 and 2 undergo a random walk. Some trajectories terminate at the injecting contact and some at the other contact. If a positive voltage is applied to contact 2, then a few more electrons terminate on contact 2.

A key parameter in the LDL transport model is a quantity $\gamma(E)\pi D(E)/2$ which is the number of conduction modes $M(E)$ in the case of ballistic transport. The broadening γ relates to the transit time as $\gamma = \hbar/\tau$. The transit time is being increased when transport becomes diffusive, thus $\gamma(E)\pi D(E)/2$ will decrease. It will be shown now that for diffusive transport $\gamma\pi D(E)/2 = M(E) \cdot T(E)$, where $T(E) \leq 1$ is known as the transmission coefficient.

In ballistic regime electrons are injected into channel at different angles. Accordingly, there is a certain distribution of transit times. Thus, the value of γ is found through the average transit time

$$\gamma(E) = \frac{\hbar}{\langle \tau(E) \rangle}, \tag{26}$$

where for 2D conductor

$$\langle \tau(E) \rangle = \frac{L}{\langle v_x^+(E) \rangle} = \frac{L}{v(E)\langle \cos\vartheta \rangle} = \frac{L}{v(E)(2/\pi)}. \tag{27}$$

What would be $\langle \tau(E) \rangle$ for diffusive transport?

When $L >> \lambda$, then the first Fick's law of diffusion would be applied. In case of 2D conductor the current flux

$$J = q\bar{D}\frac{dn_S}{dx}, \tag{28}$$

where current density is proportional to the surface electron density gradient and $\bar{D}$ is a diffusion coefficient.

Let electrons be injected into a channel mostly by contact 1. Then $f_1 \approx 1$ and $f_2 \approx 0$. There is a finite concentration of injected electrons $\Delta n_S(0)$ at the left side ($x = 0$) of the conductor. For a long channel $\Delta_S(L) \to 0$ due to $f_2 \approx 0$. The electron profile is linear, because no recombination-generation processes are assumed.

Transit time according to (12) is determined by the stored charge relative to current

$$\tau_D = \frac{qN}{I} = \frac{Wq\Delta n_S(0)L/2}{Wq\bar{D}\Delta n_S(0)/L} = \frac{L^2}{2\bar{D}}, \tag{29}$$

where the total number of electrons in the conductor is $N = n_S(0)WL/2$ and current $I = J \cdot W$ with $dn_s/dx = \Delta n_S(0)/L$. From (29) and (28) we conclude that the diffusive transit time is

$$\tau_D = \frac{L^2}{2\bar{D}}, \tag{30}$$

while the ballistic transit time

$$\tau_B = \frac{L}{\langle v_x^+ \rangle}. \tag{31}$$

Gathering all together and remembering definition of γ (26) for both regimes, one obtains

$$\gamma(E)\pi\frac{D(E)}{2} = \frac{\hbar}{\tau_D}\pi\frac{D(E)}{2} = \frac{\hbar}{\tau_B}\pi\frac{D(E)}{2}\frac{\tau_B}{\tau_D} \equiv M(E)T(E), \tag{32}$$

where we see that transmission coefficient is the relation of two transit times – ballistic to diffusive

$$T(E) = \frac{\tau_B}{\tau_D}. \tag{34}$$

In other words, in the presence of electron scattering the number of modes $M(E)$ just needs to be replaced by $M(E) \cdot T(E)$. A thorough discussion of transition from ballistic transport to diffusion regime for 1D and 3D conductors may be found in [7, 9, 10, 14, 15].

From (34) together with (30) and (31) we obtain

$$T(E) = \frac{2\bar{D}}{L\langle v_x^+ \rangle}. \tag{35}$$

Random walks theory [16] gives

$$\bar{D} = \frac{\langle v_x^+ \rangle \lambda}{2}, \tag{36}$$

and finally one obtains a simple expression for the transmission coefficient

$$T(E) = \frac{\lambda}{L} \ll 1, \tag{37}$$

with λ as the mean-free-path for backscattering. As it was already noted,

$$\gamma \pi D(E)/2 = M(E) \cdot T(E) \tag{38}$$

is greatly reduced in diffusion regime relative to ballistic one.

Equation (37) is accurate in the diffusion limit ($L >> \lambda$), but it fails when length of a conductor is short enough. In the most general case [4, 5]

$$T(E) = \frac{\lambda(E)}{\lambda(E) + L}, \tag{39}$$

which is valid for both diffusive and ballistic regimes, as well as between

$$\begin{gathered} \text{Diffusive: } L >> \lambda;\ \ T = \lambda/L << 1, \\ \text{Ballistic: } L << \lambda;\ \ T \to 1, \\ \text{Quasi-ballistic: } L \approx \lambda;\ \ T < 1. \end{gathered} \tag{40}$$

It is remarkable that such a simple transport model works well in all three regimes.

1.3. Ohm's law

It is now clearly established that the resistance of a ballistic conductor can be written in the form

$$R^{ball} = \frac{h}{q^2}\frac{1}{M(E)}. \tag{41}$$

This result is now fairly well known, but the common belief is that it applies only to short resistors and belongs to a course on special topics like mesoscopic physics or nanoelectronics. What is not well known is that the resistance for both long and short conductors can be written as

$$R(E) = \frac{h}{q^2}\frac{1}{M(E)}\left(1 + \frac{L}{\lambda(E)}\right). \tag{42}$$

Ballistic and diffusive conductors are not two different worlds, but rather a continuum as the length L is increasing. Ballistic limit is obvious for $L << \lambda$, while for $L >> \lambda$ it reduces into standard Ohm's law

$$R \equiv \frac{V}{I} = \rho\frac{L}{A}. \tag{43}$$

Indeed, we could rewrite $R(E)$ above as

$$R(E) = \frac{\rho(E)}{A}[L + \lambda(E)] \tag{44}$$

with a new expression for resistivity

$$\rho(E) = \frac{h}{q^2}\left(\frac{1}{M(E)/A}\right)\frac{1}{\lambda(E)}, \tag{45}$$

which provides a different view of resistivity in terms of the number of modes per unit area and the mean-free-path.

1.4. Linear response regime

Near-equilibrium transport or low field linear response regime corresponds to $\lim(dI/dV)_{V\to 0}$. There are several reasons to develop a low field transport model. First, near-equilibrium transport is the foundation for understanding transport in general. Concepts introduced in the study of near-equilibrium regime are often extended to treat more complicated situations, and near-equilibrium regime is used as a reference point when we analyze transport in more complex conditions. Second, near-equilibrium transport measurements are widely used to characterize electronic materials and to understand the properties of new materials. And finally, near-equilibrium transport strongly influences and controls the performance of most electronic devices.

Let us assume that under the low field condition

$$f_0(E) \approx f_1(E) > f_2(E), \tag{46}$$

where $f_0(E)$ is the equilibrium Fermi function, and an applied bias

$$V = \Delta E_F / q = (E_{F1} - E_{F2})/q \tag{47}$$

is small enough. Using the Taylor expansion under constant temperature condition

$$f_2 = f_1 + \frac{\partial f_1}{\partial E_1}\nabla E_F = f_1 + \frac{\partial f_1}{\partial E_1} qV \tag{48}$$

and the property of the Fermi function

$$+\frac{\partial f}{\partial E_F} = -\frac{\partial f}{\partial E} \tag{49}$$

one finds

$$f_1 - f_2 = (-\frac{\partial f_0}{\partial E})qV\,. \tag{50}$$

The derivative of the Fermi function multiplied by *kT* to make it dimensionless

$$F_T\left(E, E_F\right) = kT\left(-\frac{\partial f}{\partial E}\right) \tag{51}$$

is known as thermal broadening function and shown in Fig. 1.

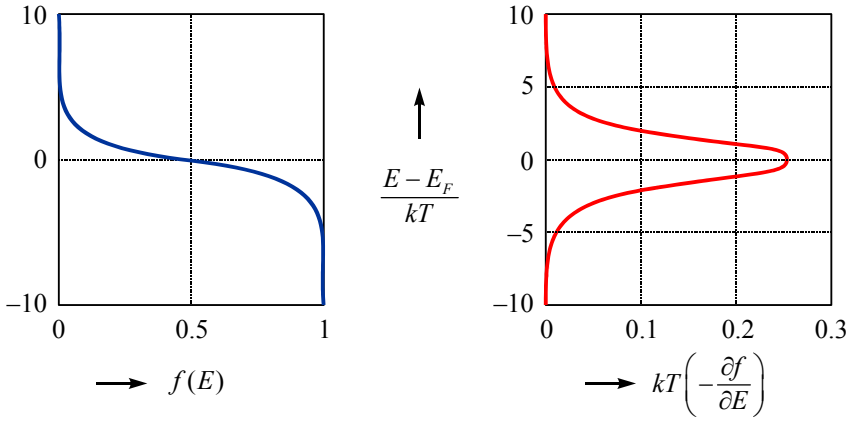

Fig. 1. Fermi function and the dimensionless normalized thermal broadening function.

If one integrates F_T over the entire energy range, the total area

$$\int_{-\infty}^{+\infty} dEF_T\left(E,E_F\right)=kT\,, \tag{52}$$

so that we can approximately visualize F_T as a rectangular pulse centered around $E=E_F$ with a peak value of ¼ and a width of ~ $4kT$.

The derivative $(-\partial f_0/\partial E)$ is known as the Fermi conduction window function. Whether a conductor is good or bad is determined by the availability of the conductor energy states in an energy window ~ $\pm 2kT$ around the electrochemical potential E_{F0}, which can vary widely from one material to another. Current is driven by the difference f_1-f_2 of the two contacts which for low bias is proportional to the derivative of the equilibrium Fermi function (50). Current generation concept based on experimental and theoretical results of modern nano- and mesophysics are discussed thoroughly in [4, 5, 9, 10, 17].

With the near-equilibrium assumption for current (23) instead of most general expression valid for both diffusive and ballistic regimes as well as in between

$$I=\frac{2q}{h}\int T(E)M(E)\left(f_1-f_2\right)dE\,, \tag{53}$$

we have now

$$I=\left[\frac{2q^2}{h}\int T(E)M(E)\left(-\frac{\partial f_0}{\partial E}\right)dE\right]V=GV\,, \tag{54}$$

with conductivity

$$G=\frac{2q^2}{h}\int T(E)M(E)\left(-\frac{\partial f_0}{\partial E}\right)dE\,, \tag{55}$$

known as the Landauer expression which is valid in 1D, 2D, and 3D resistors, if we use the appropriate expressions for $M(E)$.

1.5. Transport in a massive conductor

For ballistic limit $T(E)=1$. For diffusive transport $T(E)$ is given by equation (39). For a conductor much longer than a mean-free-path the equation for current density is

$$J_x = \frac{\sigma}{q}\frac{d\left(E_F\right)}{dx} \tag{56}$$

where the electrochemical potential E_F is also known as the quasi-Fermi level.

For a 2D conductor the surface specific conductivity is

$$\sigma_S = \frac{2q^2}{h}\int M_{2D}(E)\lambda(E)\left(-\frac{\partial f_0}{\partial E}\right)dE\,. \tag{57}$$

or in a different form

$$\sigma_S = \int \sigma'_S(E)dE\,, \tag{58a}$$

where differential specific conductivity

$$\sigma'_S(E) = \frac{2q^2}{h}M_{2D}(E)\lambda(E)\left(-\frac{\partial f_0}{\partial E}\right). \tag{58b}$$

Similar expressions can be written for 1D and 3D resistors.

Another way to write the conductance is the product of the quantum of conductance, times the average transmission, times the number of modes in the Fermi windows:

$$G = \frac{2q^2}{h}\left\langle\left\langle T\right\rangle\right\rangle\left\langle M\right\rangle, \tag{59a}$$

$$\left\langle M\right\rangle = \int M(E)(-\frac{\partial f_0}{\partial E})dE\,, \tag{59b}$$

$$\left\langle\left\langle T\right\rangle\right\rangle = \frac{\int T(E)M(E)\,(-\frac{\partial f_0}{\partial E})\,dE}{\int M(E)\,(-\frac{\partial f_0}{\partial E})\,dE} = \frac{\left\langle MT\right\rangle}{\left\langle M\right\rangle}\,. \tag{59c}$$

Yet another way to write the conductance is in terms of the differential conductance $G'(E)$ as

$$G = \int G'(E)dE\,,\ [S] \tag{60a}$$

$$G'(E) = \frac{2q^2}{h}M(E)T(E)\left(-\frac{\partial f_0}{\partial E}\right). \tag{60b}$$

2. LDL model for thermocurrent and thermoelectric coefficients

Electrons carry both charge and heat. The charge current is given by Eq. (53). To get the

equation for the heat current, one notes that electrons in the contacts flow at an energy $E \approx E_F$. To enter a mode $M(E)$ in the resistor electrons must absorb (if $E > E_F$) or emit (if $E < E_F$) a thermal energy $E - E_F$. We conclude that to get the heat current equation, we should insert $(E - E_F)/q$ inside the integral. The resulting thermocurrent

$$I_Q = \frac{2}{h}\int (E - E_F)T(E)M(E)\left(f_1 - f_2\right)dE\,. \tag{61}$$

It is important from practical point of view that both expressions – for the electric current (53) and thermocurrent (61) are suitable for analysis of conductivity of any materials from metals to semiconductors up to modern nanocomposites [18].

When there are differences in both voltage and temperature across the resistor, then we must expand the Fermi difference $\left(f_1 - f_2\right)$ in a Taylor series in both voltage and temperature and get

$$f_1 - f_2 \approx \left(-\frac{\partial f_0}{\partial E}\right)q\Delta V - \left(-\frac{\partial f_0}{\partial E}\right)\frac{E - E_F}{T}\Delta T\,, \tag{62}$$

where $\Delta V = V_2 - V_1$, $\Delta T = T_2 - T_1$ and $T = (T_1 + T_2)/2$.

Deriving a general near-equilibrium current equation is now straightforward. The total current is the sum of the contributions from each energy mode

$$I = \int I'(E)dE\,, \tag{63a}$$

where the differential current is

$$I'(E) = \frac{2q}{h}T(E)M(E)\left(f_1 - f_2\right). \tag{63b}$$

Using Eq. (62), we obtain

$$I'(E) = G'(E)\Delta V + S'_T(E)\Delta T\,, \tag{64a}$$

where

$$G'(E) = \frac{2q^2}{h}T(E)M(E)\left(-\frac{\partial f_0}{\partial E}\right) \tag{64b}$$

is the differential conductance and

$$S'_T(E) = -\frac{2q^2}{h}T(E)M(E)\left(\frac{E - E_F}{qT}\right)\left(-\frac{\partial f_0}{\partial E}\right) = -\frac{k}{q}\left(\frac{E - E_F}{kT}\right)G'(E) \tag{64c}$$

is the Soret coefficient for electro-thermal diffusion in differential form. Note that $S'_T(E)$ is negative for the modes with the energy above E_F (*n*-resistors) and positive for the modes with the energy below E_F (*p*-resistors).

Now we integrate Eq. (64a) over all energy modes and find

$$I = G\Delta V + S_T \Delta T\,, \ [\mathrm{A}] \tag{65a}$$

$$I_Q = -T\,S_T\,\Delta V - K_0\,\Delta T\,, \ [\mathrm{W}] \tag{65b}$$

with three transport coefficients – conductivity given by Eqs. (60) , the Soret electro-thermal diffusion coefficient

$$S_T = \int S_T'(E)dE = -\frac{k}{q}\int\left(\frac{E-E_F}{kT}\right)G'(E)dE\,, \ [\mathrm{A/K}] \tag{65c}$$

and the electronic heat conductance under the short circuit conditions ($\Delta V = 0$)

$$K_0 = T\left(\frac{k}{q}\right)^2\int\left(\frac{E-E_F}{kT}\right)^2 G'(E)\,dE\,, \ [\mathrm{W/K}] \tag{65d}$$

where current I is defined to be positive when it flows outside into contact 2 with electrons flowing towards. The heat current I_Q is positive when it flows in the $+x$ direction out of contact 2.

Equations (65) for long diffusive resistors can be written in the common form used to describe bulk transport as

$$J_x = \sigma\frac{d\left(E_F/q\right)}{dx} - s_T\frac{dT}{dx}\,. \ [\mathrm{A/m^2}] \tag{66a}$$

$$J_{Qx} = T\,s_T\frac{d(E_F/q)}{dx} - \kappa_0\frac{dT}{dx} \ [\mathrm{W/m^2}] \tag{66b}$$

with three specific transport coefficients

$$\sigma = \int \sigma'(E)\,dE\,, \tag{66c}$$

$$\sigma'(E) = \frac{2q^2}{h}M_{3D}(E)\lambda(E)\left(-\frac{\partial f_0}{\partial E}\right), \ [1/\Omega\cdot\mathrm{m}\cdot\mathrm{J}]$$

$$s_T = -\frac{k}{q}\int\left(\frac{E-E_F}{kT}\right)\sigma'(E)dE\,, \ [\mathrm{A/m\cdot K}] \tag{66d}$$

$$\kappa_0 = T\left(\frac{k}{q}\right)^2\int\left(\frac{E-E_F}{kT}\right)^2\sigma'(E)dE\,. \ [\mathrm{W/m\cdot K}] \tag{66e}$$

These equations have the same form for 1D and 2D resistors, but the units of the various terms differ.

The inverted form of Eqs (65) is often preferred in practice, namely:

$$\Delta V = RI - S\Delta T\,, \tag{67a}$$

$$I_Q = -\Pi I - K\Delta T\,, \tag{67b}$$

where

$$S = S_T / G\,, \tag{67c}$$

$$\Pi = TS\,, \tag{67d}$$

$$K = K_0 - \Pi SG\,. \tag{67d}$$

In this form of the equations, the contributions from each energy mode are not added, e.g. $R \neq \int R(E)dE$.

Similarly, the inverted form of the bulk transport equations (66) become

$$\frac{d(E_F / q)}{dx} = \rho J_x + S\frac{dT}{dx}\,, \tag{68a}$$

$$J_{Qx} = TSJ_x - \kappa\frac{dT}{dx} \tag{68b}$$

with transport coefficients

$$\rho = 1/\sigma\,, \tag{68c}$$

$$S = s_T / \sigma\,, \tag{68d}$$

$$\kappa = \kappa_0 - S^2\sigma T\,, \tag{68e}$$

In summary, when a band structure is given, number of modes can be evaluated from Eqs (18) and, if a model for the mean-free-path for backscattering $\lambda(E)$ can be chosen, then the near-equilibrium transport coefficients can be evaluated using the expressions listed above.

2.1. Heat transfer by phonons

Electrons transfer both charge and heat. Electrons carry most of the heat in metals. In semiconductors electrons carry only a part of the heat, but most of the heat is carried by phonons.

The phonon heat flux is proportional to the temperature gradient

$$J_{Qx}^{ph} = -\kappa_L\frac{dT}{dx}\ \ [\mathrm{W/m^2}] \tag{69}$$

with coefficient κ_L known as the specific lattice thermal conductivity. Such an exceptional thermal conductor like diamond has $\kappa_L \approx 2\cdot 10^3$ W/m·K while such a poor thermal conductor like glass has $\kappa_L \approx 1$ W/m·K. Note that electrical conductivities of solids vary over more than 20 orders of magnitude, but thermal conductivities of solids vary over a range of only 3 – 4 orders of magnitude. We will see that the same methodology used to describe electron transport can be also used for phonon transport. We will also discuss the differences between electron and phonon transport.

To describe the phonon current, we need an expression like for the electron current (63) written now as

$$I = \frac{2q}{h}\int T_{el}(E)M_{el}(E)\left(f_1 - f_2\right)dE\,. \tag{70}$$

For electrons the states in the contacts were filled according to the equilibrium Fermi functions, but phonons obey the Bose statistics, thus the phonon states in the contacts are filled according to the equilibrium Bose – Einstein distribution

$$n_0(\hbar\omega) = \frac{1}{e^{\hbar\omega/kT} - 1}\,. \tag{71}$$

Let the temperatures for the left and right contacts be T_1 and T_2. As for the electrons, both contacts are assumed ideal. Thus, the phonons that enter a contact are not able to reflect back, and transmission coefficient $T_{ph}(E)$ describes the phonon transmission across the entire channel.

It is easy now to rewrite Eq. (70) for the phonon heat current. Electron energy E we replace by the phonon energy $\hbar\omega$. In the electron current we have charge q moving in the channel, in case of the phonon current the quantum of energy $\hbar\omega$ is moving instead; thus, we replace q in (70) by $\hbar\omega$ and move it inside the integral. The coefficient 2 in (70) reflects the spin degeneracy of electron. In the case of phonons we remove this coefficient, and instead of the number of phonon polarization types that contribute to the heat flow we include it to the number of phonon modes $M_{ph}(\hbar\omega)$. Finally, the heat current due to phonons is

$$Q = \frac{1}{h}\int(\hbar\omega)T_{ph}(\hbar\omega)M_{ph}(\hbar\omega)\left(n_1 - n_2\right)d(\hbar\omega)\,. \quad [W] \tag{72}$$

In the linear response regime by analogy with (50)

$$n_1 - n_2 \approx -\frac{\partial n_0}{\partial T}\Delta T\,, \tag{73}$$

where the derivative according to (71)

$$\frac{\partial n_0}{\partial T} = \frac{\hbar\omega}{T}\left(-\frac{\partial n_0}{\partial(\hbar\omega)}\right), \tag{74}$$

with

$$\frac{\partial n_0}{\partial(\hbar\omega)} = \left(-\frac{1}{kT}\right)\frac{e^{\hbar\omega/kT}}{(e^{\hbar\omega/kT} - 1)^2}\,. \tag{75}$$

Now Eq. (72) for small differences in temperature becomes

$$Q = -K_L\,\Delta T\,, \tag{76}$$

where the thermal conductance

$$K_L = \frac{k^2 T}{h} \int T_{ph}(\hbar\omega) M_{ph}(\hbar\omega) \left[\left(\frac{\hbar\omega}{kT} \right)^2 \left(-\frac{\partial n_0}{\partial(\hbar\omega)} \right) \right] d(\hbar\omega) . \quad [W/K] \tag{77}$$

Equation (52) is simply the Fourier's law stating that heat flows down to a temperature gradient. It is also useful to note that the thermal conductance (53) displays certain similarities with the electrical conductance

$$G = \frac{2q^2}{h} \int T_{el}(E) M_{el}(E) \left(-\frac{\partial f_0}{\partial E} \right) dE . \tag{78}$$

The derivative

$$W_{el}(E) \equiv \left(-\frac{\partial f_0}{\partial E} \right) \tag{79}$$

known as the Fermi window function cutting out only those conduction modes which contribute to electric current. The electron windows function is normalized:

$$\int_{-\infty}^{+\infty} \left(-\frac{\partial f_0}{\partial E} \right) dE = 1 . \tag{80}$$

In case of phonons the term in square brackets of Eq.(53) acts as a window function specifying which modes carry the heat current. After normalization

$$W_{ph}(\hbar\omega) = \frac{3}{\pi^2} \left(\frac{\hbar\omega}{kT} \right) \left(\frac{\partial n_0}{\partial(\hbar\omega)} \right) ; \tag{81}$$

thus finally

$$K_L = \frac{\pi^2 k^2 T}{3h} \int T_{ph}(\hbar\omega) M_{ph}(\hbar\omega) W_{ph}(\hbar\omega) d(\hbar\omega) \tag{82}$$

with

$$g_0 \equiv \pi^2 k^2 T / 3h \approx (9.456 \times 10^{-13}\ W / K^2) T , \tag{83}$$

known as the quantum of thermal conductance experimentally observed first in 2000 [19].

Comparison of Eq. (54) and Eq. (58) shows that the electrical and thermal conductances are similar in structure: both are proportional to corresponding quantum of conductance times an integral over the transmission times the number of modes times a window function.

The thermal broadening functions for electrons and phonons have similar shapes and each has a width of a few kT. In case of electrons this function is given by Eq.(22) or

$$F_T(x) \equiv \frac{e^x}{\left(e^x + 1 \right)^2} \tag{84}$$

with $x \equiv (E - E_F) / kT$ and shown in Fig. 2. This function for phonons is given by Eq.(57) or

$$F_T^{ph}(x) \equiv \frac{3}{\pi^2} \frac{x^2 e^x}{\left(e^x - 1\right)^2} \tag{85}$$

with $x \equiv \hbar\omega / kT$. Both functions are normalized to a unity and shown together in Fig. 2.

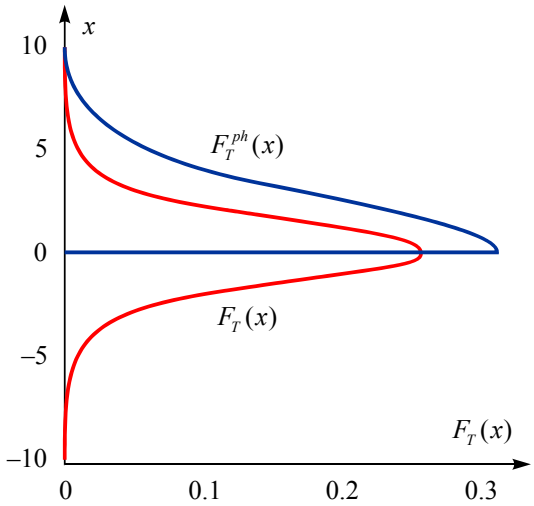

Fig. 2. Broadening function for phonons compared to that of electrons.

Along with the number of modes determined by the dispersion relation, these two window functions play a key role in determining the electrical and thermal conductivities.

Conclusions

In summary, we see that the LDL concept used to describe electron transport can be generalized for phonons. In both cases the Landauer approach generalized and extended by Datta and Lundstom gives correct quantitative description of transport processes for resistors of any nature, any dimension and size in ballistic, quasi-ballistic, and diffusive linear response regimes when there are differences in both voltage and temperature across the device. We saw that the lattice thermal conductivity can be written in the form that is very similar to the electrical conductivity, but there are two important differences.

The first difference between electrons and phonons is the difference in bandwidths of their dispersions. For electrons, the dispersion $BW \gg kT$ at room temperature, so only low energy states are occupied. For phonons, $BW \approx kT$, so at room temperature all of the acoustic modes across the entire Brillouin zone are occupied. As a result, the simple Debye approximation to the acoustic phonon dispersion does not work, almost as the simple effective mass approximation to the electron dispersion.

The second difference between electrons and phonons is that for electrons the mode populations are controlled by the window function which depends on the position of the Fermi level and the temperature. For phonons, the window function depends on the temperature only. The result is that electrical conductivities vary over many orders of magnitude, as the position of the Fermi level varies, while lattice conductivities vary over only a few orders of magnitude.

References

1. R. Landauer, *IBM J. Res. Dev*. **1**, 223 (1957).
2. R. Landauer, *J. Math. Phys*. **37**, 5259 (1996).
3. R. Landauer, *Philos. Mag*. **21**, 863 (1970).
4. S. Datta, *Lessons from Nanoelectronics: A New Perspective on Transport* (World Scientific, Singapore, 2012).
5. M. Lundstrom, J. Changwook, *Near-Equilibrium Transport: Fundamentals and Applications* (World Scientific, Singapore, 2013).
6. Yu. A. Kruglyak, *Nanosystems, Nanomaterials, Nanotechnologies*, **11**, 519 (2013); Erratum, **12**, 415 (2014).
7. Yu. A. Kruglyak, *ScienceRise*, **5:** N 3(5), 21 (2014).
8. C. Gang, *Nanoscale Energy Transport and Conversion: A Parallel Treatment of Electrons, Molecules, Phonons, and Photons* (Oxford University Press, New York, 2005).
9. Yu. A. Kruglyak, N.Yu. Kruglyak, M.V. Strikha, Sensor Electronics Microsys. Techn. **9**: N 4, 5 (2012).
10. Yu. A. Kruglyak, J. Nano- Electron. Phys. **5**: N 1, 01023 (2013).
11. Yu. A. Kruglyak, *Physics in Higher Education*, **19:** N 3, 99 (2013).
12. Yu. A. Kruglyak, Visnyk Odessa State Environ. Univ. N 15, 213 (2013).
13. C. Jeong, R. Kim, M. Luisier, S. Datta, and M. Lundstrom, *J. Appl. Phys.* **107**, 023707 (2010).
14. Yu. A. Kruglyak, *Physics in Higher Education*, **19:** N 2, 161 (2013).
15. Yu. A. Kruglyak, *Nanosystems, Nanomaterials, Nanotechnologies*, **11**, 655 (2013)
16. H. C. Berg, *Random Walks in Biology* (Princeton University Press, Princeton, 1993)
17. Yu. A. Kruglyak, *Physics in Higher Education*, **19:** N 1, 50 (2013).
18. L. I. Anatychuk, P. V. Gorsky, V. P. Mikhalchenko, *J. Thermoelectricity*, N 1, 5 (2014).
19. K. Schwab, E.A. Henriksen, J. M. Worlock, and M. L. Roukes, *Nature*, **404**, 974 (2000).

Submitted 21.11.2014

Yu. A. Kruglyak

Department of Information Technologies, Odessa State Environmental University, 15, Lvivska Str., Odessa, 65016, Ukraine

Yu. A. Kruglyak

ELECTRIC CURRENT, THERMOCURRENT, AND HEAT FLUX IN NANO- AND MICROELECTRONICS: SELECTED TOPICS

The modern Landauer – Datta – Lundstrom (LDL) electron and heat transport model was briefly summarized in [1], namely: if a band structure is chosen analytically or numerically, the number of conduction modes can be evaluated and, if a model for a mean-free-path for backscattering can be established, then the near-equilibrium thermoelectric transport coefficients can be calculated for 1D, 2D, and 3D resistors of any size in ballistic, quasi-ballistic, and diffusive linear response regimes when there are differences in both voltage and temperature across the device.

The following topics are discussed now in the LDL approach: bipolar conductivity, thermal conductivity of the bulk conductors, specific heat versus thermal conductivity, Debye model, phonon scattering, lattice thermal conductivity versus temperature, difference between lattice thermal and electrical conductivities, lattice thermal conductivity quantization.

Appendices give final expressions of thermoelectric transport coefficients through the Fermi – Dirac integrals for 1D, 2D, and 3D resistors with parabolic band structure and for 2D graphene linear dispersion in ballistic and diffusive regimes with the power law scattering.

Keywords: nanoelectronics, microelectronics, bipolar conductivity, thermal conductivity, Debye model, near-equilibrium transport, phonon scattering, thermal conductivity quantization, thermoelectric transport coefficients.

Introduction

The modern Landauer – Datta – Lundstrom (LDL) electron and heat transport model was briefly summarized in [1]. The LDL model is based on three concepts: conductivity modes $M(E)$, transmission coefficients $T(E)$, Fermi conductivity windows for electrons $(-\partial f_0/\partial E)$ and corresponding expression for phonons proportional to $(-\partial n_0/\partial E)$, where $f_0(E)$ and $n_0(E)$ are Fermi and Bose functions. These window functions are responsible for selecting those electron and phonon conduction modes which only contribute to the electric current and heat flow under the low bias conditions.

The following topics are discussed in the LDL approach below: bipolar conductivity, thermal conductivity of the bulk conductors, specific heat versus thermal conductivity, Debye model, phonon scattering, temperature dependence of the lattice thermal conductivity, difference between lattice thermal and electrical conductivities, lattice thermal conductivity quantization.

In summary, given a band structure dispersion, the number of modes can be evaluated and, if a model for a mean-free-path for backscattering $\lambda(E)$ can be established, then the near-equilibrium transport

coefficients can be calculated using final expressions listed in Appendices where we collect practically useful final expressions for thermoelectric transport coefficients through the Fermi – Dirac integrals for 1D, 2D, and 3D resistors with parabolic band structure and for 2D graphene linear dispersion case in ballistic and diffusive regimes with the power law scattering.

1. Bipolar conduction

Let us consider a 3D semiconductor with parabolic dispersion. For the conduction band

$$M_{3D}^{(c)}(E) = g_v \frac{m_n^*}{2\pi\hbar^2}(E - E_C) \quad (E \geq E_C) \tag{1a}$$

and for the valence band

$$M_{3D}^{(v)}(E) = g_v \frac{m_p^*}{2\pi\hbar^2}(E_V - E) \quad (E \leq E_V)\,. \tag{1b}$$

The conductivity [1] is provided with two contributions: for the conduction band

$$\sigma_n = \frac{q^2}{h}\int_{E_C}^{\infty} M_{3D}^{(c)}(E)\lambda_n(E)\left(-\frac{\partial f_0}{\partial E}\right)dE \tag{2a}$$

and for the valence band

$$\sigma_p = \frac{q^2}{h}\int_{-\infty}^{E_V} M_{3D}^{(v)}(E)\lambda_p(E)\left(-\frac{\partial f_0}{\partial E}\right)dE\,. \tag{2b}$$

The Seebeck coefficient S_n for electrons in the conduction band follows from eqs (66) in [1]:

$$\sigma_n = \int_{E_C}^{\infty} \sigma_n'(E)dE\,, \tag{3a}$$

$$\sigma_n'(E) = \frac{2q^2}{h} M_{3D}^{(c)}(E - E_C)\lambda_n(E)\left(-\frac{\partial f_0}{\partial E}\right), \tag{3b}$$

$$s_T^{(c)} = -\frac{k}{q}\int_{E_C}^{\infty}\left(\frac{E - E_F}{kT}\right)\sigma_n'(E)\,dE\,, \tag{3c}$$

$$S_n = s_T^{(c)} / \sigma_n\,. \tag{3d}$$

Similarly, S_p for electrons in the valence band we have:

$$\sigma_p = \int_{-\infty}^{E_V} \sigma_p'(E)dE\,, \tag{4a}$$

$$\sigma'_p(E) = \frac{2q^2}{h} M_{3D}^{(v)}(E_V - E)\lambda_p(E)\left(-\frac{\partial f_0}{\partial E}\right), \tag{4b}$$

$$s_T^{(v)} = -\frac{k}{q}\int_{-\infty}^{E_V}\left(\frac{E - E_F}{kT}\right)\sigma'_p(E)\,dE, \tag{4c}$$

$$S_p = s_T^{(v)} / \sigma_p, \tag{4d}$$

but the sign of S_p will be positive.

What is going on when both the conduction and valence bands contribute to conduction? This can happen for a narrow bandgap conductors or at high temperatures. In such a case, we have to simply integrate over all the modes and will find

$$\sigma^{tot} \equiv \sigma_n + \sigma_p = \frac{q^2}{h}\int_{E_1}^{E_2} M_{3D}^{tot}(E)\lambda(E)\left(-\frac{\partial f_0}{\partial E}\right)dE, \tag{5a}$$

$$M_{3D}^{tot}(E) = M_{3D}^{(c)}(E) + M_{3D}^{(v)}(E). \tag{5b}$$

Moreover, we have not be worried about integrating to the top of the conduction band or from the bottom of the valence band because the Fermi function ensures that the integrand falls exponentially to zero away from the band edge. What is important that in both cases we integrate the same expression with the appropriate $M_{3D}(E)$ and $\lambda(E)$ over the relevant energy difference $E_2 - E_1$. Electrons carry current in both bands. Our general expression is the same for the conduction and valence bands. There is no need to change signs for the valence band or to replace $f_0(E)$ with $1 - f_0(E)$.

To calculate the Seebeck coefficient when both bands contribute let us remind that in the first direct form of the transport coefficients (66) of [1] the contributions from each mode are added in parallel so the total specific Soret coefficient

$$s_T^{tot} = -\frac{k}{q}\int_{-\infty}^{+\infty}\left(\frac{E - E_F}{kT}\right)\sigma'(E)dE = S_n\sigma_n + S_p\sigma_p; \tag{6a}$$

then the Seebeck coefficient for bipolar conduction

$$S^{tot} = \frac{S_n\sigma_n + S_p\sigma_p}{\sigma_n + \sigma_p}. \tag{6b}$$

Since the Seebeck coefficients for the conduction and valence bands have opposite signs the total Seebeck coefficient just drops for high temperatures and the performance of a thermoelectrical device falls down.

2. Thermal conductivity of the bulk conductors

The thermal conductivity of a large diffusive resistor is a key material property that controls

performance of any electronic devices. By analogy with the transmission coefficient (39) in [1] for electron transport the phonon transmission

$$T_{ph}(\hbar\omega) = \frac{\lambda_{ph}(\hbar\omega)}{\lambda_{ph}(\hbar\omega) + L}\Big|_{L \gg \lambda_{ph}} \to \frac{\lambda_{ph}(\hbar\omega)}{L}. \tag{7}$$

It is also obvious that for large 3D conductors the number of phonon modes is proportional to the cross-sectional area of the sample:

$$M_{ph}(\hbar\omega) \propto A, \tag{8}$$

Now let us return to eqn (76) of [1] dividing and multiplying it by *A/L*, which immediately gives eqn (69) over there for the phonon heat flux postulated in [1]

$$\frac{Q}{A} \equiv J_{Qx}^{ph} = -\kappa_L \frac{dT}{dx} \tag{9}$$

with specific lattice thermal conductivity

$$\kappa_L = K_L \frac{L}{A}, \tag{10}$$

or substituting (7) above to (82) of [1] one for the lattice thermal conductivity finally obtains

$$\kappa_L = \frac{\pi^2 k^2 T}{3h} \int \frac{M_{ph}(\hbar\omega)}{A} \lambda_{ph}(\hbar\omega) W_{ph}(\hbar\omega)\, d(\hbar\omega). \tag{11}$$

It is useful now to define the average number of phonon modes per cross-sectional area of the conductor that participate in the heat transport

$$\left\langle M_{ph} / A \right\rangle \equiv \int \frac{M_{ph}(\hbar\omega)}{A} W_{ph}(\hbar\omega)\, d(\hbar\omega). \tag{12}$$

Then

$$\kappa_L = \frac{\pi^2 k^2 T}{3h} \left\langle M_{ph} / A \right\rangle \left\langle \left\langle \lambda_{ph} \right\rangle \right\rangle, \tag{13}$$

where the average mean-free-path is defined now as

$$\left\langle \left\langle \lambda_{ph} \right\rangle \right\rangle = \frac{\int \frac{M_{ph}(\hbar\omega)}{A} \lambda_{ph}(\hbar\omega) W_{ph}(\hbar\omega)\, d(\hbar\omega)}{\int \frac{M_{ph}(\hbar\omega)}{A} W_{ph}(\hbar\omega)\, d(\hbar\omega)}. \tag{14}$$

Thus, the couple of the phonon transport equations (9) and (13) corresponds to similar electron transport equations:

$$J_x = \frac{\sigma}{q} \frac{d\left(E_F\right)}{dx}, \tag{15}$$

$$\sigma = \frac{2q^2}{h}\langle M_{el} / A\rangle\langle\langle \lambda_{el} \rangle\rangle . \tag{16}$$

The thermal conductivity (13) and the electrical conductivity (16) have the same structure. It is always a product of the corresponding quantum of conductance times the number of modes that participate in transport, times the average mean-free-path. These three quantities for phonons will be discussed later.

3. Specific heat versus thermal conductivity

The connection between the lattice specific thermal conductivity and the lattice specific heat at constant volume is well known [2 – 5]. We will show now that corresponding proportionality coefficient is a product of an appropriately-defined mean-free-path $\langle\langle \Lambda_{ph} \rangle\rangle$ and an average phonon velocity $\langle v_{ph} \rangle$, namely:

$$\kappa_L = \frac{1}{3}\langle\langle \Lambda_{ph} \rangle\rangle\langle v_{ph} \rangle C_V . \tag{17}$$

The total phonon energy per unit volume

$$E_{ph} = \int_0^\infty (\hbar\omega) D_{ph}(\hbar\omega) n_0(\hbar\omega) d(\hbar\omega) , \tag{18}$$

where $D_{ph}(\hbar\omega)$ is the phonon density of states. By definition,

$$\begin{aligned} C_V \equiv \frac{\partial E_{ph}}{\partial T} = \frac{\partial}{\partial T}\int_0^\infty (\hbar\omega) D_{ph}(\hbar\omega) n_0(\hbar\omega) d(\hbar\omega) = \\ = \int_0^\infty (\hbar\omega) D_{ph}(\hbar\omega)\left(\frac{\partial n_0(\hbar\omega)}{\partial T}\right) d(\hbar\omega) = \frac{\pi^2 k^2 T}{3}\int_0^\infty D_{ph}(\hbar\omega) W_{ph}(\hbar\omega) d(\hbar\omega) \end{aligned} . \tag{19}$$

where eqs (74) and (81) of [1] were used. Next, multiply and divide (11) by (19) and obtain proportionality we are looking for:

$$\kappa_L = \left[\frac{\frac{1}{h}\int_0^\infty \frac{M_{ph}(\hbar\omega)}{A}\lambda_{ph}(\hbar\omega) W_{ph}(\hbar\omega) d(\hbar\omega)}{\int_0^\infty D_{ph}(\hbar\omega) W_{ph}(\hbar\omega) d(\hbar\omega)}\right] C_V . \tag{20}$$

To obtain final expression (17) and correct interpretation of the proportionality coefficient we need to return to eqn (7). This expression can be easily derived for 1D conductor with several simplifying assumptions. Nevertheless it works very well in practice for a conductor of any dimension. Derivation of eqn (7) is based on the interpretation of the mean-free-path $\lambda(E)$ or $\lambda(\hbar\omega)$ as that its inverse is the probability per unit length that a positive flux is converted to a negative flux. This is why λ is often called a mean-free-path for backscattering. Let us relate it to

the scattering time τ. The distinction between mean-free-path and mean-free-path for backscattering is easiest to see for 1D conductor. Let electron undergoes a scattering event. For isotropic scattering the electron can forward scatter or back scatter. Only backscattering is relevant for the mean-free-path for scattering, so the time between backscattering events is 2τ. Thus the mean-free-path for backscattering is twice the mean-free-path for scattering

$$\lambda_{1D}(E) = 2\Lambda(E) = 2v(E)\tau(E). \tag{21a}$$

It was shown that the proper definition of the mean-free-path for backscattering for a conductor of any dimension [6]

$$\lambda(E) = 2\frac{\left\langle v_x^2\tau\right\rangle}{\left\langle |v_x|\right\rangle},$$

where averaging is performed over angles. For isotropic bands

$$\lambda_{2D}(E) = \frac{\pi}{2}v(E)\tau(E), \tag{21b}$$

$$\lambda_{3D}(E) = \frac{4}{3}v(E)\tau(E). \tag{21c}$$

The scattering time is often approximately written as the power law scattering

$$\tau(E) = \tau_0\left(\frac{E-E_C}{kT}\right)^s, \tag{22}$$

where exponent *s* describes the specific scattering mechanism: for acoustic phonon scattering in 3D conductor with parabolic dispersion $s=-1/2$, and for ionized impurity scattering $s=+3/2$ [7].

Analogous power law is often used for mean-free-path:

$$\lambda(E) = \lambda_0\left(\frac{E-E_C}{kT}\right)^r. \tag{23}$$

For parabolic zone structure $v(E)\propto E^{1/2}$, thus $r=s+1/2$ with $r=0$ for acoustic phonon scattering, and $r=2$ for ionized impurity scattering.

Coming back to our initial task to derive (17) from (20) for 3D conductor according (21c) we have

$$\lambda_{ph}(\hbar\omega) = \frac{4}{3}v_{ph}(\hbar\omega)\tau_{ph}(\hbar\omega), \tag{24}$$

where according to (21a),

$$v_{ph}(\hbar\omega)\tau_{ph}(\hbar\omega) = \Lambda_{ph}(\hbar\omega), \tag{25}$$

and finally

$$\lambda_{ph}(\hbar\omega) = \frac{4}{3}\Lambda_{ph}(\hbar\omega)\,. \tag{26}$$

It was stated above in (18) of [1] that the density of states and number of modes for electrons in 3D:

$$M_{el}(E) = AM_{3D}(E) = A\frac{h}{4}\left\langle v_x^+(E)\right\rangle D_{3D}(E)\,. \tag{27}$$

Let us rewrite this formulae for phonons. Note that the spin degeneracy for electrons $g_S = 2$ is included to the density of states

$$D_{3D}(E) = 2D'_{3D}(E)\,, \tag{28}$$

and for spherical bands in 3D conductor

$$\left\langle v_x^+(E)\right\rangle = \frac{v_{el}(E)}{2}\,. \tag{29}$$

Collecting (27) up to (29) all together in case of phonons we have

$$M_{ph}(\hbar\omega) = A\frac{h}{2}\left(\frac{v_{ph}(\hbar\omega)}{2}\right)2D_{ph}(\hbar\omega) = A\frac{h}{4}v_{ph}(\hbar\omega)D_{ph}(\hbar\omega)\,. \tag{30}$$

Substituting (26) and (30) to (20) we obtain

$$\kappa_L = \left[\frac{\frac{1}{3}\int_0^\infty \Lambda_{ph}(\hbar\omega)v_{ph}(\hbar\omega)D_{ph}(\hbar\omega)W_{ph}(\hbar\omega)d(\hbar\omega)}{\int_0^\infty D_{ph}(\hbar\omega)W_{ph}(\hbar\omega)d(\hbar\omega)}\right]C_V\,. \tag{31}$$

Multiplying and dividing (31) by

$$\int_0^\infty v_{ph}(\hbar\omega)D_{ph}(\hbar\omega)W_{ph}(\hbar\omega)d(\hbar\omega)\,, \tag{32}$$

we finally get eqn (17) with proportionality coefficient between κ_L and C_V as the product of an average mean-free-path as

$$\left\langle\left\langle\Lambda_{ph}\right\rangle\right\rangle \equiv \frac{\int_0^\infty \Lambda_{ph}(\hbar\omega)v_{ph}(\hbar\omega)D_{ph}(\hbar\omega)W_{ph}(\hbar\omega)d(\hbar\omega)}{\int_0^\infty v_{ph}(\hbar\omega)D_{ph}(\hbar\omega)W_{ph}(\hbar\omega)d(\hbar\omega)} \tag{33}$$

and an average velocity as

$$\left\langle v_{ph}\right\rangle \equiv \frac{\int_0^\infty v_{ph}(\hbar\omega)D_{ph}(\hbar\omega)W_{ph}(\hbar\omega)d(\hbar\omega)}{\int_0^\infty D_{ph}(\hbar\omega)W_{ph}(\hbar\omega)d(\hbar\omega)}\,, \tag{34}$$

with the appropriate averaging.

Equation (17) is often used to estimate the average mean-free-path from the measured κ_L and C_V, if we know the average velocity, which is frequently assumed to be the longitudinal sound velocity. The derivation above has identified the precise definitions of the $\left\langle\left\langle \Lambda_{ph} \right\rangle\right\rangle$ and $\left\langle v_{ph} \right\rangle$. If a phonon dispersion is chosen one can always compute the average velocity according to (34), and it is typically very different from the longitudinal sound velocity. Thus, estimates of the average mean-free-path can be quite wrong if one assumes the longitudinal sound velocity [8].

4. Debye model

For 3D conductors there are three polarization states for lattice vibrations: one for atoms displaced in the direction of propagation (longitudinal/L) and two for atoms displaced orthogonal to the direction of propagation (transverse/T). The low energy modes are called acoustic modes/A: one LA mode analogous to sound waves propagating in air and two TA modes. Near $q \to 0$ dispersion of acoustic modes is linear

$$\hbar\omega = \hbar v_D q\,, \tag{35}$$

and known as Debye approximation. The Debye velocity v_D is an average velocity of the L and T acoustic modes. In case of LA mode v_D is simply the sound velocity $v_s \propto m^{-1/2}$ with m being an effective mass of vibrating atom. Typical $v_s \approx 5\times10^3$ m/s, about 20 times slower that the velocity of a typical electron.

The bandwidth of the electronic dispersion is typically $BW \gg kT$, so only states near the bottom of the conduction band where the effective mass model is reasonably accurate are occupied. For phonons the situation is much different; the bandwidth $BW \approx kT$, so states across the entire Brillouin zone are occupied. The widely-used Debye approximation (35) fits the acoustic branches as long as q is not too far from the center of the Brillouin zone.

With the Debye approximation (35) it is easy to find the density of the phonon states

$$D_{ph}(\hbar\omega) = \frac{3(\hbar\omega)^2}{2\pi^2(\hbar v_D)^3}\,,\ [\mathrm{J}^{-1}\cdot\mathrm{m}^{-3}] \tag{36}$$

where the factor of three is for the three polarizations. Then one can obtain the number of phonon modes per cross-sectional area from eqn (30):

$$M_{ph}(\hbar\omega) = \frac{3(\hbar\omega)^2}{4\pi(\hbar v_D)^2}\,. \tag{37}$$

Since all the states in the Brillouin zone tend to be occupied at moderate temperatures, we are to be sure that we account the correct number of states. For a crystal there are $3N/\Omega$ states per unit volume. To find the total number of states we have to integrate the density-of-states

$$\int_0^{\hbar\omega_D} D_{ph}(\hbar\omega)\, d(\hbar\omega), \tag{38}$$

with the upper limit as $\hbar$ times the so-called Debye frequency to produce the correct number of states, namely:

$$\hbar\omega_D = \hbar v_D \left(\frac{6\pi^2 N}{\Omega} \right)^{1/3} \equiv kT_D . \tag{39}$$

The Debye frequency defines a cutoff frequency above which no states are accounted for. This restriction can also be expressed via a cutoff wavevector q_D or as a Debye temperature

$$T_D = \hbar\omega / k . \tag{40}$$

For $T \ll T_D$ only states with $q \to 0$ for which the Debye approximation is accurate are occupied.

Now we can calculate the lattice thermal conductivity by integrating (11) to the Debye cutoff energy

$$\kappa_L = \frac{\pi^2 k^2 T}{3h} \int_0^{\hbar\omega_D} \frac{M_{ph}(\hbar\omega)}{A} \lambda_{ph}(\hbar\omega) W_{ph}(\hbar\omega)\, d(\hbar\omega) \tag{41}$$

and estimate $M_{ph}(\hbar\omega)$ according to (11). The integral can be taken numerically or analytically if appropriate expression for the mean-free-path is used. This is how the lattice thermal conductivities were first calculated [9, 10]. The theory and computational procedures for the thermoelectric transport coefficients were developed further in [6, 8, 11].

5. Phonon scattering

Phonons can scatter from defects, impurity atoms, isotopes, surfaces and boundaries, electrons, and from other phonons. Phonon-phonon scattering occurs because the potential energy of the bonds in the crystal are not exactly harmonic. All higher order terms are treated as a scattering potential. Two types of phonon scattering are considered. In the normal process two phonons interact and create a third phonon with energy and momentum being conserved:

$$\begin{aligned} \hbar\vec{q}_1 + \hbar\vec{q}_2 &= \hbar\vec{q}_3 \\ \hbar\vec{w}_1 + \hbar\vec{w}_2 &= \hbar\vec{w}_3 \end{aligned} . \tag{42}$$

The total momentum of the phonon ensemble is conserved, thus this type of scattering has little effect on the heat flux.

In a second type of scattering, umklapp/U-scattering the two initial phonons have larger momentum, thus the resulting phonon would have a momentum outside the Brillouin zone due to unharmonic phonon-phonon as well as electron-phonon interactions. The U-scatterings are the basic processes in the heat transport especially at high temperatures. Scattering on defects/D and on boundaries/B are also important. Scattering rates add, thus the total phonon scattering rate is

$$\frac{1}{\tau_{ph}(\hbar\omega)} = \frac{1}{\tau_U(\hbar\omega)} + \frac{1}{\tau_D(\hbar\omega)} + \frac{1}{\tau_B(\hbar\omega)} \tag{43}$$

or alternatively in terms of the mean-free-path (24)

$$\frac{1}{\lambda_{ph}(\hbar\omega)} = \frac{1}{\lambda_U(\hbar\omega)} + \frac{1}{\lambda_D(\hbar\omega)} + \frac{1}{\lambda_B(\hbar\omega)}, \tag{44}$$

Expressions for each of the scattering rates are developed [12]. For scattering from point defects

$$\frac{1}{\tau_D(\hbar\omega)} \propto \omega^4, \tag{45}$$

known as the Rayleigh scattering which is like the scattering of light from the dust.

For boundaries and surfaces

$$\frac{1}{\tau_B(\hbar\omega)} \propto \frac{v_{ph}(\hbar\omega)}{L}, \tag{46}$$

where L is the shortest dimension of the sample.

A commonly used expression for U-scattering is

$$\frac{1}{\tau_U(\hbar\omega)} \propto T^3\omega^2 e^{-T_D/bT}. \tag{47}$$

With this background we are now able to understand the temperature dependence of the lattice thermal conductivity.

6. Lattice thermal conductivity versus temperature

The temperature dependence of the lattice thermal conductivity κ_L is illustrated for bulk *Si* on Fig. 1.

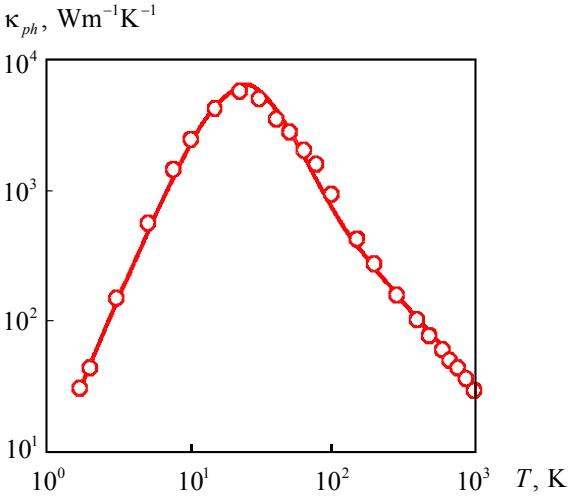

Fig. 1. The experimental [13] and calculated [8] thermal conductivity of bulk Si as a function of temperature.

According to eqn (13) κ_L is proportional to the number of the phonon modes that are occupied $\langle M_{ph} / A \rangle$ and to the average value of the phonon mean-free-path $\langle\langle \lambda_{ph} \rangle\rangle$. The curve $\kappa_L(T)$ can be explained by understanding how $\langle M_{ph} \rangle$ and $\langle\langle \lambda_{ph} \rangle\rangle$ vary with temperature.

It can be shown using eqn (12) that at low temperatures

$$\langle M_{ph} \rangle \propto T^3, \quad (T \to 0) \tag{48}$$

so the initial rise in thermal conductivity is due to the fact that the number of populated modes rises quickly with temperature. At low temperatures boundary scattering is important. As the temperature increases more short-wave-length phonons are produced. These phonons scatter from point defects, so defect scattering becomes more and more important. As the temperature approaches the T_D, all of the phonon modes are populated and further increases in temperature do not change $\langle M_{ph} \rangle$. Instead, the higher temperatures increase the phonon scattering by U-processes, and the thermal conductivity drops with increasing temperatures.

7. Difference between lattice thermal and electrical conductivities

We have already noted the similarity between phonon transport equations (9) and (13) and electron transport equations (15) and (16). The average electron and phonon mean-free-paths are of the same order of magnitude. Why then does the electrical conductance vary over many more orders of magnitude while the lattice thermal conductance varies only over a few? The answer lies in the corresponding windows functions (79) and (81) of [1]. For both electrons and phonons, higher temperatures broaden the window function and increase the population of states. For electrons, however, the position of the Fermi level has a dramatic effect on the magnitude of the window function. By controlling the position of the Fermi level, the electrical conductivity can be varied over many orders magnitude. For the phonons the width of the window function is determined by temperature only.

Another key difference between electrons and phonons relates to how the states are populated. For a thermoelectric device $E_F \approx E_C$, and the electron and phonon window functions are quite similar. However, for electrons the BW of the dispersion is very large, so only a few states near the bottom of the conduction band are populated: the effective mass approximation works well for these states, and it is easy to obtain analytical solutions. For phonons, the BW of the dispersion is small. At moderate temperatures states all across the entire Brillouin zone are occupied: simple analytical approximations do not work, and it is hard to get analytical solutions for the lattice thermal conductivity.

8. Lattice thermal conductivity quantization

By analogy with the electronic conduction quantization

$$G^{ball} = \frac{2q^2}{h} M(E_F), \tag{49}$$

over 30 years ago Pendry [14] stated the existence of the quantum limits to the heat flow. In fact, if $T \to 0$ in eqn (82) of [1] then the phonon window $W_{ph}(\hbar\omega)$ is sharply peaked near $\hbar\omega = 0$:

$$K_L = \frac{\pi^2 k^2 T}{3h} T_{ph}(0) M_{ph}(0). \tag{50}$$

For a bulk conductor $M_{ph}(\hbar\omega) \to 0$ as $\hbar\omega \to 0$, but for a nanoresistors like a nanowire or nanoribbon one can have a finite number of phonon modes. For ballistic phonon transport $T_{ph} = 1$ and one can expect

$$K_L = \frac{\pi^2 k^2 T}{3h} M_{ph}. \tag{51}$$

Exactly this result was proved experimentally using 4-mode resistor at T < 0.8 K [15]; thermoconductivity measurements were agree with the predictions for 1D ballistic resistors [16 – 18].

The quantum of thermal conductance

$$g_0 \equiv \pi^2 k^2 T / 3h \tag{52}$$

represents the maximum possible value of energy transported per phonon mode. Surprisingly, it does not depend on particle statistics: the quantum of thermal conductance is universal for fermions, bosons, and anyons [19 – 21].

Conclusions

As a summary of both papers [1] and the present one we state that the Landauer – Datta – Lundstrom modern electron and heat transport model works well for nano-, micro-, and macroelectronics. If a band structure is chosen analytically or numerically, the number of conduction modes can be evaluated and, if a model for a mean-free-path for backscattering can be established, then the near-equilibrium thermoelectric transport coefficients can be calculated for 1D, 2D, and 3D resistors of any size in ballistic, quasi-ballistic, and diffusive linear response regimes when there are differences in both voltage and temperature across the device.

Finally, we collect below the thermoelectric coefficients through the Fermi – Dirac integrals for parabolic band semiconductors and for graphene in ballistic and diffusive regimes [22].

Appendix A. Thermoelectric coefficients for 1D, 2D, and 3D semiconductors with parabolic dispersion for ballistic and diffusive regimes

Thermoelectric coefficients are expressed through the Fermi – Dirac integral of order *j* defined as

$$\Im_j(\eta_F)=\frac{1}{\Gamma(j+1)}\int_0^\infty\frac{\eta^j}{\exp(\eta-\eta_F)+1}\,d\eta\,,$$

where the location of the Fermi level E_F relative to the conduction band edge E_C is given by the dimensionless parameter

$$\eta_F=\frac{E_F-E_C}{kT}\,.$$

In expressions below thermoelectric coefficients for diffusive regime were calculated with the power law scattering

$$\lambda(E)=\lambda_0\left(\frac{E}{kT}\right)^r.$$

1. Thermoelectric coefficients for 1D ballistic resistors

$$G=\frac{2q^2}{h}\Im_{-1}(\eta_F);\;\; S_T=-\frac{k}{q}\frac{2q^2}{h}\left[\Im_0(\eta_F)-\eta_F\Im_{-1}(\eta_F)\right];\;\; S=-\frac{k}{q}\left[\frac{\Im_0(\eta_F)}{\Im_{-1}(\eta_F)}-\eta_F\right];$$

$$K_0=T\left(\frac{k}{q}\right)^2\frac{2q^2}{h}\left[2\Im_1(\eta_F)-2\eta_F\Im_0(\eta_F)+\eta_F^2\,\Im_{-1}(\eta_F)\right];$$

$$K=T\left(\frac{k}{q}\right)^2\frac{2q^2}{h}\left[2\Im_1(\eta_F)-\frac{\Im_0^2(\eta_F)}{\Im_{-1}(\eta_F)}\right];$$

2. Thermoelectric coefficients for 1D diffusive resistors

$$G=\frac{2q^2}{h}\left(\frac{\lambda_0}{L}\right)\Gamma(r+1)\Im_{r-1}(\eta_F);$$

$$S_T=-\frac{k}{q}\frac{2q^2}{h}\left(\frac{\lambda_0}{L}\right)\Gamma(r+1)\left[(r+1)\Im_r(\eta_F)-\eta_F\Im_{r-1}(\eta_F)\right];\; S=-\frac{k}{q}\left[\frac{(r+1)\Im_r(\eta_F)}{\Im_{r-1}(\eta_F)}-\eta_F\right];$$

$$K_0=T\left(\frac{k}{q}\right)^2\frac{2q^2}{h}\left(\frac{\lambda_0}{L}\right)\left[\Gamma(r+3)\Im_{r+1}(\eta_F)-2\eta_F\Gamma(r+2)\Im_r(\eta_F)+\eta_F^2\Gamma(r+1)\Im_{r-1}(\eta_F)\right];$$

$$K=T\left(\frac{k}{q}\right)^2\frac{2q^2}{h}\left(\frac{\lambda_0}{L}\right)\Gamma(r+2)\left[(r+2)\Im_{r+1}(\eta_F)-\frac{(r+1)\Im_r^2(\eta_F)}{\Im_{r-1}(\eta_F)}\right];$$

Conductivity $G=\sigma_{1D}/L$ is given in Siemens: $\left[\sigma_{1D}\right]=1\,\mathrm{S}\cdot\mathrm{m}$. Similarly for other specific coefficients: $s_T=S_TL;\quad \kappa_0=K_0L;\quad \kappa=KL.$

3. Thermoelectric coefficients for 2D ballistic resistors

$$G=W\frac{2q^2}{h}\frac{\sqrt{2\pi m^*kT}}{h}\Im_{-1/2}(\eta_F);$$

$$S_T=-W\frac{k}{q}\frac{2q^2}{h}\frac{\sqrt{2\pi m^*kT}}{h}\left[\frac{3}{2}\Im_{1/2}(\eta_F)-\eta_F\Im_{-1/2}(\eta_F)\right];\;\; S=-\frac{k}{q}\left[\frac{3\Im_{1/2}(\eta_F)}{2\Im_{-1/2}(\eta_F)}-\eta_F\right];$$

$$K_0 = W\,T\left(\frac{k}{q}\right)^2 \frac{2q^2}{h}\frac{\sqrt{2\pi m^* kT}}{h}\left[\frac{15}{4}\Im_{3/2}(\eta_F) - 3\eta_F\Im_{1/2}(\eta_F) + \eta_F^2\Im_{-1/2}(\eta_F)\right];$$

$$K = W\,T\left(\frac{k}{q}\right)^2 \frac{2q^2}{h}\frac{\sqrt{2\pi m^* kT}}{h}\left[\frac{15}{4}\Im_{3/2}(\eta_F) - \frac{9\Im_{1/2}^2(\eta_F)}{4\Im_{-1/2}(\eta_F)}\right];$$

4. Thermoelectric coefficients for 2D diffusive resistors

$$G = W\frac{2q^2}{h}\left(\frac{\lambda_0}{L}\right)\frac{\sqrt{2m^* kT}}{\pi h}\Gamma(r+\frac{3}{2})\Im_{r-1/2}(\eta_F);\;\; S = -\frac{k}{q}\left[\frac{(r+3/2)\Im_{r+1/2}(\eta_F)}{\Im_{r-1/2}(\eta_F)} - \eta_F\right];$$

$$S_T = -W\frac{k}{q}\frac{2q^2}{h}\left(\frac{\lambda_0}{L}\right)\frac{\sqrt{2m^* kT}}{\pi h}\left[\Gamma(r+\frac{5}{2})\Im_{r+1/2}(\eta_F) - \eta_F\Gamma(r+\frac{3}{2})\Im_{r-1/2}(\eta_F)\right];$$

$$K_0 = W\,T\left(\frac{k}{q}\right)^2 \frac{2q^2}{h}\left(\frac{\lambda_0}{L}\right)\frac{\sqrt{2m^* kT}}{\pi h}\times$$
$$\times\left[\Gamma(r+\frac{7}{2})\Im_{r+3/2}(\eta_F) - 2\eta_F\Gamma(r+\frac{5}{2})\Im_{r+1/2}(\eta_F) + \eta_F^2\Gamma(r+\frac{3}{2})\Im_{r-1/2}(\eta_F)\right];$$

$$K = W\,T\left(\frac{k}{q}\right)^2 \frac{2q^2}{h}\left(\frac{\lambda_0}{L}\right)\frac{\sqrt{2m^* kT}}{\pi h}\Gamma(r+\frac{5}{2})\left[(r+\frac{5}{2})\Im_{r+3/2}(\eta_F) - \frac{(r+\frac{3}{2})\Im_{r+1/2}^2(\eta_F)}{\Im_{r-1/2}(\eta_F)}\right];$$

Conductivity $G = \sigma_{2D}W/L$ is given in Siemens: $[\sigma_{2D}] = 1\,\mathrm{S}$. Similarly for other specific coefficients: $s_T = S_T L/W;\quad \kappa_0 = K_0 L/W;\quad \kappa = KL/W.$

5. Thermoelectric coefficients for 3D ballistic resistors

$$G = A\frac{2q^2}{h}\frac{m^* kT}{2\pi\hbar^2}\Im_0(\eta_F);\;\; S_T = -A\frac{k}{q}\frac{2q^2}{h}\frac{m^* kT}{2\pi\hbar^2}\left[2\Im_1(\eta_F) - \eta_F\Im_0(\eta_F)\right];\;\; S = -\frac{k}{q}\left[\frac{2\Im_1(\eta_F)}{\Im_0(\eta_F)} - \eta_F\right];$$

$$K_0 = AT\left(\frac{k}{q}\right)^2 \frac{2q^2}{h}\frac{m^* kT}{2\pi\hbar^2}\left[6\Im_2(\eta_F) - 4\eta_F\Im_1(\eta_F) + \eta_F^2\Im_0(\eta_F)\right];$$

$$K = AT\left(\frac{k}{q}\right)^2 \frac{2q^2}{h}\frac{m^* kT}{2\pi\hbar^2}\left[6\Im_2(\eta_F) - \frac{4\Im_1^2(\eta_F)}{\Im_0(\eta_F)}\right];$$

6. Thermoelectric coefficients for 3D diffusive resistors

$$G = A\frac{2q^2}{h}\left(\frac{\lambda_0}{L}\right)\frac{m^* kT}{2\pi\hbar^2}\Gamma(r+2)\Im_r(\eta_F);\;\; S = -\frac{k}{q}\left[\frac{(r+2)\Im_{r+1}(\eta_F)}{\Im_r(\eta_F)} - \eta_F\right];$$

$$S_T = -A\frac{k}{q}\frac{2q^2}{h}\left(\frac{\lambda_0}{L}\right)\frac{m^* kT}{2\pi\hbar^2}\left[\Gamma(r+3)\Im_{r+1}(\eta_F) - \eta_F\Gamma(r+2)\Im_r(\eta_F)\right];$$

$$K_0 = AT\left(\frac{k}{q}\right)^2 \frac{2q^2}{h}\left(\frac{\lambda_0}{L}\right)\frac{m^* kT}{2\pi\hbar^2}\left[\Gamma(r+4)\Im_{r+2}(\eta_F) - 2\eta_F\Gamma(r+3)\Im_{r+1}(\eta_F) + \eta_F^2\Gamma(r+2)\Im_r(\eta_F)\right];$$

$$K = AT\left(\frac{k}{q}\right)^2 \frac{2q^2}{h}\left(\frac{\lambda_0}{L}\right)\frac{m^* kT}{2\pi\hbar^2}\Gamma(r+3)\left[(r+3)\Im_{r+2}(\eta_F) - \frac{(r+2)\Im_{r+1}^2(\eta_F)}{\Im_r(\eta_F)}\right];$$

Conductivity $G = \sigma_{3D} A / L$ is given in Siemens: $[\sigma_{3D}] = 1$ S/m. Similarly for other specific coefficients: $s_T = S_T L / A; \quad \kappa_0 = K_0 L / A; \quad \kappa = KL / A.$

Appendix B. Thermoelectric coefficients for graphene with linear dispersion for ballistic and diffusive regimes

Graphene is a 2D conductor with a unique linear band structure $E(k) = \pm\hbar v_F k$. Its transport coefficients are calculated from eqs (65) and (67) of [1] with the number of modes given by $M(E) = W \cdot 2|E|/\pi\hbar v_F$. The power law scattering for diffusive regime is used as above.

Conductivity $G = \sigma W / L$ is given in Siemens: $[\sigma] = 1$ S. Similarly for other specific coefficients: $s_T = S_T L / W; \ \kappa_0 = K_0 L / W; \ \kappa = K L / W.$

1. Ballistic regime

$$G^{ball} = W\frac{2q^2}{h}\left(\frac{2kT}{\pi\hbar v_F}\right)\left[\Im_0(\eta_F) + \Im_0(-\eta_F)\right]; \ S^{ball} = -\frac{k}{q}\left\{\frac{2\left[\Im_1(\eta_F) - \Im_1(-\eta_F)\right]}{\Im_0(\eta_F) + \Im_0(-\eta_F)} - \eta_F\right\};$$

$$S_T^{ball} = -W\frac{2q^2}{h}\left(\frac{2kT}{\pi\hbar v_F}\right)\left(\frac{k}{q}\right)\left\{2\left[\Im_1(\eta_F) - \Im_1(-\eta_F)\right] - \eta_F\left[\Im_0(\eta_F) + \Im_0(-\eta_F)\right]\right\};$$

$$K^{ball} = WT\frac{2q^2}{h}\left(\frac{2kT}{\pi\hbar v_F}\right)\left(\frac{k}{q}\right)^2\left\{6\left[\Im_2(\eta_F) + \Im_2(-\eta_F)\right] - \frac{4\left[\Im_1(\eta_F) - \Im_1(-\eta_F)\right]^2}{\Im_0(\eta_F) + \Im_0(-\eta_F)}\right\};$$

$$K_0^{ball} = WT\frac{2q^2}{h}\left(\frac{2kT}{\pi\hbar v_F}\right)\left(\frac{k}{q}\right)^2 \times$$
$$\times\left\{6\left[\Im_2(\eta_F) + \Im_2(-\eta_F)\right] - 4\eta_F\left[\Im_1(\eta_F) - \Im_1(-\eta_F)\right] + \eta_F^2\left[\Im_0(\eta_F) + \Im_0(-\eta_F)\right]\right\}.$$

2. Diffusive regime

$$G^{diff} = W\frac{2q^2}{h}\left(\frac{2kT}{\pi\hbar v_F}\right)\left(\frac{\lambda_0}{L}\right)\Gamma(r+2)\left[\Im_r(\eta_F) + \Im_r(-\eta_F)\right];$$

$$S^{diff} = -\frac{k}{q}\left\{\frac{(r+2)\left[\Im_{r+1}(\eta_F) - \Im_{r+1}(-\eta_F)\right]}{\Im_r(\eta_F) + \Im_r(-\eta_F)} - \eta_F\right\};$$

$$S_T^{diff} = -W\frac{2q^2}{h}\frac{k}{q}\left(\frac{2kT}{\pi\hbar v_F}\right)\left(\frac{\lambda_0}{L}\right)\left\{\begin{matrix}\Gamma(r+3)\left[\Im_{r+1}(\eta_F) - \Im_{r+1}(-\eta_F)\right] - \\ -\eta_F\Gamma(r+2)\left[\Im_r(\eta_F) + \Im_r(-\eta_F)\right]\end{matrix}\right\};$$

$$K = W\,T\,\frac{2q^2}{h}\left(\frac{k}{q}\right)^2\left(\frac{2kT}{\pi\hbar v_F}\right)\left(\frac{\lambda_0}{L}\right)\times$$
$$\times\Gamma(r+3)\left\{(r+3)\left[\Im_{r+2}(\eta_F)+\Im_{r+2}(-\eta_F)\right]-\frac{(r+2)\left[\Im_{r+1}(\eta_F)-\Im_{r+1}(-\eta_F)\right]^2}{\Im_r(\eta_F)+\Im_r(-\eta_F)}\right\};$$

$$K_0 = W\,T\,\frac{2q^2}{h}\left(\frac{k}{q}\right)^2\left(\frac{2kT}{\pi\hbar v_F}\right)\left(\frac{\lambda_0}{L}\right)\times$$
$$\times\left\{\begin{array}{l}\Gamma(r+4)\left[\Im_{r+2}(\eta_F)+\Im_{r+2}(-\eta_F)\right]-2\eta_F\Gamma(r+3)\left[\Im_{r+1}(\eta_F)+\Im_{r+1}(-\eta_F)\right]+\\ +\eta_F^2\Gamma(r+2)\left[\Im_r(\eta_F)+\Im_r(-\eta_F)\right]\end{array}\right\}.$$

References

1. Yu. A. Kruglyak, *J. Thermoelecticity*, N X, XXX (2014).
2. J. M. Ziman, *Principles of the Theory of Solids* (Cambridge Univercity Press, Cambridge, 1964).
3. C. Kittel, *Introduction to Solid State Physics* (John Wiley and Sons, New York, 1971).
4. N. W. Ashcroft and N.D. Mermin, *Solid State Physics* (Saunders College, Philadelphia, 1976).
5. L. I. Anatychuk, *Thermoelectricity. V. 1. Physics of Thermoelectricity* (Bookrek, Chernivtsi, 2009).
6. C. Jeong, R. Kim, M. Luisier, S. Datta, and M. Lundstrom, *J. Appl. Phys*. **107**, 023707 (2010).
7. M. Lundstrom, *Fundamentals of Carrier Transport* (Cambridge University Press, Cambridge, 2012).
8. C. Jeong, S. Datta, and M. Lundstrom, *J. Appl. Phys*. **109**, 073718 (2011).
9. J. Callaway, *Phys. Rev*. **113**, 1046 (1959).
10. M. G. Holland, *Phys. Rev*. **132**, 2461 (1963).
11. C. Jeong, S. Datta, and M. Lundstrom, *J. Appl. Phys*. **111**, 093708 (2012).
12. C. Gang, *Nanoscale Energy Transport and Conversion: A Parallel Treatment of Electrons, Molecules, Phonons, and Photons* (Oxford University Press, New York, 2005).
13. C. J. Glassbrenner and G.A. Slack, *Phys. Rev. A*, **134**, 1058 (1964).
14. J. B. Pendry, *J. Phys. A*, **16**, 2161 (1983).
15. K. Schwab, E.A. Henriksen, J.M. Worlock, and M.L. Roukes, *Nature*, **404**, 974 (2000).
16. D. E. Angelescu, M.C. Cross, and M.L. Roukes, *Superlatt. Microstruct*. **23**, 673 (1998).
17. L. G. C. Rego, and G. Kirczenow, *Phys. Rev. Lett*. **81**, 232 (1998).
18. M. P. Blencowe, *Phys. Rev. B*, **59**, 4992 (1999).
19. L. G. C. Rego, and G. Kirczenow, *Phys. Rev. B*, **59**, 13080 (1999).
20. I. V. Krive, and E.R. Mucciolo, *Phys. Rev. B*, **60**, 1429 (1999).
21. C. M. Caves, and P.D. Drummond, *Rev. Mod. Phys*. **66**, 481 (1994).
22. R. S. Kim, *Physics and simulation of Nanoscale Electronic and Thermoelectric Devices* (Purdue University, West Lafayette, 2011).

Submitted 21.11.2014

E. I. Rogacheva[1], A. V. Budnik[1], O. S. Vodorez[1], M.V. Dobrotvorskaya[2]

[1]National Technical University "Kharkiv Polytechnic Institute",
21 Frunze St., Kharkiv 61002, Ukraine
[2]Institute for Single Crystals of NAS of Ukraine,
60 Prospect Lenin, Kharkov, 61001, Ukraine

THE EFFECT OF DEVIATION FROM STOICHIOMETRY ON THERMOELECTRIC AND MECHANICAL PROPERTIES OF Bi_2Te_3

For alloys in the Bi-Te system with compositions in the vicinity of Bi_2Te_3 (57.5-70 at.% Te), room temperature dependences of the Seebeck coefficient S, the Hall coefficient R_H, electrical conductivity σ, charge carrier mobility μ, thermoelectric power factor P, and microhardness H on Te concentration were measured. The objects of the study were polycrystalline samples prepared by an ampoule method and subjected to a long-term homogenizing annealing at 670 K. It was found that under the deviation from the stoichiometric composition (60 at.% Te) to the Bi side down to 57.5 at.% Te and to the Te side up to ~ 61 at.% Te, S, R_H, μ decrease, whereas H increases; at ~ 61 at.% Te the inversion of the conductivity type p→n occurs, and at the inversion point the minimum values of σ and μ are observed. In the region corresponding to the electron conductivity, in the vicinity of 63 at.% Te, extrema are observed in the property-composition dependences, and starting from ~ 65 at.% Te, S, R_H and μ remain practically constant, while H increases monotonically. The maximum values of P correspond to the stoichiometric composition (p-type conductivity) and to 65 at.% Te (n-type conductivity). Possible causes of such non-monotonic behavior of the properties under deviation from the stoichiometric composition are discussed.

Key words: bismuth telluride, nonstoichiometry, thermoelectric properties, microhardness

Introduction

Deviation from stoichiometry belongs to one of the basic means of control over the properties of semiconductor compounds. It stimulates a detailed research on thermoelectric (TE) properties of promising TE materials depending on the degree of deviation from stoichiometry.

Bismuth telluride Bi_2Te_3 and solid solutions on its basis are well known TE materials that are widely used in the manufacture of various cooling devices and are most efficient at near-room temperatures [1-4].

Bi and *Te* components have unlimited mutual solubility in liquid state. In solid state, in *Bi-Te* system formation of a series of compounds was found (Bi_2Te_3, Bi_7Te_3, Bi_2Te, $BiTe$, etc.), of which only Bi_2Te_3 is melting congruently at temperature 859 K, and the rest are formed according to peritectic reactions [5, 6]. In the region of compositions between Bi_2Te_3 and Te no intermediate phases were found, and a eutectic-type state diagram takes place (eutectic temperature is 687 K). It is known that close to Bi_2Te_3 compound, maximum on liquidus and solidus curves is displaced from stoichiometric composition towards *Bi* excess, and at congruent melting point it corresponds,

according to different authors, to compositions: 59.935 at.% *Te* [7], 59.95 at.% *Te* [8] and 59.8 at.% *Te* [9]. To determine the boundaries of homogeneity region of Bi_2Te_3 in *Bi-Te* system, different authors measured charge carrier concentration $n(p)$ [10], electric conductivity σ [11], the Seebeck coefficient *S* [10,11], unit cell parameters [9], optical density of vapours [8], as well as the data of differential thermal analysis [9]. Today it is known that Bi_2Te_3 exists in a narrow concentration range, and the data of different authors with respect to the boundaries of homogeneity region of Bi_2Te_3 correlate rather well and correspond to 59.4–60.3 at.% *Te* (773-853 K) [11], 59.8-60.2 at.% *Te* (733-793 K) [8], 59.4-60.2 at.% *Te* (~850 K) [10], 59.7- 60.35 at.% *Te* (673 K) [9], 59.92-60.05 at.% *Te* (773-798 K) [7]. However, as we can see, the data available in the literature refer to sufficiently high temperatures.

Bi_2Te_3 crystallizes as tetradymite-type rhombohedral lattice based on a nine-layer packing of *Bi* and *Te* atoms (space group $R3m$-D^5_{3d}) [2, 3, 12-14] and is characterized by anisotropy of properties. Tetradymite-type rhombohedral lattice can be considered as a hexagonal layered structure where one cell is a successive superposition of three five-layer groups with alternation of layers according to scheme:$-B^1-A-B^2-A-B^1-$, where *A – Bi*, *B – Te*, and indexes 1 and 2 point to the difference in positions of *Te* atoms in crystal lattice. X-ray studies of other phases of *Bi-Te* system [12-14] have shown that all of them crystallize as a hexagonal layered structure consisting of five atomic packings with intercalated additional layers of one sort of atoms perpendicular to the *c* axis and different number and sequence of layers.

Under deviation from stoichiometry, structural defects are formed in crystal lattice. It was established that with stoichiometric composition (60 at.% *Te*) and under deviation from it towards *Bi* excess, *p*-type conductivity is manifested, and towards *Te* excess– *n*-type. In order to explain the abnormal behaviour of charge carriers as compared to that which occurs, for instance, in *PbTe*, T. Harman was the first to suppose [15] that in nonstoichiometric Bi_2Te_3 it is antisite defects that are mostly formed. In [16], for identification of the type of defects the experimentally obtained values of density of bismuth telluride single crystals of various compositions were compared to the results of theoretical calculation on the assumption of various defect formation models. It was shown that under deviation from stoichiometry towards *Bi* excess, formation of antisite defect Bi_{Te} is most possible, and with *Te* excess the experimental values of density were closer to the values calculated on the assumption of vacancy model. However, the authors of [16] indicated the proximity of theoretical calculations disregarding the composition dependence of lattice parameter and using a series of assumptions in the determination of charge carrier concentrations from the electric data. Therefore, it is generally considered that the main type of defects under deviation from stoichiometry both towards *Te* excess and towards *Bi* excess are antisite defects Te_{Bi} and Bi_{Te}, respectively.

In a number of works, the TE properties *S* [11, 10, 2, 17, 18], R_H [10, 2, 17, 18], $n(p)$ [10, 2, 17, 18], electric conductivity σ [11, 17, 18, 2], thermal conductivity λ [10, 17, 18], the Fermi level [18], the Lorentz number [18], TE figure of merit *Z* [2, 17] were studied as a function of

composition in the vicinity of Bi_2Te_3. TE properties were generally measured on single crystal samples. In the majority of works available for characterization of the degree of deviation from stoichiometry in single crystals, it is not the composition of crystals that was employed, but the composition of the melt from which crystals were grown (point on liquidus line) or the temperature of isothermal annealing (these two characteristics are interrelated), or charge carrier concentration in the obtained crystals whose composition does not coincide with the composition of the liquid phase [10, 2, 17, 18]. A direct relation between the composition of crystals and their properties can be established (as it was first done in [10]) by calculation of defect concentration on the basis of $n(p)$ values and lattice parameters, however, in this case one should know exactly the electric effect of this or other stoichiometry defect, its valence state.

The authors of [10] obtained dependences of $n(p)$, S, R_H on the composition of the melt of which Bi_2Te_3 single crystals were grown, and first showed that crystal which is in equilibrium with the liquid of composition 62.8 at.% *Te* has minimum concentration of charge carriers of each type, and its density coincides with the density calculated by parameters of crystal lattice of stoichiometric composition. At higher *Te* concentration in the melt, crystals have *n*-type conductivity, at lower – *p*-type conductivity.

Similar investigations were performed in [2, 17, 18], but the authors used an advanced method of growing single crystals that allowed their quality to be enhanced. They also obtained the dependences of S, R_H, σ, λ, Z on the composition of the melt. According to this data, maximum values of TE figure of merit ($Z = 2.9\ 10^{-3}\ K^{-1}$) were observed for materials with electron conductivity and corresponded to melt composition 64 at.% *Te*.

Analysis of works available on the investigation of properties behaviour in the region of compositions in the vicinity of Bi_2Te_3 in *Bi-Te* system shows that the literature practically lacks information on studying the properties of polycrystals, though for TE applications mostly polycrystalline samples are used. Moreover, as long as solidus line defining ultimate solubility of *Bi* or *Te* in Bi_2Te_3 in solid state is built only for sufficiently high temperatures, and the region of application of Bi_2Te_3 based materials – close to room temperature, it is also desirable to obtain such information for lower temperatures.

The purpose of the present work is to perform a detailed study of the dependences of TE properties and microhardness on *Te* concentration in polycrystalline bismuth telluride exposed to a long-term isothermal annealing in solid state.

Experimental procedure

Synthesis of polycrystals was performed by direct melting of *Bi* and *Te* of high degree of purity (99.999 at. % of the basic component) in evacuated quartz ampoules at (1020 ± 10) K for 5 – 6 hours, annealing at (670 ± 5) K for 300 hours and subsequent cooling to room temperature at the rate of switched off furnace. Altogether, 28 alloys of different composition were prepared in

the range of concentrations 57.5 – 70 at.% *Te*. Some compositions (e.g. 60 at.% *Te*, 59.93 at.% *Te*, 62.8 at.% *Te*) were prepared 2-3 times to be sure in the reproducibility of composition and properties at resynthesis. Comparing the properties of samples of the same composition after resynthesis showed that the difference in the values of characteristics did not exceed their measurement errors.

Microhardness was measured at room temperature on PMT-3 instrument, using a diamond pyramid, at constant load on indentor $P = 0.49$ H. The time of loading, holding under load and the time of load relief made 10 s each. Adjustment of the instrument was performed by means of fresh cleavages of *KCl* crystals. Surface preparation for measurement of *H* (grinding, mechanical polishing and etching) was identical for all the samples. Measurement of *H* of each sample was done at least at 30 sample points with subsequent statistical treatment of the results. The relative mean-square fluctuation did not exceed 3% for all the samples.

The Seebeck coefficient *S* was measured by compensation method with respect to copper electrodes at room temperature at least at 20 sample points with subsequent statistical treatment of measured results. Mean-square relative error for all the samples did not exceed 3 %. The electric conductivity σ and the Hall coefficient R_H were measured by standard *dc* method at an accuracy of ± 5 %. The Hall mobility μ was calculated as $\mu = R_H \cdot \sigma$, and the value of thermoelectric power – by the formula $P = S^2 \cdot \sigma$. Measurements were performed on the samples shaped as parallelepipeds of size 10x2x3 mm, cut out of the obtained ingots.

Results

Figs. 1, *a*-*e* show dependences of *S,* R_H, μ*, H* and *P* on *Te* concentration. It can be seen that these dependences are of sufficiently complicated non-monotonic nature.

S and R_H dependences (Fig. 1, *a*, *b*) are much alike: on both curves at stoichiometric composition (60 at.% *Te*) with hole conductivity there are maxima, under deviation from stoichiometry towards tellurium, *S* and R_H are reduced, and in the vicinity of composition 61 at.% *Te* there is inversion of conductivity type $p \rightarrow n$. Note that position of the inversion point is very close to that determined in [11], where *S* and σ were measured in the vicinity of stoichiometric composition on polycrystalline samples. In the region with *n*-type conductivity, *S* increases to ~ 64 at.% *Te*, following which it practically does not change. The composition dependence of R_H in *n*-region is more complicated: after the inversion point R_H increases, passes through maximum at ~ 63 at.% *Te*, reduces to 65 at.% *Te*, keeping later practically constant value.

On the composition dependence of μ (Fig. 1, *c*) there are two distinct maxima: at stoichiometric composition (60 at.% *Te*) in *p*-region and at composition ~ 63 at.% *Te* in *n*-region.

The concentration dependence of *H* is of unusual nature *H* (Fig. 1, *d*). Under deviation from stoichiometric composition either side (to ~ 59.5 and 61 at.% *Te*), *H* increases, which agrees with generally observed strengthening of crystal lattice on introduction of defects into crystal.

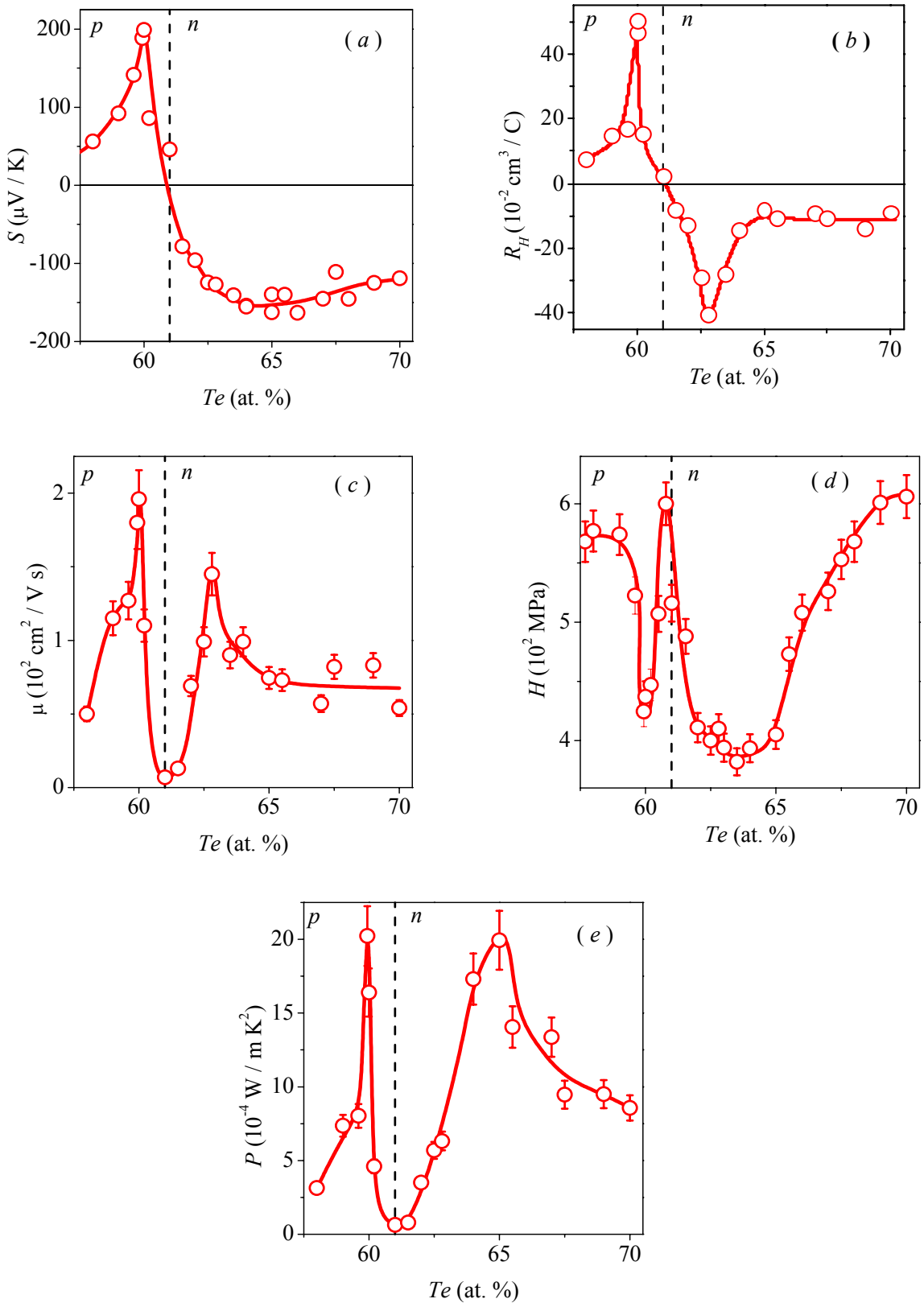

Fig. 1. Dependences of the Seebeck coefficient S (a), the Hall coefficient R_H (b), charge carrier mobility μ (c), microhardness H (d) and thermoelectric power $P = S^2\sigma$ (e) on Te concentration in Bi – Te system with compositions in the vicinity of Bi_2Te_3.

However, at 61 at.% *Te* there is a drastic drop of *H* to the values even lower than at 60 at.% *Te* which continues to ~ 63 at.% *Te*. As a result, the compositions 60 and 63 at.% *Te* are matched by minima of *H*, the inversion point of conductivity sign is matched by maximum of *H*. Then *H* is monotonically increased with growth of *Te* concentration to 70 at.% *Te*. A drastic reduction of *H* observed in the range of compositions 61-63 at.% *Te*, is accompanied by growth of σ, μ, R_H and *S*. Close to 63 at.% *Te* on the dependences of σ, μ, R_H there are maxima, on *H* – composition curve – minimum, and the Seebeck coefficient practically ceases changing. Thermoelectric power shows two maxima on the dependence of *P* on *Te* concentration – at 60 and ~65 at.% *Te*.

Discussion of the results

Deviation from stoichiometric composition of compound results in formation of structural defects, which, in turn, should lead to charge carrier concentration growth (if defects are electrically active), increase in scattering of electrons (holes) and phonons on defects, as well as growth of crystal lattice stresses. Hence, it is not difficult to explain the observed drop in *S*, R_H and μ, as well as growth of *H* under deviation from stoichiometric composition either side. The appearance of electrically active antisite defects of this or other type under deviation from stoichiometry leads to growth of charge carrier concentration, hence, to reduction of *S* and R_H, and increase of defect scattering – to drop of μ. As long as introduction to stoichiometric compound of various defects, including nonstoichiometry defects, leads to lattice strengthening and growth of *H*, increase of *H* under deviation from stoichiometry to ~ 61 and 59.5 at.% *Te* (Fig. 1, *d*) can approximately indicate the boundaries of Bi_2Te_3 homogeneity region. On the side of *Bi* excess, the boundaries of homogeneity region can be determined accurately enough by the position of a bend on the composition dependence of *H*.

The situation is more difficult with determination of the boundary of Bi_2Te_3 homogeneity region on the side of Te excess. In conformity with the state diagram of *Bi-Te*, with *Te* excess with respect to stoichiometric composition and cooling of the melt below eutectic temperature under conditions of thermodynamic equilibrium, the alloys are a two-phase mixture of solid solution based on Bi_2Te_3 and *Te*. It can be assumed that after a long-term isothermal annealing that we performed at 670 K the equilibrium at this temperature is reached. Subsequent cooling at the rate of switched off furnace to room temperature, with regard to low diffusion rate at such low temperatures and low exposure time, will hardly change the situation and one can presumably speak about keeping of equilibrium at 670 K on cooling to room temperature.

As mentioned above, the dimensions of Bi_2Te_3 homogeneity region at elevated temperatures, according to different authors, do not exceed the range of compositions 50.4 - 60.5 at.% *Te*. It was also informed [2, 17] that with lowering of temperature the limit solubility of *Te* is increased. Though we were dealing with high temperatures, it can be assumed that expansion of homogeneity region occurs up to eutectic temperature (687 K), and at 670 K (annealing temperature) close to eutectic temperature, the boundary of homogeneity region on the side of *Te*

excess exceeds 61 at.% *Te*. The fact that a change in conductivity sign takes place at 61 at.% *Te* shows that this composition is within homogeneity region, though close to its boundary, as testified by the observed growth of *H* only to ~ 61 at.% *Te*.

On the other hand, the fact that the inversion point corresponds to 61 at.% Te, rather than to stoichiometric composition, which might be expected with regard to the data obtained in [10, 17] for monocrystalline samples requires explanation. This can be due to several factors. First, displacement of congruent melting point towards *Bi* excess [7-9] leads to the fact that stoichiometric composition already comprises sufficiently high concentration of *p*-type charge carriers as a result of appearance of antisite defect Bi_{Te}. Therefore, under deviation from stoichiometry towards *Te* excess and the emergence of donor type defects (antisite defect Te_{Bi}) a certain number of the latter is needed in order to neutralize the acceptor effect of antisite defects present in stoichiometric Bi_2Te_3, which results in displacement of the inversion point towards *Te*. Moreover, as mentioned above, under deviation from stoichiometry towards *Te* excess, formation of antisite defects Te_{Bi} is most probable, however, according to [9], it is not impossible that *Bi* cation vacancies will be formed that demonstrate an acceptor effect. In this case the inversion point will be further displaced towards tellurium excess.

Assuming that the limit solubility on the side of *Te* is close to 61.0 at.% *Te*, it is not clear why after ~ 61 at.% *Te H* drastically drops, reaching the value which proves to be lower than the value of *H* for stoichiometric Bi_2Te_3 (Fig. 1, *d*). It points to a drastic reduction of crystal lattice distortions, crystal weakening and can testify to the presence of a phase transition. This is also in agreement with mobility growth accompanying a drop in *H* (Fig. 1, *c*).

In some works of the present author with co-authors there were revealed concentration anomalies of various physical properties, including *H* and μ, in the region of low impurity concentrations (0.5–1.0 at.%) that were attributable to critical phenomena attending phase transition of percolation type from dilute to concentrated solid solutions [19].It was suggested that any solid solution has weakening area corresponding to transition to state when interaction of defects covers the entire crystal, leading to qualitative change in the dynamic motion of dislocations, their mobility increase, the macroscopic consequence of which is weakening, i.e. drop in *H*. Obviously, said weakening effect should be particularly significant with the ordered arrangement of defects. In this connection, it may be assumed that in the vicinity of homogeneity region boundary the concentration of defects becomes so considerable that percolation channels are formed connecting deformation fields of separate defects and piercing crystal. Attainment of percolation threshold stimulates self-organization processes in defects subsystem reducing crystal internal energy and leading to formation of a new (in addition to Bi_2Te_3) ordered phase having its own stoichiometry and homogeneity region. Therefore, properties keep changing with composition.

Another reason for a complicated composition dependence of properties can be effects attending second phase precipitations in passing through solidus line. In conformity with *Bi-Te*

diagram of state, on reaching the boundary of homogeneity region there must start *Te* precipitation. *Te* crystal lattice cannot be obtained by simple redistribution of atoms in the sites of Bi_2Te_3 lattice for the distances commensurate with interatomic distances, as in case of ordering, since Bi_2Te_3 and *Te* structures are essentially different. Therefore, second phase precipitation can be preceded by formation of intermediate nonequilibrium structures. In this case, properties can also change in a complicated fashion. Assuming that after 61 at.% *Te* second phase precipitations did start, one can hardly expect in this case a drastic drop in *H*, since at the initial step second phase precipitations are generally fine dispersed, crystal lattice is strengthened and *H* increases, rather than drops.

It can be further supposed that the observed effects are in a certain way related to the impact of kinetic factors. On cooling of alloys from eutectic to room temperatures, in conformity with the equilibrium state diagram the homogeneity region must narrow. On considerably quick cooling of alloys at a rate of switched off furnace from annealing (670 K) to room temperature, because of low diffusion rate of atoms at these temperatures and short exposure time, this process is nor realized completely, but a certain intermediate nonequilibrium state is created whereby crystal is oversaturated with defects. However, on introduction of additional number of excess *Te*, the system jumps into equilibrium (or quasi-equilibrium) state, leading to a drastic reduction of *H* and growth of μ. With further concentration increase of superstoichiometric *Te*, the systems comes to equilibrium state and electrophysical properties cease to change with composition, as it should be in two-phase system. With solid solution decomposition in a quasibinary system in equilibrium state the properties of matrix phase should not change with composition. The growth of *H* in eutectic region 65-70 at.% *Te* is due to the fact that we measure averaged *H* value which increases due to concentration growth of *Te* whose microhardness exceeds *H* of Bi_2Te_3.

Thus, possible reasons for the observed change in TE parameters up to ~ 65 at.% *Te* include: 1) formation of intermediate ordered phase with its own stoichiometry and homogeneity region similar to the way in which it occurs on the side of *Bi* excess; 2) complicated process of the onset of second phase precipitation and possible formation of intermediate nonequilibrium states; 3) impact of kinetic factors – the appearance of nonequilibrium states in which the alloys are found after quick cooling from a long-term annealing to room temperature, and gradual transition to equilibrium with increasing degree of deviation from stoichiometry.

Final identification of the reasons for complicated dependence of TE and mechanical properties of Bi_2Te_3 on the degree of deviation from stoichiometry toward *Te* excess calls for thorough investigation of microstructure and crystal structure depending on the composition and thermal treatment, which will be the subject of our future studies.

Conclusions

The effect of deviation from stoichiometry on thermoelectric and mechanical properties of Bi_2Te_3 semiconductor compound with a change in *Te* content from 57.5 to 70 at.% was studied at

room temperature on polycrystalline samples subject to a long-term homogenizing annealing at 670 K and subsequent cooling at a rate of switched off furnace. A set of experimental studies performed and their analysis allowed making the following conclusions.

After the employed technique of samples preparation the boundaries of homogeneity region are within 59.5 – 61 at.% *Te*. In this region, under deviation from stoichiometric composition (60 at.% *Te*) both toward *Bi* excess and toward *Te* excess there is a drop in *S*, R_H and μ and growth of *H*, which is attributable to introduction to crystal of nonstoichiometry defects increasing charge carrier concentration and the level of stresses in crystal lattice. With increase in *Te* concentration, in the vicinity of 61 at.% *Te* there is inversion of conductivity type $p \rightarrow n$.

A complicated character of properties change with composition beyond the homogeneity region in electron conductivity area is revealed. Close to 63 at.% Te on the composition dependences of properties there are extremes, and starting from ~ 65 at.% *Te*, *S*, R_H and μ practically do not change with composition, and *H* is monotonically increased.

Among possible reasons for the observed complicated nature of properties change beyond the homogeneity region are: 1) formation of intermediate ordered phase with its own stoichiometry and homogeneity region after percolation threshold is reached in defects subsystem; 2) complicated process of the onset of second phase precipitation (*Te*) and possible formation of intermediate nonequilibrium states; 3) impact of kinetic factors – the appearance of metastable states in which the alloys are found after quick cooling from annealing to room temperature, and gradual transition to equilibrium with increasing degree of deviation from stoichiometry.

Maximum values of thermoelectric power *P* correspond to stoichiometric composition and 65 at.% *Te*.

The work was performed with support from the State Foundation for Basic Research (Ukraine) (Grant #UU 42/006-2011) and US Civilian Research and Development Foundation (Grant # UKP-7074-KK-12).

References

1. L.I.Anatychuk, *Thermoelements and Thermoelectric Devices: Reference Book* (Kyiv, Naukova Dumka, 1979).
2. H.Scherrer and S. Scherrer, Bismuth Telluride, Antimony Telluride and their Solid Solution, *CRC Handbook of Thermoelectrics, Edited by D.M. Rowe*, *1995.*
3. B.M.Goltsman, V.A.Kudinov, and I.A.Smirnov, *Semiconducting Thermoelectric Materials Based on Bi_2Te_3* (Moscow: Nauka, 1972) (in Russian).
4. L.E.Bell, Cooling, Heating, Generating Power, and Recovering Waste Heat with Thermoelectric Systems, *Science* **321**, 1457 – 1467 (2008).
5. M.Hansen, K.Anderko, *Structures of Double Alloys, Vol. 2* (Moscow: Metallurgizdat, 1962), p. 256−259.
6. A.E.Vol, *Structure and Properties of Double Metallic Systems, Vol. 2* (Moscow, Gosizdat.Fizmat.Lit., 1962), p. 235−257.

7. G.Offergeld and J.Van Cakenberghe, Determination de la Composition a Fusion Congruente de Semiconducteurs Binaires par Analyse Thermique Differentielle Application a Bi2Te3, Sb2Te3 et Bi2Se3, *J. Phys. Chem. Sol*. **11**, 310-314 (1959).
8. R.F.Brebrick, Homogeneity Ranges and T_{e2}–Pressure along the Three–Phase Curves for $B_{i2}T_{e3}$ and a 55–58 at.% Te, Peritectic Phase, *J. Phys. Chem. Sol*. **30**, 719–731 (1969).
9. A.C.Glatz, An Evaluation of the Bismuth-Tellurium Phase System, *J. Electrochem. Soc*. **112**(12), 1204-1207 (1965).
10. C.B.Satterthwaite and R.W.Ure, Electrical and Thermal Properties of Bi_2Te_3, *Phys. Rev*. **108**, 1164–1170 (1957).
11. N.Kh.Abrikosov, V.F.Bankina, L.V.Poretskaya, E.V.Skudnova, and L.E.Shelimova, *Semiconductor Compounds, Their Preparation and Properties* (Moscow: Nauka, 1967).
12. M.M.Stasova, X-ray Study of Some Bismuth and Antimony Chalcogenides, *J.Structural Chemistry* **5**, 793–794 (1964).
13. M.M.Stasova, O.G.Karpinsky, Number of Layers in the Structures of Bismuth Selenides and Tellurides and Antimony Tellurides, *J.Srtuctural Chemistry* **8**, 85–88 (1967).
14. M.M.Stasova, On the Crystalline Structure of Bismuth Selenides and Antimony and Bismuth Tellurides, *J. Structural Chemistry*, **8**, 655–661 (1967).
15. T.C.Harman, B.Paris, S.E.Miller, and H.L.Goeing, Preparation and Some Physical Properties of Bi_2Te_3, Sb_2Te_3, and As_2Te_3, *J.Phys. Chem. Sol*. **2**, 181-190 (1957).
16. G.R.Mille, Li Che-Yu, Evidence for the Existence of Antistructure Defects in Bismuth Telluride by Density Measurements, *J. Phys. Chem. Sol*. **26**, 173–177 (1965).
17. J.P.Fleurial, L.Gailliard, R.Triboulet, H.Scherrer, and S.Scherrer, Thermal Properties of High Quality Single Crystals of Bismuth Telluride – Part 1: Experimental Characterization, *J. Phys. Chem. Sol*. **49**, 1237-1247 (1988).
18. J.P.Fleurial, L.Gailliard, R.Triboulet, H.Scherrer, and S.Scherrer, Thermal Properties of High Quality Single Crystals of Bismuth Telluride – Part 2: Mixed – Scattering Model, *J. Phys. Chem. Solids* **49**, 1249-1257 (1988).
19. E.I.Rogacheva, Percolation Effects and Thermoelectric Materials Science, *J. Thermoelectricity* **2**, 61-72 (2007).

Submitted 17.12.2015

S. I. Menshikova[1], E. I. Rogacheva[1], A. Yu. Sipatov[1],
P. V. Mateichenko[2], M.V. Dobrotvorskaya[2]

[1]National Technical University "Kharkov Polytechnic Institute", 21 Frunze St., Kharkiv 61002, Ukraine
[2] Institute for Single Crystals, NAS of Ukraine, 60 Lenin ave., Kharkiv, 61001, Ukraine

DEPENDENCES OF THERMOELECTRIC PROPERTIES ON THE THICKNESS OF THIN FILMS OF INDIUM DOPED LEAD TELLURIDE

Dependences of thermoelectric properties (the Seebeck coefficient S, the electric conductivity σ, the Hall coefficient R_H, the carrier mobility μ and the thermoelectric power $P = S^2 \cdot \sigma$) on the thickness d (d = 10 – 255 nm) of thin films prepared by vacuum evaporation of indium-doped PbTe crystals and subsequent condensation on (111) BaF_2 substrates were obtained. With decreasing thickness of films to d ≈ 40 nm, there is n- to p-type inversion of conduction which is related to a change in thermodynamic equilibrium conditions and partial re-evaporation of lead and/or indium atoms. Extremes were found on the thickness dependences of properties at d_1 ≈ 20 nm which is indicative of hole gas quantization. In the range of thicknesses with n-type conduction there is a smooth change in thermoelectric properties with thickness which testifies to manifestation of classical size effect and is sufficiently well described in the framework of the Fuchs-Sondheimer theory.
Key words: lead telluride, thin film, thickness, size effect.

Introduction

The advancement of nanophysics and nanotechnologies calls attention to the development of methods for preparation of low-dimensional structures with the assigned characteristics and to the investigation of their properties. It is known that in low-dimensional state, for instance, in thin films, one can observe size effects. Classical size effect is due to diffusion carrier scattering on film interfaces and is manifested in the case when film thickness *d* is comparable to mean free path length of charge carriers. Quantum size effect results from quantization of carrier energy spectrum and is observed when *d* value becomes comparable to de Broglie wavelength λ_F [1]. When using thin films for practical purposes, account must be taken of the size effects that can result in fundamental changes of material properties.

IV-VI-class semiconductors refer to materials that are widely used in thermoelectricity [2, 3]. Lead telluride has recommended itself as the most efficient material for thermal generators working in the range of medium temperatures (from room temperature to $870 \div 920$ K) [4]. Doping is known to change over a wide range the thermoelectric (TE) properties of material (conduction type, carrier concentration and mobility, etc). As the donor dopants for *PbTe*, use is made of iodine, chlorine, indium and bismuth impurities [5]. It was established [5] that

introduction of indium into *PbTe* crystal lattice yields uniform-carrier concentration crystals with stable properties and low sensitivity to the influence of uncontrolled defects and impurities. Such properties of indium-doped *PbTe*, attractive from a practical point of view, are generally attributable to the existence of a quasi-local impurity level located above the bottom of conduction band and stabilization of the Fermi level at that level [5]. It was shown [6] that introduction of a considerable amount of InTe impurity (up to ~ 6 mol.%) into *PbTe* does not lead to changes in the law of carrier dispersion in conduction band, and that on doping of *PbTe* with In impurity up to ~ 2 at.%, the shape and orientation of the Fermi surface, as well as the value of carrier effective mass remain the same as in the undoped *PbTe* [7].

It was shown [8-13] that in lead chalcogenide films grown by vacuum evaporation of crystals with subsequent condensation on (001) *KCl* substrates there is an oscillating behavior of the kinetic properties with film thickness, attributable by the authors to quantum size effects. In *PbSe* films, there was increase in the electric conductivity and carrier mobility with film thickness, which testified to manifestation of classical size effects [12, 14], and when studying *PbSe* films doped with chlorine the authors of [15] came to conclusion on the overlapping of classical and quantum size effects.

To study size effects, it is important to use structurally perfect films. Small difference in lattice periods and close values of dilatation coefficients of *PbTe* and BaF_2 make (111) BaF_2 cleavages most suitable substrates for preparation of structurally perfect *PbTe* films [16]. As far as we know, size effects in *PbTe* thin films doped with indium donor impurity and grown on (111) BaF_2 substrates have not been investigated by studying transport phenomena.

The purpose of this work is to establish the influence of thickness d of films grown by vacuum evaporation of *PbTe* crystals doped with indium and deposited on (111) BaF_2 cleavages on their thermoelectric properties.

Experimental procedure

The films were prepared by vacuum evaporation (~10^{-5}-10^{-6} Pa) of *PbTe* crystals doped with 1 mol. % *InTe* with subsequent deposition on fresh (111) BaF_2 cleavages maintained at a temperature of (600 ± 10) K. Film thicknesses varied within d = 10 – 255 nm. On top of the films, a protective layer of BaF_2 was deposited by an electron-beam method to protect the film from oxidation and mechanical damages. Film thickness was measured by means of a precalibrated quartz resonator. The Seebeck coefficient S was measured by compensation method with respect to copper in the film plane with an error not exceeding ± 3 %. The electric conductivity σ and the Hall coefficient R_H were measured by standard *dc* method to an accuracy of ± 5 %. The Hall mobility μ_H was calculated as $\mu_H = R_H \cdot \sigma$, the TE power value – by formula $P = S^2 \cdot \sigma$. The measurements were performed on as-prepared samples. In the measurements, crystal was shaped as a parallelepiped of size 10x2x3 mm, and the films of thickness d had the form of a double Hall cross.

The surface morphology and chemical composition of the resulting films was controlled by

electron-probe microanalysis using a scanning electron microscope JSM-6390 LV (Jeol, Japan) with a system of energy-dispersive spectrometer X-Max^n 50 (Oxford Inst., Great Britain) at accelerating voltage 10 kV.

Results

The results of S and R_H measurement have shown that crystal of which the films were prepared was of n-conduction type and had electron concentration n = 3.0 10^{18} cm^{-3}. The low value of n with a considerable content of indium impurity, as mentioned above, is attributable to the Fermi level stabilization on a quasi-local donor level [5].

Studies by electron-probe microanalysis method in the mode of scanning along the film surface and in the mode of probing by the surface points have shown that *PbTe<InTe>* films possess high degree of homogeneity on a microlevel, i.e. the distribution of (*Pb*, *Te*, *In*) elements in the film from one analyzed part to another does not vary within the accuracy of the method. Study on the surface of the films in the mode of secondary electrons (resolution 10 nm) has shown that grain structure in the films is not apparent, the surface is uniform and defects (agglomerates, pores, cracks, etc.) are not observed on the surface. Thus, high homogeneity degree and low sensitivity to the presence of defects are typical not only of the bulk *PbTe<InTe>* crystals [5], but also of the films.

Dependences of S, R_H, σ, μ_H, as well as P on the thickness of *PbTe* layer at room temperature are given in Fig. 1, where the values of crystal kinetic coefficients are marked by black squares, those of thin films – by white circles.

Measurements of S and R_H have shown that with increasing the thickness of films, there is n- to p-type inversion at $d \approx 40$ nm (dashed line in Fig. 1 corresponds to the boundary between the areas with p-and n-type conduction). Possible reason for the appearance of p-type conduction can be a change in thermodynamic equilibrium conditions in the thin-film state as compared to crystal. One should also take into account the possibility of partial reevaporation of indium or lead atoms at condensation on the substrates.

Note that in *PbTe* films under study with thicknesses $d \approx$ 100-255 nm the values of S and R_H practically coincide with S and R_H of polycrystal. At the same time, the electric conductivity and carrier mobility in the films are almost three times higher than σ and μ_H of the initial charge (Fig. 1), which indicates to a higher degree of structural perfection of films as compared to crystal. As a result, in the film state one can reach the value of thermoelectric power $P = S^2 \cdot \sigma = 16.5 \cdot 10^{-4}$ W/K^{2}m which is more than three times as large as the P of the initial crystal.

As is evident from Fig. 1, for films with p-type conduction for $d_1 = (20 \pm 2)$ nm on the thickness dependences of S and R_H there are maxima that correspond to minima on the dependences $\sigma(d)$, $\mu_H(d)$ and $P(d)$. In the area with n-type conduction (d > 40 nm) there are also extremes on the d-dependences of the kinetic coefficients at $d = (50 \pm 4)$ nm. With larger

thicknesses ($d > 50$ nm) TE properties change monotonically with film thickness, namely S, σ, μ_H, P and smoothly increased, and R_H is decreased.

Note that in [12], like in the present work, extremes were observed on d-dependences of TE properties of *PbSe* films in *p*-type conduction area at $d = 10$ nm, which was attributable by the authors to manifestation of quantum size effect for carrier hole gas and explained by intersection of the first hole subband of the Fermi level. In the present paper, the observed extreme in the area of *p*-type conduction films can be also related to size quantization of carrier energy spectrum. If a layer of *PbTe<InTe>* is represented as a rectangular potential well with infinitely high walls arranged between isolating BaF_2 layers, one of which is a single-crystal substrate, and the other – protective coating, in such a well carrier motion is limited, which leads to quasi-pulse quantization and formation of transverse energy subbands. The number of carrier-filled subbands N varies stepwise, and when film thickness is increased by the value equal to half de Broglie wavelength, a new subband intersects the Fermi level and contributes to conduction. The thickness whereby the first subband ($N = 1$) intersects the Fermi level can be written as [12]:

$$d_1 = \frac{h}{\sqrt{8m_{\perp}^{*}\varepsilon_F}}, \qquad (1)$$

where h is the Planck constant, $m_{\perp}^{*}$ is effective mass along the direction perpendicular to quantum well, ε_F is the Fermi energy. The period of quantum oscillations Δd is also determined by formula (1) [17], i.e. it completely coincides with the value of d_1. In a number of works it was shown (see, for instance [12, 13, 17]) that for precise determination of quantum oscillation period it is sufficient to fix the first extreme on the film thickness dependences of the kinetic properties.

Let us determine thickness d_1 in *PbTe* films under study. In the calculation, we shall use the value of ε_F found by the average hole concentration in the films with hole conduction $p = 2.7 \cdot 10^{18}$ cm^{-3} with regard to the transverse and longitudinal components of effective mass $m_{\perp}^{*} = 0.022\ m_0$, $m_{\parallel}^{*} = 0.31\ m_0$ [18]. Calculation by formula (1) yielded the value of $d_1 = (21 \pm 2)$ nm, which is in good agreement with the position of the first extreme in the region with *p*-type conduction ($d_1 = 20 \pm 2$ nm) (Fig. 1).

A similar calculation of oscillation period was performed for *n*-type films, i.e. in the area with $d > 40$ nm. As the input parameters, use was made of the values of effective masses $m_{\perp}^{*} = 0.024\ m_0$, $m_{\parallel}^{*} = 0.24\ m_0$ [18] for electrons in *PbTe* and the value of ε_F calculated by the Hall coefficient values in the thick films. As a result of calculation, the value of oscillation period was $\Delta d = (20 \pm 2)$ nm.

It can be supposed that the extremes observed at $d \approx 50$ nm on the dependences $S(d)$, $R_H(d)$, $\sigma(d)$, $\mu_H(d)$ and $P(d)$ correspond to intersection of the Fermi level by the energy subband.

Smooth variation of the kinetic coefficients with thickness for films with $d > 50$ nm can be related to manifestation of classical size effect. Due to the fact that the electron gas in films under study was degenerate, an attempt was made to describe the thickness dependences of transport properties using the Fuchs-Sondheimer theory for metals [19]. The theory is concerned with a

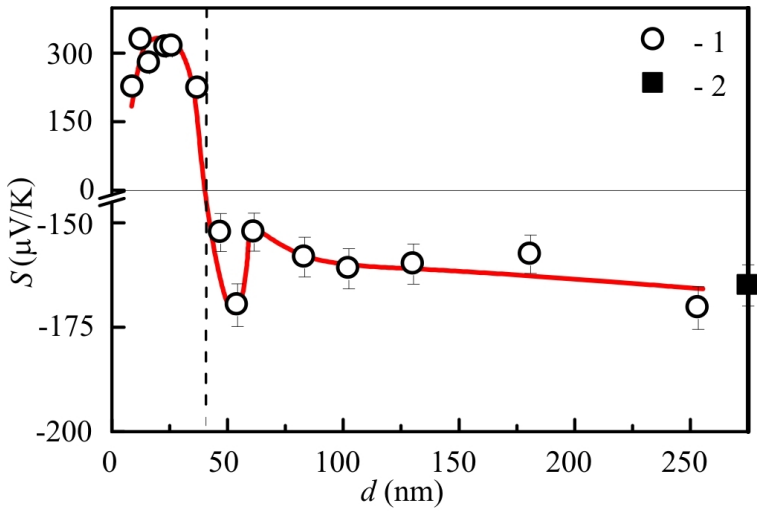
300
150
0
-150
-175
-200
S (μV/K)
0
50
100
150
200
250
d (nm)
- 1
- 2

a)

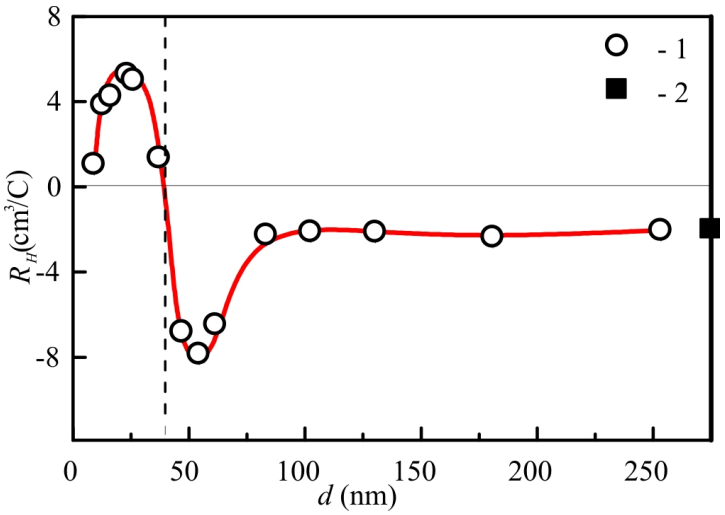
8
4
0
-4
-8
R_H(cm³/C)
0
50
100
150
200
250
d (nm)
- 1
- 2

b)

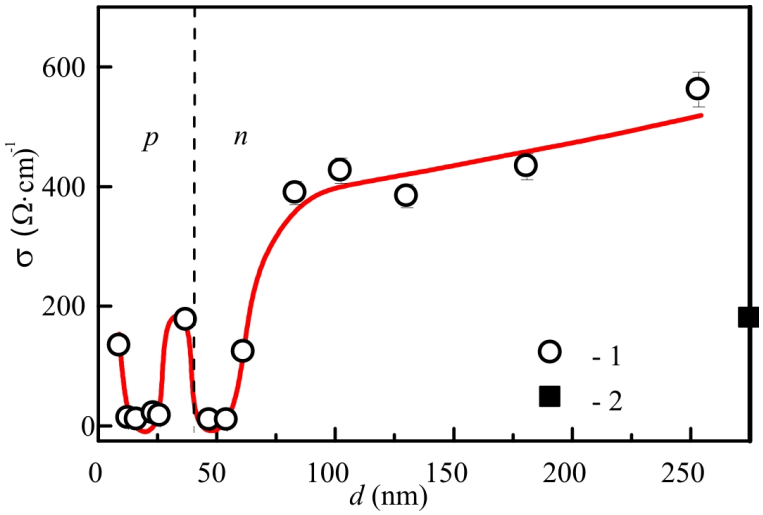
600
400
200
0
σ (Ω·cm)⁻¹
p
n
0
50
100
150
200
250
d (nm)
- 1
- 2

c)

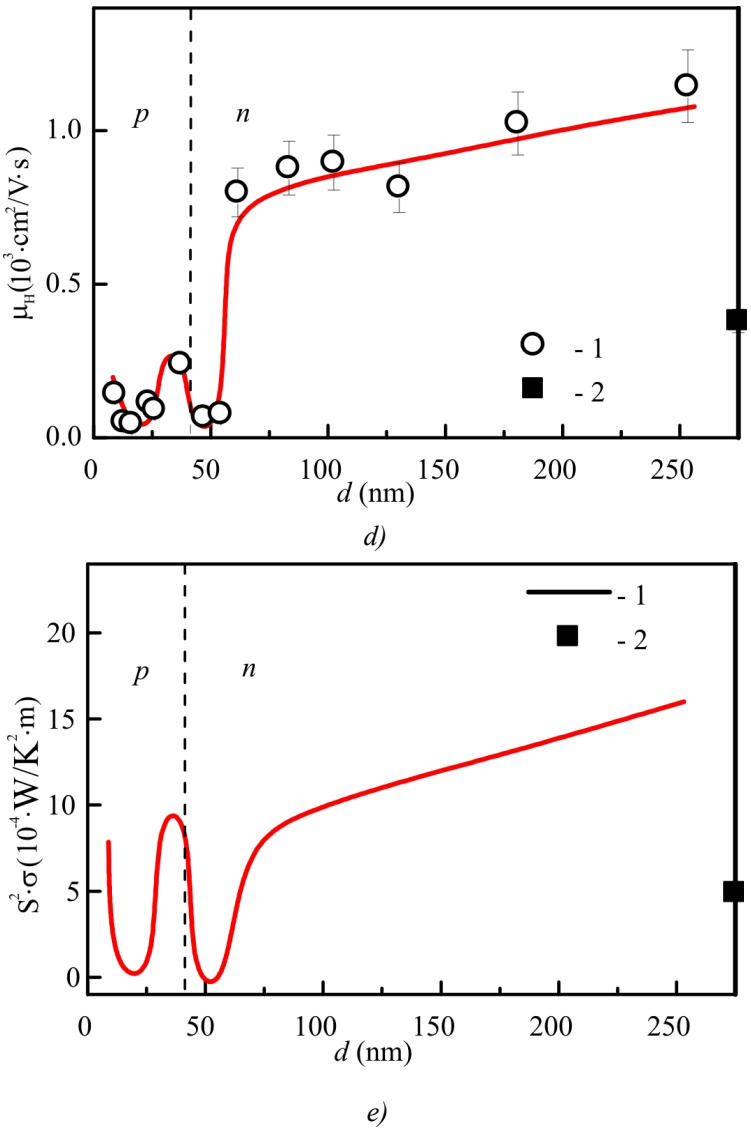

Fig. 1. Dependences of the Seebeck coefficient S (a), the Hall coefficient R_H (b), the electric conductivity σ (c), the Hall carrier mobility μ_H (d) and the thermoelectric power $P = S^2 \cdot \sigma$ (e) on the thickness of PbTe<InTe> films in the structure (111)BaF_2/PbTe<InTe>/BaF_2: 1 – PbTe<InTe> films; 2 – PbTe<InTe> crystal.

metal having a spherical Fermi surface and isotropic carrier mean free path *l*.

A specularity parameter *p* is introduced which characterizes the share of carriers elastically reflected from the film interfaces. The value of *p* can lie in the range from 1 (fully specular reflection) to 0 (fully diffuse reflection). With a fully specular reflection, classical size effect will be not apparent. In the theory it is assumed that *l* and *p* do not depend on the thickness, and *p* is a constant which is equal for both surfaces and does not depend on the trajectory and the angle of carrier incidence on the surface.

If the films are not too thin ($d \sim l$), then according to the Fuchs-Sondheimer theory, the expression for electric conductivity of metal plate of thickness *d* can be written as follows [19, 20]:

$$\sigma_d = \frac{\sigma_\infty}{1+\frac{3}{8}(1-p)\frac{l}{d}}, \quad (2)$$

where σ_∞ is the value of electric conductivity for a sample with infinitely large thickness.

Based on the Fuchs-Sondheimer theory, Mayer [21] obtained the expression for the Seebeck coefficient S of metallic plate as a function of its thickness. In the approximation of not very thin films ($d \sim l$), S is written as [21]:

$$S = S_\infty\left(1-\frac{3}{8}(1-p)\frac{l}{d}\frac{U}{1+U}\right), \quad (3)$$

where S_∞ is the S value of a film with infinitely large thickness, parameter $U = \left(\partial \ln l \big/ \partial \ln E\right)_{E=\varepsilon_F}$ characterizes the energy dependence of mean free path, and with a quadratic dispersion law $U = 2$ [22].

In the framework of the Fuchs-Sondheimer theory, subject to condition $d \sim l$, the Hall coefficient is practically unvaried with thickness ($R_H = R_{H\infty}$, where $R_{H\infty}$ is the Hall coefficient of a film with infinitely large thickness) [22]. With regard to the fact that carrier mobility is a product of σ and R_H, dependence of μ on d, provided $d \sim l$, is determined by dependence $\sigma(d)$, i.e. it can be written as:

$$\mu_d = \frac{\mu_\infty}{1+\frac{3}{8}(1-p)\frac{l}{d}}, \quad (4)$$

where μ_∞ is the mobility of a film with infinitely large thickness.

With the aid of software package MatLAB 6.5, by varying the values of p and l, conditions were determined (the values of l and p), whereby there is the best fit of theoretical curves $\sigma(d)$, $S(d)$ and $\mu_H(d)$ to the respective experimental data. As a criterion of the best coincidence between the calculated and experimental curves, a root-mean-square deviation ε was chosen. Calculation was made for the films with thicknesses $d > 55$ nm, where one can observe gradual increase of the electric conductivity, the Seebeck coefficient and the mobility with thickness. Fig. 2 shows the results of theoretical calculation of dependences $\sigma(d)$, $S(d)$ and $\mu_H(d)$ in the framework of the Fuchs-Sondheimer theory (continuous line) and experimental data (white circles).

It is seen that the experimental dependences $\sigma(d)$, $S(d)$ and $\mu_H(d)$ can be fairly well described in the framework of the Fuchs-Sondheimer theory, considering the case of not very thin films. As the input parameters, the values of σ_∞ = 565 (Ohm · cm)$^{-1}$, μ_∞ = 1150 cm^2/V·s and S_∞ = -170 μV/K were used corresponding to the kinetic coefficients of the thickest film under study. The lowest value of ε in the calculation of dependences $\sigma(d)$, $S(d)$ and $\mu_H(d)$ was achieved with specularity parameters p = 0.64, 0.87 and 0.75 and the electron mean free path lengths l = 470 nm, 400 nm and 410 nm, respectively. The spread in the values of p can be due to a small number of experimental points and/or considerable number of simplifications

used in the calculation. Nevertheless, averaging of specularity parameter values determined from the dependences $\sigma(d)$, $S(d)$ and $\mu_H(d)$ yields rather high value of $< p > = 0.75$ which points to preferably specular reflection of electrons from the film interfaces.

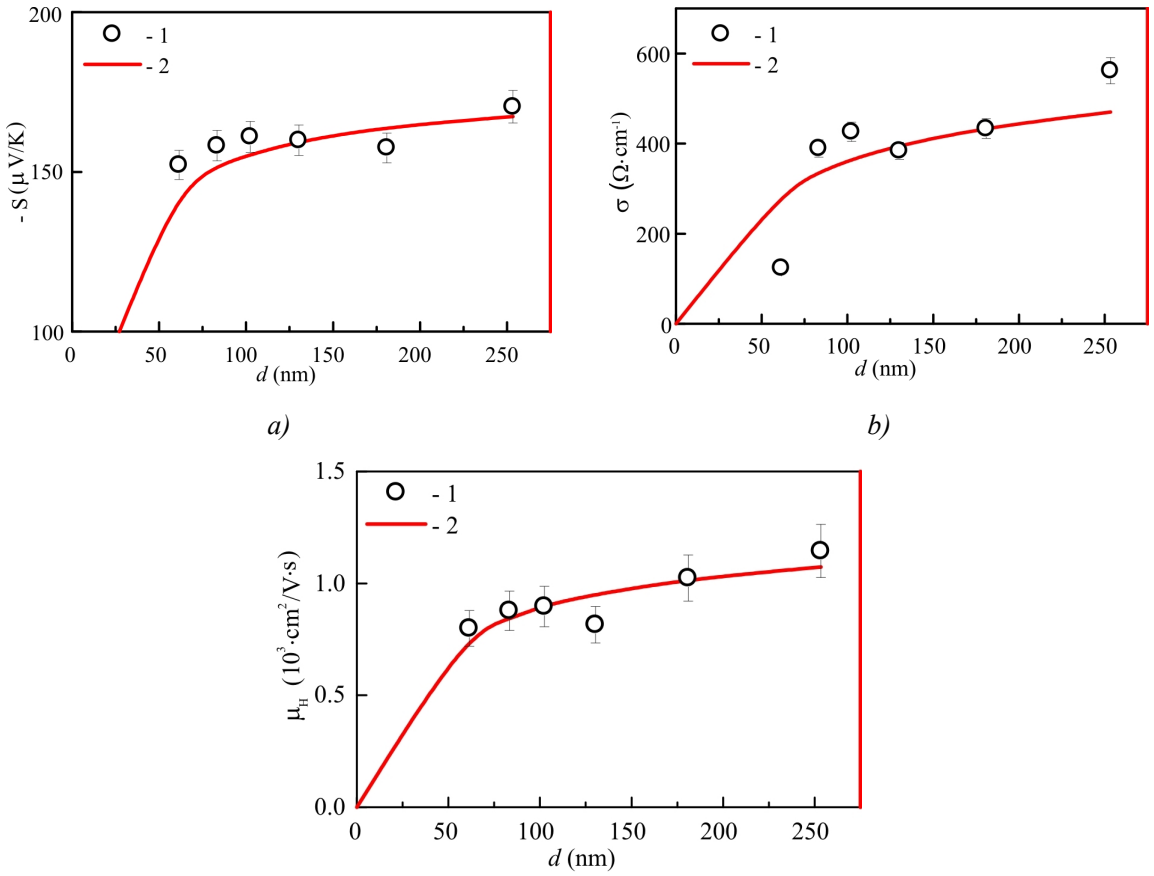

Fig. 2. The Seebeck coefficient S (a), the electric conductivity σ (b) and the electron mobility μ_H (c) in the structure (111)BaF_2/PbTe<InTe>/BaF_2: 1 – PbTe<InTe> films; 2 – theoretical calculation in the framework of the Fuchs-Sondheimer theory.

In [12], for *PbSe* films in the calculation of $\sigma(d)$ dependence in the framework of the Fuchs-Sondheimer theory the value of $p = 0.57$ was obtained that proved to be lower than in the present work. The difference in p values for lead chalcogenide films grown on different substrates (*KCl* and BaF_2) is attributable to different location of atoms (lead and chalcogen) in crystallographic planes (001) and (111). As long as lead chalcogenides have the structure of *NaCl* type [18], with the growth of film in [001] orientation on *KCl* substrates [12], on the interfaces in (001) plane the atoms of components (lead and chalcogen) are arranged in staggered rows, and with the growth of film in [111] orientation, i.e. on BaF_2 substrates, like in this paper, (111) plane consists of one sort of atoms (either lead atoms or chalcogen atoms only). Obviously, several sorts of atoms available on (001) surface result in a more considerable diffuse scattering than in the films with [111] orientation, where only one sort of atoms contributes to scattering.

Conclusions

1. Vacuum evaporation of *PbTe* crystals doped with 1 mol. % InTe with subsequent condensation on (111) BaF_2 substrates was used to obtain films of thickness d = 10-255 nm.
2. With decreasing film thickness to $d \approx 40$ nm, there is $n \rightarrow p$ type inversion of conduction. It is supposed that the effect observed can be due to a change in thermodynamic equilibrium conditions in the thin film as compared to the bulk crystal and due to partial reevaporation of indium and/or lead atoms.
3. The films possess high degree of homogeneity, and the grain structure in the films is not manifested, which is of interest from practical standpoint.
4. The dependences of the electric conductivity σ, the Hall mobility μ_H, the Hall coefficient R_H, the Seebeck coefficient S and the thermoelectric power $P = S^2 \cdot \sigma$ on the thickness of films are of nonmonotonic nature. In the range of thicknesses of p-type films there are extremes on the thickness dependences of all properties at $d_1 = (20 \pm 2)$ nm that are attributable to quantum size effect.
5. The increase in S, σ and μ_H with film thickness in the range with n-type conduction indicates the manifestation of classical size effect. Theoretical calculation of the dependences $\sigma(d)$, $S(d)$ and $\mu_H(d)$ in the framework of the Fuchs-Sondheimer and Mayer theories is in rather good agreement with the experimental data.

The work was supported by the Ukrainian Foundation for Basic Research (grant № UU 42/006-2011) and by the U.S. Civilian Research and Development Foundation (grant № UKP2-7074-KK-12).

References

1. Komnik Yu. F. Physics of Metal Films // Moscow: Atomizdat, 1979. 264 p.
2. Anatychuk L. I. Thermoelements and Thermoelectric Arrangements. // Reference book, Kiev, Naukova dumka, (in Russian), 1979, 768 p.
3. Rowe D. M. CRC Handbook of Thermoelectrics. // CRC Press, Boca Raton, London, New York, Washington, 1995.
4. Sorrell C. C., Sugihara S., Nowotny J. // Materials for energy conversion devices, Woodhead Pub. Limited. – 2005. – 416 p.
5. Kaidanov V. I., Ravich Yu.I. Deep and resonance states in A^{IV} B^{VI} semiconductors. // Usp. Fiz. Nauk, 145, 1, in Russian. – 1985. – P. 51-86.
6. Averkin A. A., Kaidanov V. I., Melnik R. B. // On the nature of the impurity states of indium in lead telluride // Fiz. Tekh. Poluprov. – 1971. – № 5. – P. 91-95.
7. Lykov S. N., Chernick I. A. // Oscillation effects of the Shubnikov-de Haas in lead telluride doped with indium, Sov. Phys. Semicond. – 1980. – № 14. – P. 47-54.
8. Rogacheva E. I., Nashchekina O. N., Tavrina T. V., Us M., Deepselh and M. S., Cresonance., Rabin O. Quantum stateseffects in IV-VI quantum wells. // Physica E. – 2003. – № 17. – P. 313-315.

9. Rogacheva E. I., Nashchekina O. N., Vekhov Y. O., Dresselhaus M. S., Cronin S. B. // Effect of thickness on the thermoelectric properties of *PbS* thin films, Thin Solid Films. – 20024 № 23. – P. 115-118.
10. Rogacheva E. I., Vodorez O. S., Nashchekina O. N., Sipatov A. Yu., Fedorov A. G., Olkhovskaya S. I., Dresselhaus M. S. Oscillatory Behavior of Thermoelectric Properties in p-Pbte Quantum Wells. // J. Electronic Materials. // 2010. – № 39(9). – P. 2085-2091.
11. Rogacheva E. I., Tavrina T. V., Nashchekina O. N., Grigorov S. N., Nasedkin K. A., Dresselhaus M. S., Cronin S. B. Quantum size effects in *PbSe* quantum wells. // Appl. Phys. Lett. – 2002 80. – P. 2690-2693.
12. Rogacheva E. I., Nashchekina O. N., Olkhovskaya S. I., and Dresselhaus M. S. Size Effects in *PbSe* Thin Films. – J. Thermoelectricity. – 2012. – № 4. – P. 25-32.
13. Olkhovskaya S.I., Rogacheva E.I.. Size effects in lead telluride thin films and thermoelectric properties. // Thermoelectricity. – 2013. – № 5. – P. 22-27.
14. Rogacheva E. I., Ol'khovskaya S. I., Sipatov A. Yu., Fedorov A. G. Size effect in lead selenide thin films // Bulletin of Kharkov National University, Ser. Physics. – 2010. – 914 (13). – P. 115-118.
15. Ol'khovskaya S. I., Rogacheva E. I., Sipatov A. Yu. Thickness Dependences of *PbSe<Cl>* Films Thermoelectric Properties. // Metallofizika I Noveishie Tekhnologii. – 2011. – № 33. – P. 213-220.
16. Springholz G., Molecular Beam Epitaxy of IV-VI Heterostructures and Superlattices in: Lead Chalcogenides: Physics and Applications, ed. D. Khokhlov, Taylor and Francis, 2003.
17. Rogacheva E. I., Dresselhaus M. S. Quantum size effects and thermoelectric transport in IV – VI based 2*D*-structures. // Proc. ECT, Odessa, Ukraine. – 2007. – P. 29-34.
18. Ravich Yu. I., Efimova B. A., Smirnov I. A., Methods of research on semiconductors as applied to lead chalcogenides *PbTe, Pbse* and *PbS*, Moscow, Nauka, 1968.
19. Fuchs K. The conductivity of thin metallic films according to the electron theory of metals // Proc. Cambridge Philos. Soc. – 1938. – № 34. – P. 100-108.
20. Sondheimer E. H. The mean free path of electrons in metals // Adv. Phys. – 1952. – № 1. – P. 1-42.
21. Mayer H. Physik dunner Schichten, V. 2, Wissenschaftliche Verlag, Stuttgart, 1955.
22. Stasyuk Z.V., Lopatinsky A.I. size-dependent kinetic phenomena in thin metal films. Classic Effects (review). // Physics and Chemistry of Solid State. – 2001. – № 4. – P. 521-542.

Submitted 23.11.2014

Yu. M. Lobunets

Yu. M. Lobunets

Institute of Thermoelectricity NAS and MES of Ukraine
1, Nauky Str., Chernivtsi, 58029, Ukraine

HEAT EXCHANGE-TYPE TEG FOR MARINE PROPULSION PLANTS. Part II.

The characteristics of heat exchange-type thermoelectric generators using the heat of marine engine cooling system are analyzed. The prospects of using such TEG are outlined.
Key words*:* thermoelectric generator, low-grade heat source, marine propulsion plants

Introduction

In [1], the scheme of heat exchange-type thermoelectric generator (TEG) utilizing the exhaust gas heat of marine diesel engines was analyzed. It was shown that technical and economic features of the above scheme permit to expect wide application of similar TEG on water transport. At the same time, in this scheme there is another source of secondary energy, namely the heat of engine cooling system which accounts for 10 to 15% of fuel consumption. Despite the relatively low temperature potential, the use of this source can be no less attractive due to the simplicity of application scheme – actually it requires only substitution of standard heat exchanger by thermoelectric generator which performs the functions of heat exchanger and simultaneously generates additional electric power. Below are discussed the peculiarities of such TEG, and the estimates of its technical and economic features are given.

Scheme of heat exchange-type TEG for diesel propulsion plant cooling system

In the general case, marine diesel plant cooling system (Fig.1) comprises two heat carrier circuits with cooling liquid circulating in one of them (fresh water or antifreeze) and sea water circulating in the other. Optimal temperature of cooling liquid is 90...100°C; the temperature of sea water varies within 5 to 30°C. The difference in heat carrier temperature at the inlet and outlet

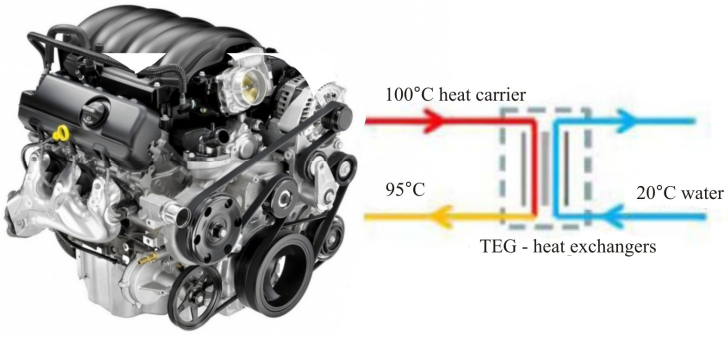

Fig. 1. Schematic of TEG for a marine plant.

of cooling system must not exceed 5 to 10°C. Heat carrier consumption in the circuits is determined by propulsion plant power and heat exchanger efficiency. The most efficient cooling systems employ plate heat exchangers [2].

The scheme of heat exchange-type TEG is similar to that of a plate heat exchanger where thermopiles are installed instead of plates [3]. The thermopiles are comprised of thermoelectric modules arranged between two metal plates with four openings that form collectors for heat carriers. The thermopiles are divided by elastic spacers forming channels for passage of heat carriers and tightening the entire structure which is clamped between two end plates, *Fig.2*.

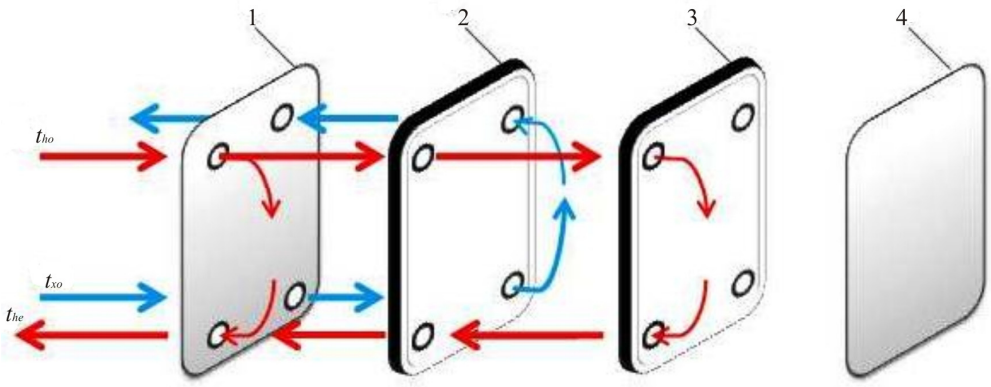

Fig. 2. Schematic of heat-exchange type TEG 1, 4 – end plates (TEG housing), 2, 3 – thermopiles.

The main function of heat exchange-type TEG in the scheme under study is to provide heat carrier cooling to given temperature. At the same time, it is necessary to optimize TEG parameters with a view to obtain maximum electric power.

The original parameters of the problem are:

Q_o – heat exchanger thermal power (in the calculations below it is assumed that Q_o = 10 kW);

t_{ho} = 100°C – TEG inlet heat carrier temperature;

t_{he} = 95°C – TEG outlet heat carrier temperature;

t_{xo} = 30°C - sea water temperature.

Mathematical model of TEG

Design model of TEG is represented in Fig.3.

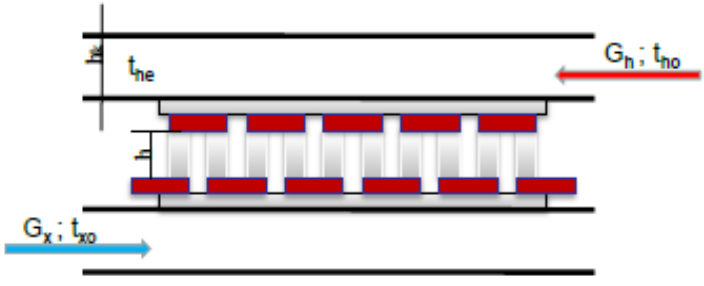

Fig.3. Design model of TEG.

In the general case, the mathematical model of TEG is composed of a system of equations that permit to determine temperature distribution in heat carriers and thermoelements [4]:

- equation for temperature distribution in thermoelements for boundary conditions of the third kind:

$$\Theta(Y) = C_1 + C_2 Y - \frac{J^2}{2I_0} Y^2, \tag{1}$$

where integration constants C_1, C_2 are determined as:

$$C_1(J + Bi_x) - C_2 = Bi_x \vartheta_x, \tag{2}$$

$$C_1(Bi_h - J) + C_2(Bi_h - J + 1) = Bi_h \vartheta_h + \frac{J^2}{I_0}(1 + 0.5Bi_h - J), \tag{3}$$

- equation for determination of heat exchange coefficients:

$$Nu = 0.022 Re^{0.8} Pr^{0.43} \tag{4}$$

- equation for determination of temperature distribution of heat carriers along the channel:

$$\frac{dvh}{dX} = \frac{dKih}{Wh}; \tag{5}$$

$$\frac{dvh}{dX} = \frac{dKix}{Wx};$$

$$Ki_h = Bi_h(\vartheta_h - \Theta_h); \tag{6}$$

$$Ki_x = Bi_x(\Theta_x - \vartheta_x).$$

In the above equations, criterion *Bi* is the ratio of thermoelectric material thermal resistance to the sum of thermal resistances on the way of heat flux from thermoelement surface to heat carrier, i.e.

$$Bi = R_O / R_t, \tag{7}$$

Where $R_t = \frac{1}{\alpha} + \sum_i \frac{hi}{\lambda i}$, *hi* and λi is the thickness and thermal conductivity coefficient of each layer on the way of heat flux (connecting elements, heat spreader, thermopile housing, solder interlayers, etc).

As long as the system of equations (1– 7) is nonlinear, it will be solved by numerical methods.

Analysis results

Formulation of the problem in hand stringently specifies heat carrier parameters in the first

circuit and, accordingly, determines its overall consumption:

$$G_o = Q_o / \left[Cp\left(t_{ho} - t_{he}\right) \right]. \tag{8}$$

The purpose of calculations is to determine the total area of TEG that meets the reference conditions of the problem. As long as TEG is composed of identical thermopiles, at the first stage it is necessary to determine conditions, whereby given temperature condition of heat carrier in cooling system is assured within one thermopile. That is, for given thermopile structure it is necessary to determine the required consumption of heat carrier G_i through one TEG channel whereby hot heat carrier is cooled to given temperature. This allows defining the required number of thermopiles n_b, as well as the temperature condition of each module in thermopiles, its power N_m, as well as the power of thermopile NS and of generator on the whole N_T:

$$N_m = \frac{E^2}{4R};\ NS = \Sigma N_m;\ N_T = n_b NS, \tag{9}$$

where $E = n_v e(T_h - T_x)$ is module electromotive force; $R = n_v \frac{\rho h}{s}$ is its electric resistance.

Temperature distribution of heat carriers and thermoelement junctions along the thermopile composed of 10 modules is illustrated in Fig.4.

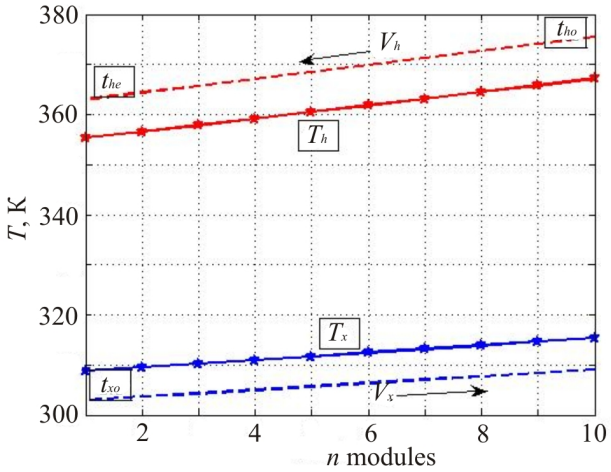

Fig. 4. Temperature distribution along the thermopile.

The next task is optimization of thermoelectric module parameters with a view to assure the best economic efficiency of TEG. Taking into account that thermopile dimensions are limited by housing dimensions of standard heat exchanger of internal combustion engine, thermoelement height h remains practically the only independent parameter which determines thermal resistance of thermopiles and, accordingly, all technical parameters of TEG, i.e. the necessary number of thermopiles and modules, heat exchange conditions in the channels, temperature difference on thermoelements, generator power and its cost.

Dependence of TEG power and efficiency is given in Fig. 5.

It is evident that increase in thermoelement height provides the opportunity of a more complete use of available temperature difference and the respective increase in thermoelement

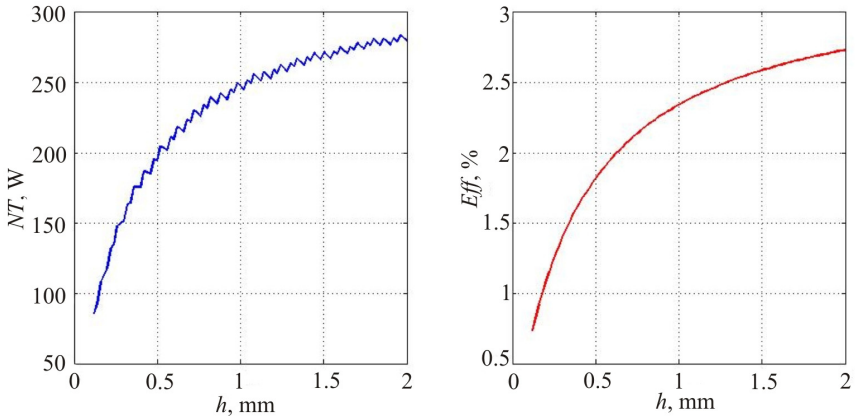

Fig. 5. Dependences of TEG power (NT) and efficiency (Eff) on thermoelement height h.

efficiency and total TEG power. However, increase in thermal resistance of thermoelements results in the reduction of heat transfer coefficient, which necessitates increase in heat exchange surface, i.e. increase in the number of thermopiles and TEG cost growth. Dependence of the necessary number of modules on thermoelement height is shown in Fig. 6 (fluctuations of curves are due to a discrete character of mathematical model – TEG dimensions can change only to integer values of the number of modules).

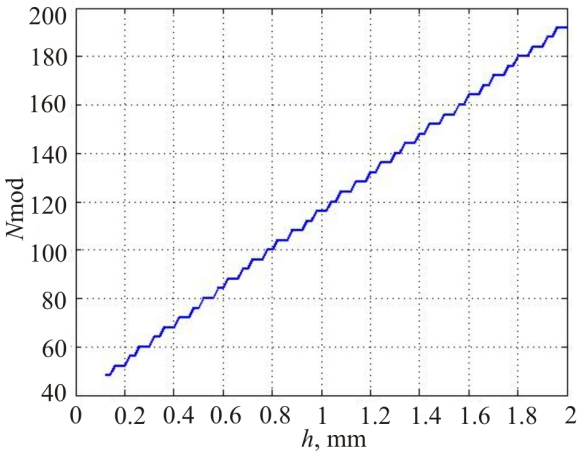

Fig. 6. Dependence of the necessary number of modules N_{mod} on thermoelement height h.

It should be noted that the cost of individual module is also a function of thermoelement height, as long as the necessary amount of thermoelectric material is changed. Dependence of specific cost of TEG power on thermoelement height with and without regard to this factor is given in Fig. 7 (as the base price, the retail cost of module 40x40 mm with thermoelement height 2 mm is taken, namely $P_{\$} = 5$ \$ US; the cost of thermoelectric material in module price is 20%).

From the above data it is seen that minimum specific cost of TEG is achieved in the range of relatively low powers, i.e. a desire to assure maximum TEG power leads to essential increase

of capital outlay. To overcome this contradiction, a compromise solution should be found that will guarantee the best technical and economic parameters of TEG. As the criteria for such solution,

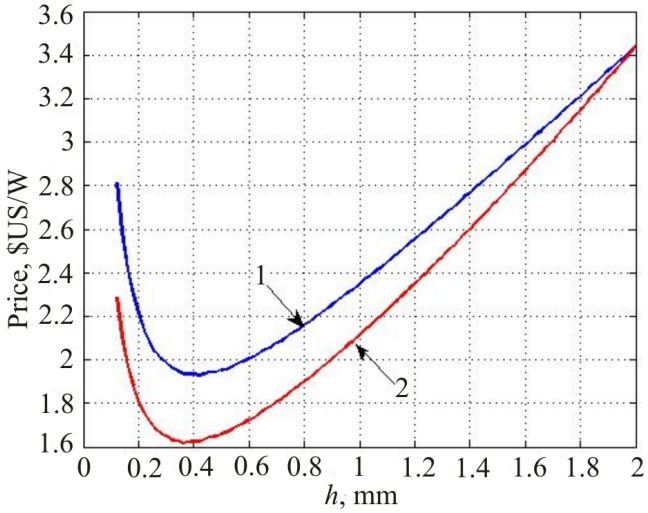

Fig. 7. Dependence of TEG specific cost, $US/W on thermoelement height h.
1 – without regard to h effect on material amount;
2 – with regard to h effect on material amount.

one can use the figures of fuel saving or TEG repayment period that can be calculated as:

$$T_{\text{O}} = \frac{\text{Price}}{\tau g P f}, \text{ years},$$

where Price is specific cost of TEG, $ US/kW; g is specific fuel cost for generation of 1 kW-h electric energy by marine plant (0.2 kg/kW-hour); P_f is fuel cost (approximately 1 $ US/kg); τ = 8640 hours/year.

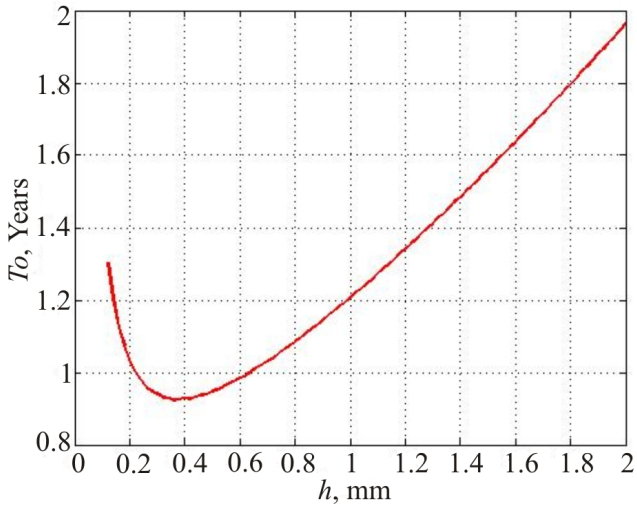

Fig. 8. Dependence of TEG repayment periods on thermoelement height h.

As follows from the foregoing, the scheme of TEG discussed above assures quite acceptable technical and economic features over a wide range of possible design concepts.

Conclusions

1. The scheme of heat exchange-type TEG using as the source of energy the heat of cooling system of marine propulsion plants is considered.
2. It is shown that the above scheme assures quite acceptable repayment periods which allow to expect wide application of similar TEG on water transport

Designations

L – thermopile length, cm;
b – thermopile width, cm;
F – thermopile area, cm^2;
h –thermoelement height, cm;
n_v – number of thermoelements in a module;
n_m – number of modules in a thermopile;
$P_\$$ – module cost, $ US;
$X = \frac{x}{L}$, $Y = \frac{y}{L}$, – dimensionless coordinates;
G – heat carrier losses, kg/s;
Cp – heat carrier specific heat, J/kgK;
$W = GCp/b\lambda$ – dimensionless water equivalent;
T – thermoelement temperature;
t – heat carrier temperature;
$\Theta = \frac{T}{T_p}$ – dimensionless thermoelement temperature;
$\vartheta = \frac{t}{T_p}$ – dimensionless heat carrier temperature;
T_p – characteristic temperature;
σ – electric conductivity coefficient $(Ohm\ cm)^{-1}$;
e – the Seebeck coefficient, V/K;
λ – thermal conductivity coefficient, W/cmK;
j – current density, A/cm^2;
$R_o = \frac{h}{\lambda}$ – thermal resistance of thermoelectric material, cm^2K/W;
α – heat-exchange coefficient, W/cm^2K;
K – heat-transfer coefficient, W/cm^2K;
$z = e^2\sigma/\lambda$ – thermoelectric figure of merit, K^{-1};
$Io = zT_p$ – Ioffe criterion;
$Bi = \frac{h}{\lambda Rt}$ – Biot criterion;
Ki – Kirpichev criterion;
Nu – Nusselt criterion;
Re – Reynolds criterion;
Pr – Prandtl criterion;

$J = \frac{jeh}{\lambda}$ – dimensionless current density;

Indices: h – hot; x – cold.

References

1. Yu. M. Lobunets, Heat-Exchange Type TEG for Marine Propulsion Plants, Part I, J.Thermoelectricity // – 2014. –№ 5. – P.29-36.
2. http://www.alfalaval.com/industries/marine/cooling-heating/pages/cooling-and-heating.aspx.
3. Yu. M. Lobunets, Thermoelectric Generator, Patent of Ukraine №8357 of 27.08.2013.
4. Yu. M. Lobunets, Performance Analysis of Heat-Exchange Type Thermoelectric Generator, J.Thermoelectricity // – 2014. – № 1. – P.52-58.

Submitted 15.12.2015

L. I. Anatychuk, R. V. Kuz, A. V. Prybyla

Institute of Thermoelectricity NAS and MES of Ukraine
1, Nauky Str., Chernivtsi, 58029, Ukraine

EFFICIENCY IMPROVEMENT OF SECTIONAL THERMOELECTRIC HEAT RECUPERATORS

The paper deals with a physical model of a thermoelectric sectional heat recuperator. Its mathematical description is given and a computer model is developed. The simulation of the recuperator is done for the hot gas temperature range from 150 to 600°C. Dependences of optimal temperatures of recuperator sections on the inlet gas temperature are established. The number of thermoelectric converters in each section for optimal temperature distribution in the sections is determined. The specific cost of each section of thermoelectric heat recuperator in the above temperature range is calculated.

Key words: heat recuperator, thermoelectric generator, computer simulation.

Introduction

General characterization of the problem. Annual energy consumption in the world is on the order of 13 TW. According to predictions, by the end of the century these figures will be tripled by population growth and industrial development [1-3]. At the same time, the majority of industrial process equipment, thermal machines (turbines, internal combustion engines, etc.), while in operation, dissipate huge amount of thermal waste [4]. This heat is not used at all, and, moreover, leads to adverse implications for the environment, namely its thermal pollution. This situation is due to the fact that thermal waste temperatures are in the range of 50-700 ºC, and the use of heat engines for this temperature range, especially below 400 ºC, in most cases is unreasonable. Such thermal waste recovery is a relevant task of thermoelectricity.

Analysis of the literature. Analysis shows [5] that 90% of waste thermal energy is released by industrial facilities at surface temperatures up to 300 ºC (Fig. 1). Exactly thermoelectric method of

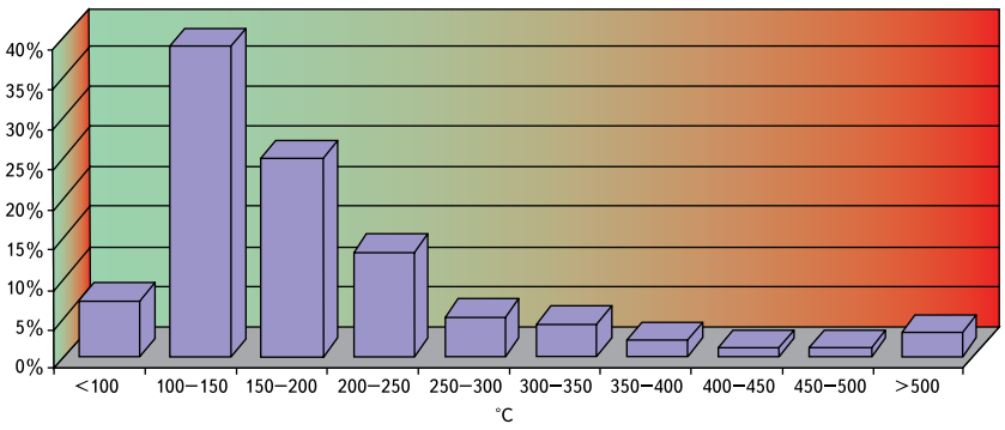

Fig. 1. Temperature distribution on the surfaces of commercial units [4].

direct thermal into electric energy conversion is beneficial for heat recovery at such temperatures [6- 9].

All kinds of practical applications of thermoelectric recuperators of waste thermal energy from internal combustion engines, gas turbines and various industrial furnaces are described in [10-17]. These works are concerned with one-section recuperators, which is not always efficient. The results of optimization of a thermoelectric sectional recuperator using exhaust heat from automobile engine are presented in [19-20]. Calculations have established possible efficiency improvement of thermal energy recovery up to 40% with the use of optimal number of generator sections. However, calculations in these works were performed for the temperature range of 400-800 ºC, which, as was shown earlier, does not correspond to the most common temperatures of heat recovery.

The purpose of this work is efficiency increase of thermoelectric heat recuperator via optimization of the number of sections in the temperature range from 150 to 600 ºC.

Physical model of a thermoelectric sectional heat recuperator

A physical model of a thermoelectric sectional heat recuperator is represented in Fig. 2.

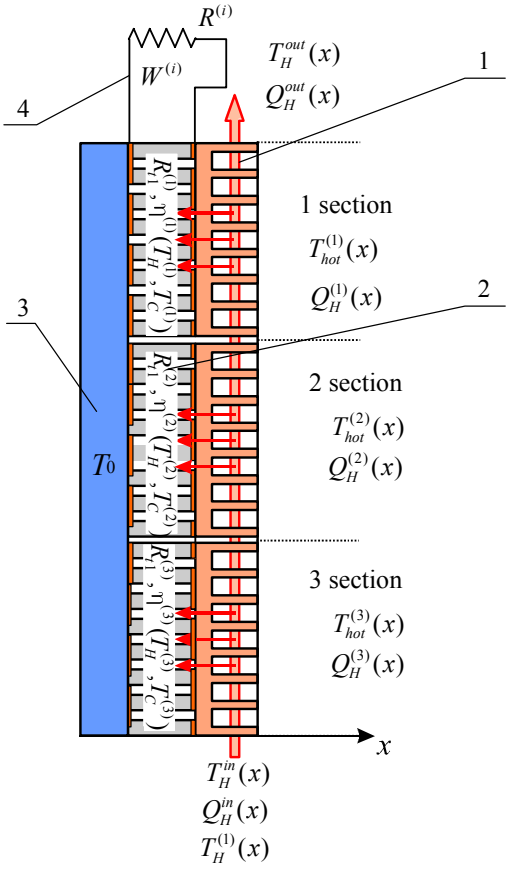

Fig. 2. Physical model of a thermoelectric sectional heat recuperator:
1 – hot heat exchanger; 2 – thermopiles; 3 – cold heat exchanger;
4 – matched electric load of section.

Each recuperator section consists of hot heat exchanger (1), thermopile (2) with thermal resistance $R_{t2}^{(i)}$ and efficiency $\eta(T_H, T_0)$; cold heat exchanger (3) with temperature T_0. Matched electric load $R^{(i)}$ is connected to thermopiles of each recuperator section (4). The inlet hot gas flow has temperature T_H^{in} and thermal power Q_H^{in}. The hot gas gives up part of heat $Q_H^{(i)}(x)$ at temperature $T_{hot}^{(i)}(x)$ to the hot heat exchanger. Gas flow at recuperator inlet has temperature T_H^{out} and thermal power Q_H^{out}. Heat from the hot heat exchanger is passed to thermopile, heating its hot side to temperature $T_H^{(i)}(x)$. Two variants of heat exchange with the cold side of thermopiles are considered. In one case, the cold side temperature T_0 is constant, and in the other heat exchange of cold heat sink *3* with the ambient is taken into account. To calculate maximum possible recuperator power, heat losses will be ignored.

Mathematical and computer description of the model

To optimize the thermoelectric sectional heat recuperator, one should find the distribution of temperatures and heat flows in the thermopiles of each section. Such calculations for the represented model are possible only with the use of computer simulation.

Let us consider one of generator sections and conventionally divide it into three areas $\Omega_1 - \Omega_3$ with the limits $g_1 - g_{10}$ (Fig. 3). Area Ω_1 is the hot heat exchanger with heat carrier, area Ω_2 is the thermopile, and area Ω_3 is the hot and cold heat exchangers.

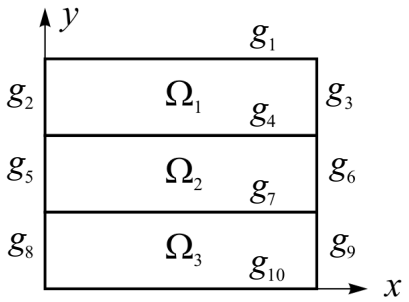

Fig. 3. Computer representation of the areas and boundaries of recuperator sections.

In area Ω_1 there is mass transfer of the hot heat carrier. The thermal conductivity equation for this area is of the form:

$$-\nabla\left(\kappa_H(T)\nabla T\right) = -\rho_H(T)C_H(T)\vec{v}\nabla T\,, \tag{1}$$

where ρ_H is density, C_H is heat capacity, κ_H is gas thermal conductivity, v_H is gas motion velocity. The boundary conditions for area Ω_1 take into account the continuity of gas flow with and between the sections, heat flow through heat exchangers.

The Joule heat is released in area Ω_2 (thermopile). For area Ω_2 the thermal conductivity equation is given below:

$$-\nabla\left(\kappa_{TE}(T)\nabla T\right)=Q_J\,, \tag{2}$$

where κ_{TE} is effective thermal conductivity of thermopile, Q_J is specific power of the Joule heat released in the thermopile.

The boundary conditions for area Ω_2 take into account the interaction between thermopile and heat exchangers.

Area Ω_3 in this model of TEG is considered to be thermostated with temperature T_0.

A combination of the boundary conditions is mathematically expressed as follows:

g_1: $$q_1^{(i)}(x)=0\,, \tag{3}$$

g_2, g_3: $$Q_H^{in(1)}=Q_H^{in},\ Q_H^{in(i+1)}=Q_H^{out(i)},\ Q_H^{out(N)}=Q_H^{out}\,, \tag{4}$$

g_4: $$Q_H^{(i)}(x)=\left(T_H^{(i)}(x)-T^{(i)}(x)\right)/R_{t1}^{(i)} \tag{5}$$

g_5, g_6: $$q_4^{(i)}(y)=0\,, \tag{6}$$

g_7: $$Q_C^{(i)}(x)=\left(T_C^{(i)}(x)-T^{(i)}(x)\right)/R_{t2}\,,$$

$$T(x)=T_0\,, \tag{7}$$

Ω_3, g_8, g_9, g_{10}: $$T(x,y)=T_0\,. \tag{8}$$

A combination of equations (1)-(2) with the boundary conditions (3-8) permits to find temperature field $T(x,y)$ in TEG and to determine the distribution of temperatures $T_H^{(i)}(x)$ along the hot sides of section thermopiles.

Then the power of each section can be found from the following expression:

$$W^{(i)}=\int Q_H^{(i)}(x)\eta(T_H^{(i)}(x),T_C^{(i)}(x))dx\,. \tag{9}$$

Total generator power

$$W_{TEG}=W^{(1)}+W^{(2)}+W^{(3)}\,. \tag{10}$$

Thermoelectric generator efficiency

$$\eta_{TEG}=\frac{W_{TEG}}{Q_H^{in}}\,. \tag{11}$$

To calculate the recuperator electric power with regard to provision of heat removal system, it is necessary to know the efficiency of air-liquid heat exchanger

$$Q_{cool}=f(W_{cool},T_L,T_A)\,, \tag{12}$$

where Q_{cool} is thermal power of heat removal system, W_{cool} is electric supply power of heat removal system, T_L is liquid temperature, T_A is air temperature. Such dependence was obtained

from the experimental studies of heat exchanger [18].

The effective efficiency of the recuperator is introduced by the expression:

$$\eta_{ef} = (W_{TEG} - W_{cool}) / Q_{in} . \quad (13)$$

A system of equations (1)-(2) with the boundary conditions (3)-(8) was solved by finite element method [21] on a two-dimensional mesh**.**

Further optimization consists in a search for optimal hot temperatures of sections through variation of thermal resistances of sections in order to achieve maximum integral efficiency of thermoelectric recuperator.

Computer simulation results

For the calculation of the efficiency and power there were selected *Bi-Te* based thermoelectric materials whose figures of merit are among the best in the temperature range under consideration [21].

Computer simulation of thermoelectric sectional recuperator of thermal energy yielded the following results.

During the first step, optimization of the hot temperatures of recuperator sections was performed. The presence of such optimum is due to the impact of two competing factors. The reduction of section thermal resistance leads to increase in thermal flow through thermoelectric converter, hence to increase in the section electric power. On the other hand, this leads to thermopile hot temperature decrease, and, accordingly, its efficiency decrease. Fig. 4 presents the results of optimization of the hot temperature of sections versus the inlet gas temperature. Fig. 5 shows a relative number of one-type thermoelectric modules in a section for the achievement of optimal temperature distribution.

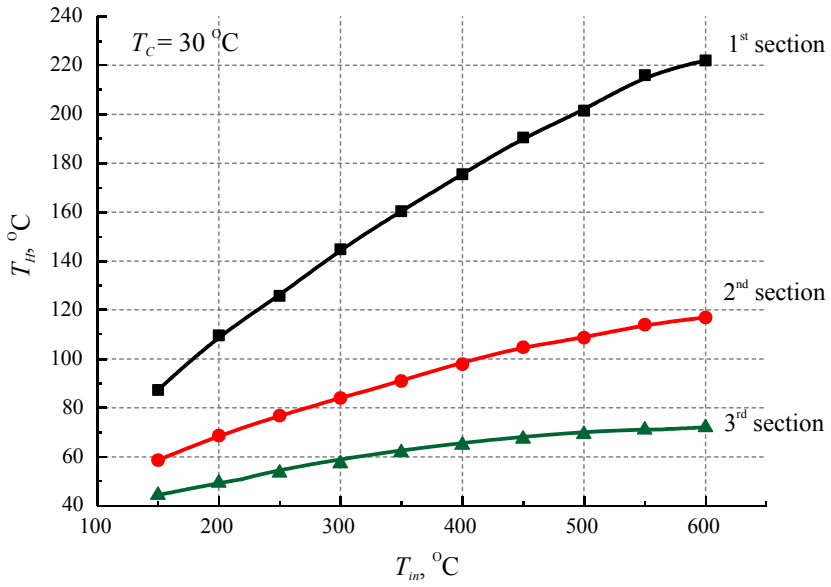

Fig. 4. Optimal hot temperature of sections versus the inlet gas temperature.

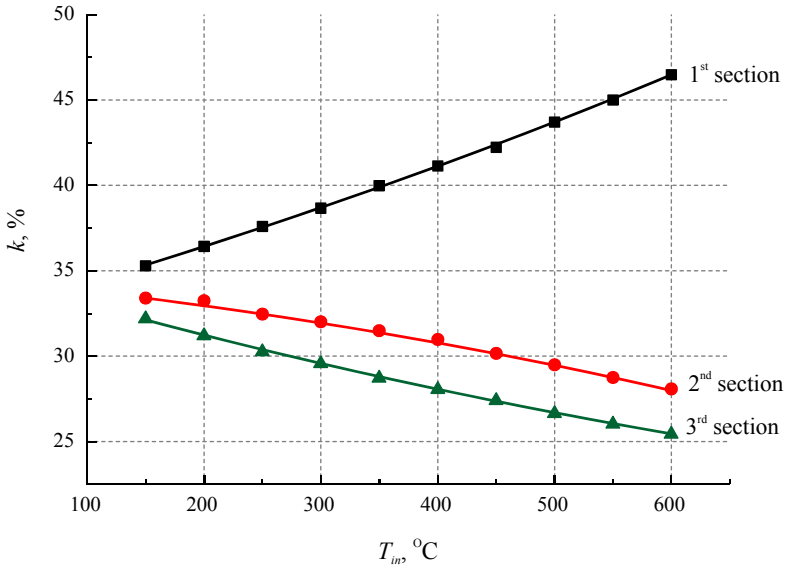

Fig. 5. Relative number of thermoelectric modules in a section for achievement of optimal temperature distribution.

The next simulation step was to determine the efficiency of thermoelectric modules (Fig. 6) and heat recuperator as a whole (Fig. 7) versus the inlet gas temperatures.

Fig. 6 shows the efficiency of thermoelectric modules from each recuperator section versus the inlet gas temperatures.

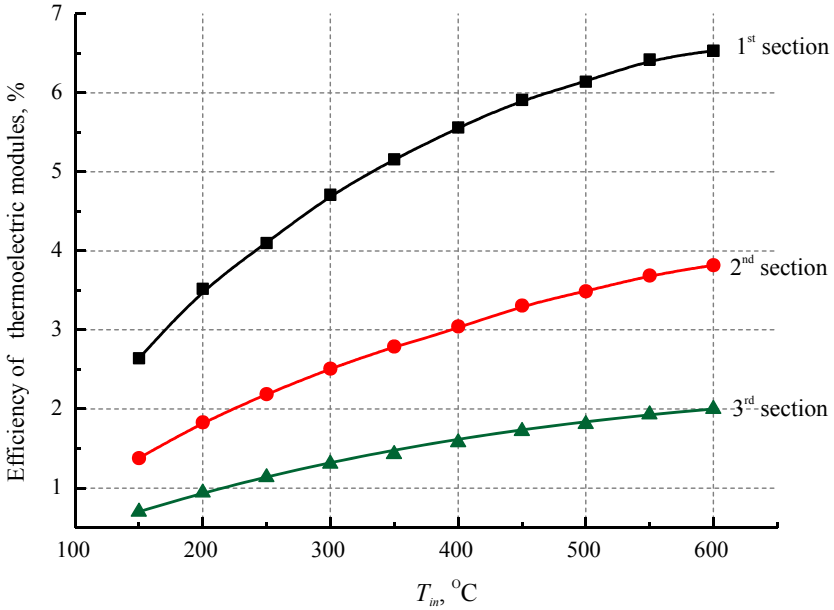

Fig. 6. The efficiency of thermoelectric modules of sections versus the inlet gas temperatures.

As is seen from Fig. 7, using the second section in thermoelectric heat recuperator results in efficiency increase by ~ 16%, and the third section – by as low as 4%.

Contribution by percentage of each section of thermoelectric heat recuperator to its total power is given in Fig. 8. As it follows from the figure, contribution by percentage of the first recuperator section to total power is 75-85%, the second section – 15-20%, the third – about 5%.

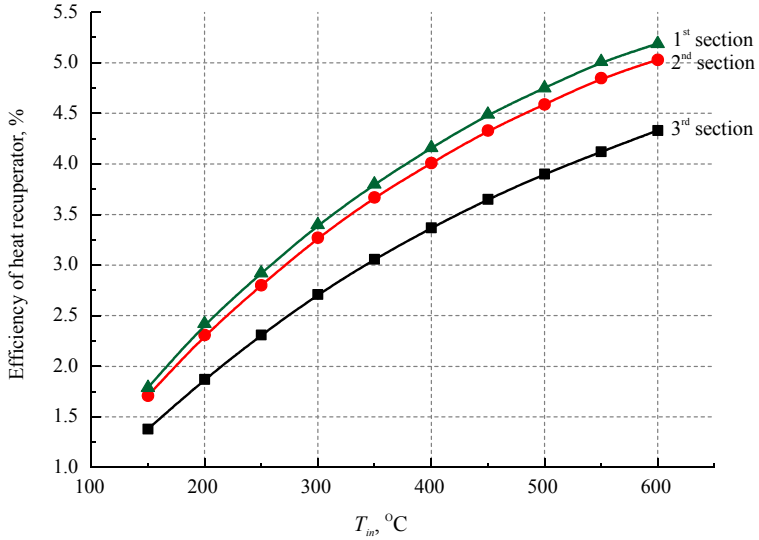

Fig. 7. The efficiency of thermoelectric sectional recuperator versus the inlet gas temperatures.

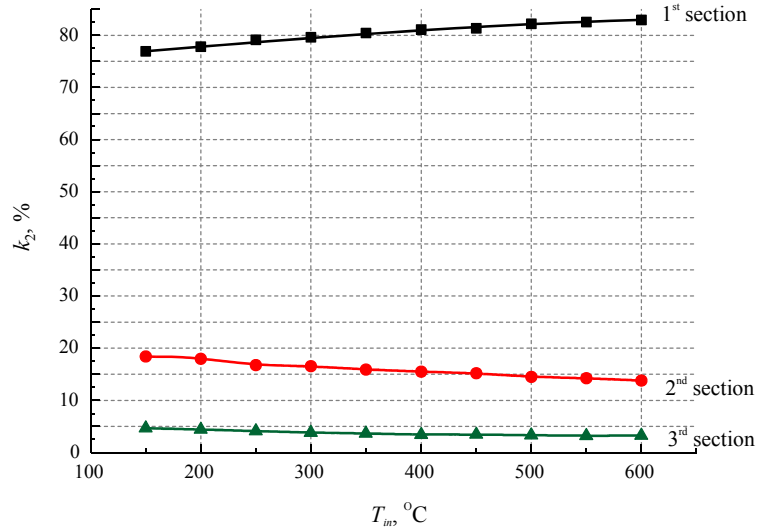

Fig. 8. Contribution by percentage of each recuperator section to its total power.

To estimate the economic viability of using sections in thermoelectric heat recuperator, the specific cost of the sections was calculated (Fig. 9) based on the results obtained in [22]. As is seen from the figure, using the third section in the temperature range under consideration is economically unviable. Using the second section is worthwhile at the hot gas temperatures from 400 ºC.

To estimate the economic viability of using sections in thermoelectric heat recuperator, the specific cost of the sections was calculated (Fig.9) based on the results obtained in [22]. As is seen from the figure, using the third section in the temperature range under consideration is economically unviable. Using the second section is worthwhile at the hot gas temperatures from 400 ºC.

Moreover, estimation was made of the energy and economic features of thermoelectric heat recuperator with regard to energy expenditures on heat removal. Fig. 10 shows the efficiency of thermoelectric sectional recuperator versus the inlet gas temperature with regard to expenditures on heat removal.

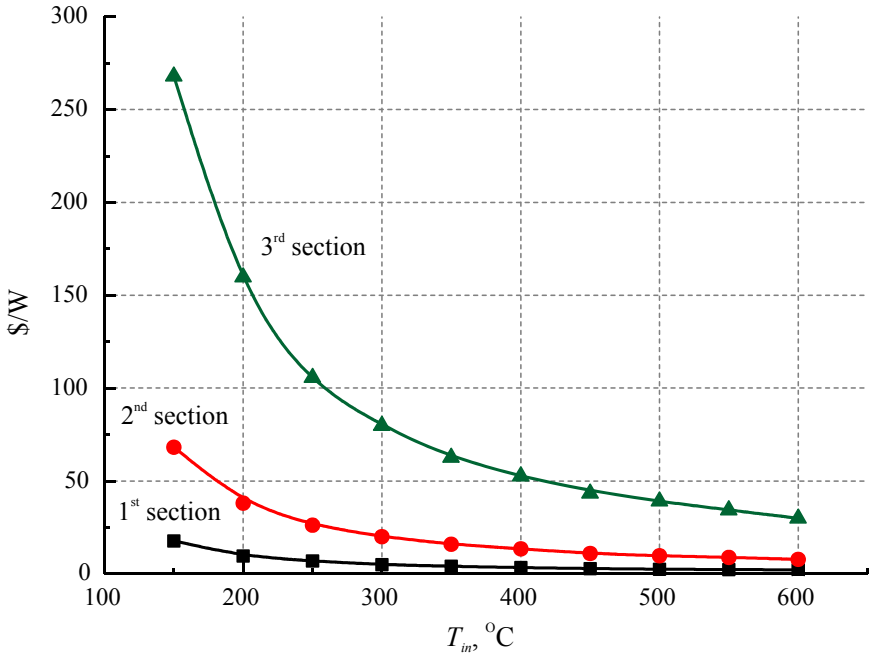

Fig. 9. Specific cost of recuperator sections.

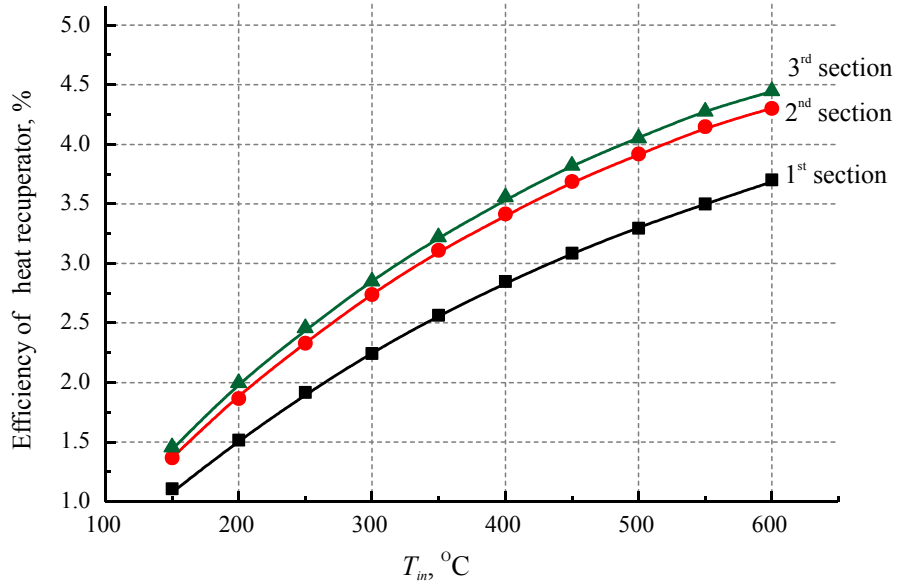

Fig. 10. The efficiency of a thermoelectric sectional recuperator versus the inlet temperature with regard to heat removal expenditures.

Fig. 11 shows the specific cost of recuperator sections with regard to heat removal expenditures. As is seen from the figures, the efficiency of heat recuperation in this case is reduced by ~ 15-20%, and the specific cost is accordingly increased by the same value.

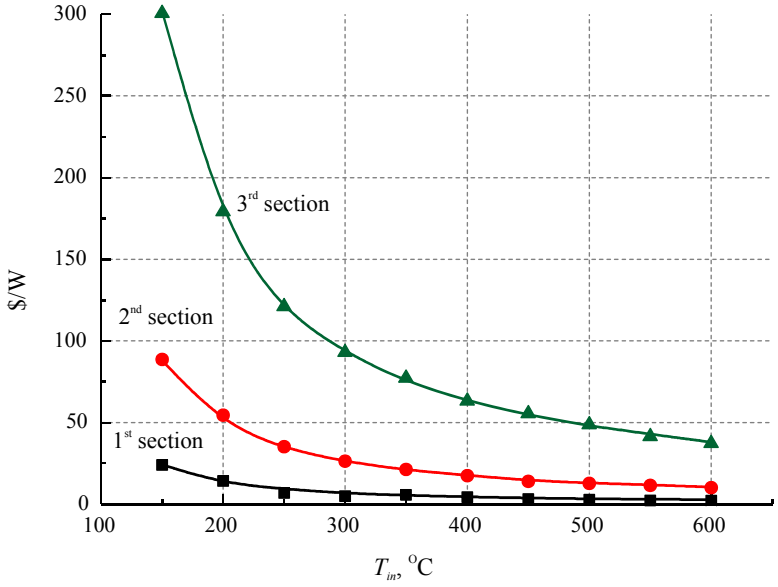

Fig. 11. Specific cost of recuperator sections with regard to heat removal expenditures.

Conclusions

1. Dependences of the optimal temperatures of recuperator sections on the inlet gas temperature in the range from 150 to 600 ºC are established. For the first section they make from 90 to 220 ºC, for the second – from 60 to 120 ºC, for the third– from 40 to 70 ºC.
2. The number of thermoelectric converters for each section necessary to achieve optimal temperature distribution in the sections is determined. For low inlet gas temperatures (150 ºC) the number of thermal converters in the sections is about the same. With a rise in temperatures, the share of thermal converters in the first section is increased.
3. Using the second section of thermoelectric heat recuperator in the range of inlet gas temperatures from 150 to 600 ºC leads to its efficiency increase by ~ 16%, and the third – by as low as 4%.
4. The specific cost of each section of thermoelectric heat recuperator in the above temperature range is calculated. It is established that the specific cost of the third section is an order higher than the cost of the first section, which makes its application inadvisable. Using the second section is worthwhile at the hot gas temperatures from 400 ºC
5. The efficiency of heat recuperation with regard to energy expenditures on heat removal is reduced by ~ 15-20%, and the specific cost is accordingly increased by the same value.

References

1. Basic Research Needs for Solar Energy Utilization, Report of the Basic Energy Sciences Workshop on Solar Energy Utilization, USA: DOE, April 18−21, 2005.
2. M. D. Rowe, Gao Min, S. G. K. Williams, A. Aoune, K. Matsuura, V. L. Kuznetsov, and Li Wen Fu, Thermoelectric Recovery of Waste Heat-Case Studies, Energy Conversion Engineering Conference, 1997, vol.2, p. 1075 – 1079.
3. D. M. Freik, L. I. Nikiruy, and O. S. Krinitskiy, Advances and Problems of Thermoelectricity, Physics and Chemistry of the Solid State **13**(2), 297-318 (2012).
4. V. Panyakiv, Cogeneration: The Way it Works, Networks and Business **4** (2010).
5. P. Shostakovsky, Thermoelectric Alternative Power Supply Sources, New Technologies **12**, 131-138 (2010).
6. L. I. Anatychuk, Rational Areas of Thermoelectric Research and Applications, J.Thermoelectricity **1**, 3 – 14(2001).
7. L. I. Anatychuk, Current Status and Some Prospects of Thermoelectricity, J.Thermoelectricity **2**, 7 – 20 (2007).
8. A. S. Bernshtein, Thermoelectric Generators (Moscow: Gosenergoizdat, 1956), 47 p.
9. L. I. Anatychuk, Thermoelements and Thermoelectric Devices: Handbook (Kyiv: Naukova Dumka, 1979), 768 p.
10. S. Sano, H. Mizukami, and H. Kaibe, Development of High-Efficiency Thermoelectric Power Generation System, KOMATSU Technical Report **49**(152), 1–7 (2003).
11. L. I. Anatychuk, A. V. Prybyla, Thermoelectric Heat Recuperator for Gas Turbines, Proc. of XIII Interstate Workshop “Thermoelectrics and Their Applications”, November 13-14, 2012, Saint-Petersburg, Russia.
12. L. I. Anatychuk, J. D. Hwang, H. S. Chu, H. L. Hsieh, The Design and Application of Thermoelectric Generators on the Waste Heat Recovery of Heating Furnace in Steel Industry, XIV International Forum on Thermoelectricity (May 17-20, 2011, Russian Federation, Moscow).
13. H. Kaibe, T. Kaijihara, S. Fujimoto, K. Makino, and H. Hachiuma, Recovery of Plant Waste Heat by a Thermoelectric Generating System, KOMATSU Technical Report **57**(164), 26–30 (2011).
14. T. Kajikawa, Advances In Thermoelectric Power Generation Technology In Japan, J.Thermoelectricity **3**, 5–19(2011).
15. H. Kaibe, K. Makino, T. Kajihara, S. Fujimoto, and H. Hachiuma, Thermoelectric Generating System Attached to a Carburizing Furnace at Komatsu Ltd., Awazu Plant, AIP Conf. Proc. 1449, 524 (2012)
16. L. I. Anatychuk, Jenn-Dong Hwang, V. V. Lysko, and A.V.Prybyla, Thermoelectric Heat Recuperators for Cement Kilns, J.Thermoelectricity **5**, 39-45 (2013).
17. T. Kuroki, K. Kabeya, K. Makino, T. Kajihara, H. Kaibe, H. Hachiuma, and H. Matsuno, Thermoelectric Generation Using Heat in Steal Works, J. Electronic Materials (2014).
18. L. I. Anatychuk, R. V. Kuz, Effect of Air Cooling on the Efficiency of Thermoelectric Generator in a Diesel-Engined Car, J.Thermoelectricity **2**, 61-69 (2014).
19. L. I. Anatychuk, R. V. Kuz, Effect of Air Cooling on the Efficiency of Sectional Thermoelectric Generator in a Car with a Diesel Engine, J.Thermoelectricity **4**, 84-92 (2014).

20. L. I. Anatychuk, R. V. Kuz, Effect of Air Cooling on the Efficiency of Sectional Thermoelectric Generator in a Car with a Petrol Engine, J.Thermoelectricity **3**, 87-92 (2014).
21. L. I. Anatychuk, R. V. Kuz', Materials for Vehicular Thermoelectric Generators, Proc. of ICT-2011, Michigan, USA.
22. L. I. Anatychuk, R. V. Kuz, and J. D. Hwang, The Energy and Economic Parameters of *Bi-Te* Based Thermoelectric Generator Modules for Waste Heat Recovery, J. Thermoelectricity 4, 73 – 79 (2012).

Submitted 11.12.2014

NEWS
OF INTERNATIONAL THERMOELECTRIC ACADEMY

XVI INTERNATIONAL FORUM ON THERMOELECTRICITY

Paris, May 19 – 22, 2015

The Forum is dedicated to Jean Charles Athanase Peltier, a French researcher and pioneer in thermoelectric cooling.

The International Thermoelectric Academy acts as an organizer of the Forum.

The objective of the Forum is the discussion of the recent progress in thermoelectricity, prospects of its development and creation of the constructive atmosphere for generation of new ideas. Invited reports on the analysis of the state-of-art in thermoelectricity will be delivered. Oral presentations and poster sessions are accepted. After reviewing the reports will be published in "The Journal of Thermoelectricity". The Editorial Board of the Journal consists of the members of the International Thermoelectric Academy. The Journal is included into Scopus database. The electronic version of the Journal is available at http://jt.inst.cv.ua.

The outstanding event at the Forum will be the unveiling of the monument to Jean Charles Athanase Peltier in Ham, his native town, situated 130 km from Paris. The International Thermoelectric Academy acts as a founder of the monument. The appearance of the monument is shown in the picture; its height being 2.4 m. Festivities on the unveiling of the monument will take place on May 22, 2015.

Welcome for participation in the work of the Forum and festivities dedicated to the unveiling of the monument to Peltier!

Please visit the site of the Forum forum2015.inst.cv.ua for details (starting with Jan. 01, 2015).

ARTICLE PREPARATION RULES

The article shall conform to the journal profile. The article content shall be legible, concise and have no repetitions.

The article shall be submitted to the editorial board in electronic version.

The text shall be typed in text editor not lower than MS Word 6.0/7.0.

Page setup: "mirror margins"- top margin – 2.5 cm, bottom margin – 2.0 cm, inside – 2.0 cm, outside– 3.0 cm, from the edge to page header – 1.27 cm, page footer – 1.27 cm.

Graphic materials, pictures shall be submitted in color or, as an exception, black and white, in .opj or .cdr formats, .jpg or .tif formats being also permissible. According to author's choice, the tables and partially the text can be also in color.

The article shall be submitted in English on A4 paper sheets; the number of pages shall not exceed 12. By agreement with the editorial board, the number of pages can be increased.

To accelerate publication of the article, please adhere to the following rules:

- the authors' initials and names are arranged in the centre of the first page at the distance of 1 cm from the page header, font Times New Roman, size 12 pt, line spacing 1.2;
- the name of organization, address (street, city, postal code, country) – indent 1 cm below the authors' initials and names, font Times New Roman, size 11 pt, line spacing 1.2, center alignment;
- the title of the article is arranged 1 cm below the name of organization, in capital letters, semi-bold, font New Roman, size 12 pt, line spacing 1.2, center alignment. The title of the article shall be concrete and possibly concise;
- the abstract is arranged 1 cm below the title of the article, font Times New Roman, size 10 pt, in italics, line spacing 1.2 ,center alignment;
- key words are arranged below the abstract, font Times New Roman, size 10 pt, line spacing 1.2, justified alignment. The title "Key words" – font Times New Roman, size 10 pt, semi-bold;
- the main text of the article is arranged 1 cm below the abstract, indent 1 cm, font Times New Roman. size 11 pt, line spacing 1.2, justified alignment;
- formulae are typed in formula editor, fonts Symbol, Times New Roman. Font size is "normal" – 12 pt, "large index" – 7 pt, "small index" – 5 pt, "large symbol" – 18 pt, "small symbol" – 12 pt). The formula is arranged in the text, centre aligned and shall not occupy more

than 5/6 of the line width, formulae are numbered in round brackets right;

• dimensions of all quantities used in the article are represented in the International System of Units (SI) with the explication of the symbols employed;

• figures are arranged in the text. The figures and pictures shall be clear and contrast; the plot axes – parallel to sheet edges, thus eliminating possible displacement of angles in scaling;

• tables are arranged in the text. The width of the table shall be 1 cm less than the line width. Above the table its ordinary number is indicated, right alignment. Continuous table numbering throughout the text. The title of the table is arranged below its number, center alignment;

• references should appear at the end of the manuscript. References within the text should be enclosed in square brackets. References should be numbered in order of first appearance in the text. Examples of various reference types are given below.

– L.I. Anatychuk, *Thermoelements and Thermoelectric Devices: Handbook* (Kyiv: Naukova Dumka, 1979), p.766. (Book)
– T.M. Tritt, Thermoelectric Phenomena, Materials, and Applications, *Annual Review of Materials Research* **41**, 433 (2011). (Journal paper)
– U. Ghoshal, *Proceedings of the XXI International Conference on Thermoelectrics* (N.Y., USA, 2002), p. 540. (Proceedings Conference)

The article should be supplemented by:

• letter from the organization where the work was performed or from the authors of the work applying for the publication of the article;

• information on the author (authors): last name and initials; full name and postal address of the institution where the author works; academic degree; position; telephone number; E-mail;

• author's (authors') photo in color or, as an exception, in black and white. With the number of authors more than two their photos are not given;

• author's application to the following effect:

We, the undersigned authors, … transfer to the founders and editors of "Journal of Thermoelectricity" the right to publish the article…in Ukrainian, Russian and English. This is to confirm that the present publication does not violate the copyright of other persons or organizations.

Date Signatures

Below is given an example of article preparation.

Author's photo 3 × 4 cm

A.I. Casian[1], B.M. Gorelov[2]

[1]Technical University of Moldova,
168, Stefan cel Mare Ave.,
Chisinau, MD-2004, Moldova;
[2]Institute of Surface Chemistry of National Academy
of Sciences of Ukraine, 17, Gen. Naumov Str.,
Kyiv, 03164, Ukraine

Author's photo 3 × 4 cm

STATE OF THE ART AND PROSPECTS OF THERMOELECTRICITY ON ORGANIC MATERIALS

The aim of the paper is to analyze the expected thermoelectric opportunities of organic materials, including some highly conducting quasi-one-dimensional crystals. It is shown that interest of investigators in these materials has been growing recently. Quasi-one-dimensional organic crystals have high prospects for thermoelectric applications. These materials combine the properties of multi-component systems with more diverse internal interactions and of quasi-one-dimensional quantum wires with increased density of electronic states. It is shown that the values of the thermoelectric figure of merit ZT ~ 1.3 – 1.6 at room temperature are expected in really existing organic crystals of tetrathiotetracene-iodide, TTT_2I_3, if the crystal parameters are approaching the optimal ones.

Key words: thermoelectricity, tetrathiotetracene-iodide, polarizability.

Introduction

It is known that conducting organic materials usually have much lower thermal conductivity than the inorganic materials. Moreover, the organic materials can be fabricated by simpler chemical methods, and it is expected that such materials will be less expensive in comparison with the inorganic ones. Exactly these properties attracted attention to such materials for the use in thermoelectric (TE) applications long time ago [1, 2]. In spite of relatively high value of the thermoelectric figure of merit $ZT = 0.15$ at room temperature observed in polycopper phthalocyanine [2] as early as 1980, the thermoelectric properties of organic materials are still weakly investigated. This situation has the only explanation that thermoelectricians are still weakly interested in organic materials, and organic chemists are also weakly interested in thermoelectric materials. Moreover, in order to seek good organic thermoelectrics, it is necessary to organize multidisciplinary consortiums of physicists, organic chemists and engineers in the field of thermoelectricity. …

The aim of this paper is to present briefly the state-of-the-art of investigations in the area of new organic thermoelectric materials and to describe the nearest expected results for really existing quasi-one-dimensional organic crystals of tetrathiotetracene-iodide, TTT_2I_3.

Quasi-one-dimensional organic crystals of TTT_2I_3

The structure of quasi-one-dimensional organic crystals of tetrathiotetracene-iodide, TTT_2I_3, has been briefly described in [34]. These needle-like crystals are formed of segregate chains or stacks of planar molecules of tetrathiotetracene *TTT*, and iodine ions. The chemical compound TTT_2I_3 is of mixed-valence: two molecules of *TTT* give one electron to the iodine chain which is formed from I_3^- ions. The conductivity of iodine chains is negligibly small, so that only *TTT* chains are electrically conductive and holes serve as carriers. The electrical conductivity σ along *TTT* chains at room temperature varies between 10^3 and $10^4\ \Omega^{-1}\text{cm}^{-1}$ for crystals grown by gas phase method [35], and between 800 and $1800\ \Omega^{-1}\text{cm}^{-1}$ for crystals grown from solution [36]. Thus, the conductivity is very sensitive to crystal impurity and perfection which depends on growth method. In the direction perpendicular to chains σ is by three orders of magnitude smaller than in the longitudinal direction and is neglected. …

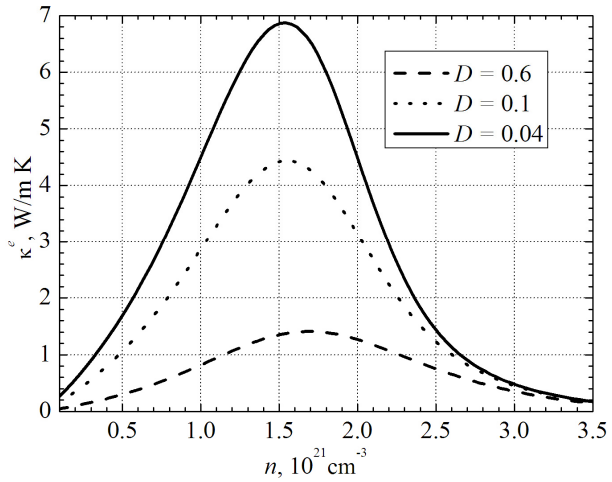

Fig. 1. Dependences of electron thermal conductivity κ^e *on n.*

$$\sigma = R_0,\ S = R_1 / eTR_0,\ \kappa^e = \left(e^2T\right)^{-1}\left(R_2 - R_1^2 / R_0\right), \tag{1}$$

Thermoelectric properties

Expressions (2) – (3) have been calculated in order to determine the thermoelectric properties of quasi-one-dimensional organic crystals of TTT_2I_3 with different degrees of purity….

Conclusions

The state-of-the-art of research on new organic materials for thermoelectric applications is analyzed. It is shown that the interest of investigators in these materials has been growing in recent years. The highest value of $ZT \sim 0.38$ at room temperature has been measured in doped acetylene, with the only problem that this material is not stable. Accurate control of the oxidation level in poly (3, 4-ethylenedioxythiophene) (PEDOT) gave the power factor $324\ \mu\text{W}\cdot\text{m}^{-1}\text{K}^{-2}$ and in

combination with its low intrinsic thermal conductivity ($\kappa = 0.37$ W·m^{-1}K^{-1}) yielded $ZT = 0.25$ at room temperature, and this material is air-stable….

References

1. Ali Shakouri, Recent Developments in Semiconductor Thermoelectric Physics and Materials, *Annu.Rev.Mater.Res*.**41**, 399-431 (2011).
2. L.I. Anatychuk, *Thermoelectricity, Vol.2, Thermoelectric Power Converters* (Kyiv, Chernivtsi: Institute of Thermoelectricity, 2003), 376p.
3. M.E. Bengen, *German Patent Appl*. OZ 123, 438, 1940; *German Patent* 869,070, 1953, Tech. Oil Mission Reel, 143,135, 1946.